Building Quantum Networks Using Diamond Nanophotonics

Citation

Nguyen, Christian Thieu. 2020. Building Quantum Networks Using Diamond Nanophotonics. Doctoral dissertation, Harvard University, Graduate School of Arts & Sciences.

Dissertation advisor: Professor Mikhail D. Lukin Christian Thieu Nguyen

Building quantum networks using diamond nanophotonics

Abstract

The construction of a quantum internet, an interconnected network which can distribute and store quantum states, is an essential step towards the development of next generation quantum technologies, including unconditionally secure communication, enhanced metrology, and distributed quantum computing. Development of these networks require functional nodes consisting of stationary registers with the capability of high-fidelity quantum information processing and storage, which efficiently interface with photonic qubits. This thesis outlines one emerging platform for building a quantum network node using the silicon-vacancy color center in diamond (SiV). Although previous work has established the SiV as a superior optical emitter capable of strong light-matter coupling, its feasibility as a quantum memory has remained elusive, primarily due to coupling to thermal phonons. This suggests two branching research directions: one where this coupling is investigated and characterized as a nanoscale sensor, and one where this coupling is supressed in order to realize the SiV as a quantum information processor. This thesis begins by highlighting the extreme phonon sensitivity as a metrological tool, where an ensemble of SiVs are used as an all-optical thermometer, capable of 70 mK precision at room temperature. When incorporated into nanodiamonds, the sensing properties deviate by less than 1% between nanodiamonds, enabling calibration-free thermometry for sensing and control of complex nanoscale systems. For quantum information tasks, coherent control of the SiV electronic spin qubit is enabled by suppressing phonon-induced dephasing by five orders of magnitude at temperatures below 500 mK. By aligning the magnetic field along the silicon-vacancy symmetry axis, optical transitions are highly spin-conserving, allowing for single-shot readout of the qubit with high fidelity. This coherent control is used to demonstrate a spin coherence time $T_2 > 13\,\mathrm{ms}$ and spin relaxation time $T_1 > 1\,\mathrm{s}$ at 100 mK. Finally, SiV quantum memories are packaged into a fully integrated quantum network node by incorporating SiV qubits into nanophotonic cavities. The efficient SiV-cavity coupling (with cooperativity $C > 30$) provides a nearly-deterministic interface between photons and the spin qubit, which enables heralded single-photon storage. Coherent coupling to nearby ^{13}C nuclear spins (with nearly second-long coherence times) enables multi-qubit registers and paves the way towards large-scale quantum networks.

Contents

To my family: past, present, and future

Acknowledgments

I am endlessly grateful to the many advisors, colleagues and friends who have supported me throughout my program. Principle among these is my advisor, Prof. Mikhail (Misha) Lukin. Misha has been invaluable as a teacher, mentor and advisor throughout my PhD. His incredible intuition about AMO systems and ability to always find new angles to approach problems and push experiments further is a constant inspiration. I truly appreciate the trust Misha has for his students, giving us the freedom to investigate and explore every tangent in our project, no matter how crazy they may sound. I would also like to thank my advising committee, Prof. Ronald Walsworth and Prof. Efthimios (Tim) Kaxiras. Ron's enthusiasm for diamond color centers is one of the things that inspired me to this field of research, and his experience and advice with these systems have been immensely helpful. Tim's mastery of solids and crystals helped my understanding of diamond group theory, and developed my intuition for defect centers. Finally, I have had the pleasure to collaborate with a number of other groups as part of this project, who have been instrumental in pushing this project to its limits. First, this project would not have been possible without the nanofabrication expertise of Prof. Marko Lončar. His willingness to collaborate and share experience with diamond nanophotonics is deeply appreciated, and it has been a pleasure working with him and his students over the years. Similarly, I a deep gratitude to Prof. Fedor Jelezko, who's excitement and knowledge of diamond color centers sparked the start of this project. Fedor and his students introduced our team to the silicon-vacancy center (as well as its cousins the germanium-vacancy and tin-vacancy), and their friendly collaborations in discovering and understanding the underlying physics of these color centers has led to many fruitful discussions and publications. Finally, I would like to thank Prof. Hongkun Park and Prof. Dirk Englud, who have provided helpful discussions and ideas which are helping to push this project forward. Their expertise with nanophotonic systems and networks will surely prove vital for turning our dreams of a Cambridge-area quantum network into reality.

I have had the great pleasure of working with many brilliant and enthusiastic scientists here at Harvard and shared many late night discussions and early morning bagels which have helped to keep me motivated and excited about physics. First, I would like to thank the entire SiV sub-team. I had the pleasure of working on this project nearly from inception, and cannot be more grateful to Alp Sipahigil, Ruffin Evans, and Denis Sukachev for accepting me onto the team. Alp has been an incredible mentor, and his mastery and patience in teaching me how to work in a quantum optics lab cannot be overstated. I have been constantly in awe of Alp's ability to overcome any experimental challenge, and his enthusiasm and dedication has shaped my understanding of what it means to be a scientist. Ruffin has also been wonderful, advising me in nearly all aspects of science, from photonics, to lab organization, to career philosophy and life optimization. Ruffin's unique combination of pragmatism and humor, especially in the face of experimental challenge continue to inspire me. Denis has been everything one could ask for in a postdoc. His deep insight and constant questioning of our experiment pushed and expanded the limits of my understanding. I treasure his advice and mentorship in physics almost as much as I do his discussions of philosophy and inconsistencies in the English language. Since its humble beginnings, I have had the privilege of watching the SiV team grow in size and complexity as the technology developed. Mihir Bhaskar joined the team shortly after, and it has been an absolute joy to learn and develop the SiV platform with him. Mihir's perseverance and intuition with the SiV nanophotonics was instrumental in developing the multi-qubit platform. Leading the next generation of this project are Bart Machielse, David Levonian, Ralf Riedinger, Can Knaut, Pasha Stroganov, Erik Knall, Rivka Bekenstein and Conner Williams. I am continually impressed by their initiative and dedication, and look forward to hearing about their many future developments and projects.

Next, I would like to thank the myriad of other scientists who have generously provided support, both academically and extracurricularly. Mike Burek, Haig Atikian, Srujan Meesala, Bart Machielse, Stefan Bogdanovic, Eric Puma, and Graham Joe have carried the spirit of collaboration between the Lukin and Lončar groups. The open discussion of new developments and technical challenges between our projects has been a significant reason for our many achievements. Joonhee Choi, Harry Zhou, Peter Maurer, Renate Landig, Arthur Safira, Aaron Kabcenell, Emma Rosenfeld, Jan

Gieseler, Elana Urbach, Tamara Šumarac, Alexei Bylinskii, Kristine Rezai, Nabeel Aslam, Kristiaan De Greve, and Bo Dwyer represent the considerable nitrogen-vacancy effort in our group. I thank them for their insights and discussion in understanding the differences and similarities between NV and SiV systems, as well as for their advice on nanodiamond and biological applications. I would like to thank my office mates Tim Milbourne, Po Samutpraphoot, and Elana Urbach for commiserating and celebrating in the many challenges and victories I experienced over the years. I would also like to thank the 2019 PS12b teaching team Bo Dwyer, Camille Gomez-Laberge, and Anna Klales, who made teaching undergraduate labs a fun and fulfilling experience. Lastly, I would like to thank the following staff: Lisa Cacciabaudo, Jacob Barandes, Silke Exner, Adam Ackerman, Karl Coleman, Clare Ploucha, Sam Dakoulas, Jim MacArthur, Adam Graham, and Sasha Zibrov who have helped support both me and this project.

Finally, I would like to thank the many friendships forged and strengthened over my time in Cambridge. I would like to thank the Lukin group volleyball team: Alexei, Bart, Can, DaLi, David, Denis, Dom, Erik, Gio, Harry L., Harry Z. Iris, Mihir, Stefan, Trond, for proving a fun and welcoming way to spend Boston summers. I would also like to thank my tabletop group: Aaron, Alex, Cameron, Chris, Dan, Elana, Evelyn, Melissa, Kimee, and Tim for entertaining my strange hobbies and providing countless hours of creativity and entertainment. Additionally, I would like to thank the entirety of Big Red Boston. Their support and friendship, both new and old, over the last six years really turned Boston into a home away from home. The community they fostered truly is one-of-a-kind, and I cannot adequately express how lucky I was to be a part of it.

I would not be who I am today without all the love and support I have received from my family. Their patience and advice in watching me grow is the foundation this thesis was built on. Lastly, a special thanks to Kimee Moore. Her unyielding enthusiasm and optimism is infectious and has filled the past few years with joy.

This thesis was typeset using the Dissertate LaTeX template, released under the permissive AGPL license.

Citations to previously published work

Chapter 1 in its entirety has been published as

"All-optical nanoscale thermometry with silicon-vacancy centers in diamond"

C. T. Nguyen, R. E. Evans, A. Sipahigil, M. K. Bhaskar, D. D. Sukachev, V. N. Agafonov, V. A. Davydov, L. M. Kulikova, F. Jelezko, and M. D. Lukin Appl. Phys. Lett. 112, 203102 (2018)

Reproduced with the permission of AIP Publishing

Chapter 2 in its entirety has been published as

"Silicon-vacancy spin qubit in diamond: A quantum memory exceeding 10 ms with single-shot state readout"

D. D. Sukachev, A. Sipahigil, C. T. Nguyen, M. K. Bhaskar, R. E. Evans, F. Jelezko, and M. D. Lukin Phys. Rev. Lett. 119, 223602 (2017)

Chapter 3 in its entirety has been published as

"An integrated nanophotonic quantum register based on silicon-vacancy spins in diamond"

C. T. Nguyen, D. D. Sukachev, M. K. Bhaskar, B. Machielse, D. S. Levonian, E. N. Knall, P. Stroganov, C. Chia, M. J. Burek, R. Riedinger, H. Park,

M. Lončar and M. D. Lukin Phys. Rev. B 100, 165428 (2019)

Chapter 4 in its entirety has been published as

“Quantum network nodes based on diamond qubits with an efficient nanophotonic interface”

C. T. Nguyen, D. D. Sukachev, M. K. Bhaskar, B. Machielse, D. S. Levonian, E. N. Knall, P. Stroganov, R. Riedinger, H. Park, M. Lončar and M. D. Lukin Phys. Rev. Lett. 123, 183602 (2019)

0

Introduction

0.1 Introduction to quantum networks

Since its development over a century ago, quantum mechanics has proved to be an invaluable tool for describing previously unexplainable paradoxes about the universe, and enabling new technologies. A quantum mechanical description of the atom for example, resolved the stability paradox of earlier models[1], and laid the groundwork for a band theory of solids, ultimately enabling the development of modern semiconductor electronics[2]. Similarly, advances in pharmacology are built on the backbone of DFT, the quantum mechanical description of how electrons organize in molecular bonds[3]. Despite these examples, many of the interesting and unique features of quantum mechanics, such as superposition and entanglement remain a largely untapped resource for new technologies due to the difficulties of creating and controlling such exotic states. Many groups around the world are currently investigating a wide range of precisely controlled quantum systems in order to harness these properties and revolutionize modern technology.

Perhaps the most well established of these platforms is that of trapped atoms and ions. These systems are well understood both from a theoretical and experimental point of view, resulting in unprecedented levels of control over the many available degrees of freedom[4,5,6]. Large arrays of neutral atoms trapped in optical lattices and tweezer arrays have enabled powerful quantum simulators, capable of probing many-body dynamics and simulating complex physical problems[7,8,9]. Unfortunately, current implementations of these systems are limited to tens of qubits[5,10], typically due to the technical complexities involved in trapping and controlling that many individual atoms.

In light of this, investigations into solid-state qubits, which don't need to be individually trapped and cooled, are a particularly promising direction for building quantum technologies[11]. These systems have the advantage of being highly engineered: their couplings and connectivity can be defined by the nanofabrication process, and they can be produced *en-masse* using established semiconductor fabrication techniques. Due to this rapid development, superconducting qubit devices have demonstrated that they can perform some calculations faster than the best available classical computers; a benchmark known as ’quantum supremacy’[12]. Once again however, these chips are currently limited to tens of qubits[12], due to undesirable cross-talk between qubits.

In order to scale up these quantum systems to the thousands (or millions) of qubits necessary for universal, fault-tolerant quantum computing, new methods for connecting and routing quantum information are paramount[13]. In analogy to classical networking, quantum networks could serve as a bus to route information between independent ’cores’ of small quantum processors. Furthermore, by connecting nodes separated by long distances, quantum networks could serve as the backbone of a quantum internet[14,15], which would enable many new technologies and applications including unconditionally secure communication[16], enhanced metrology[17,18], and ‘blind’ quantum computing[19]. Similar to classical telecommunications, where information is transmitted globally at high bandwidth through optical fibers, single optical photons are a natural choice for transmitting quantum information and connecting remote nodes together. Thus, a functional quantum network requires nodes which consist of:

1. small-to-intermediate scale quantum processors

2. which can store and process quantum information with high fidelity
3. and are efficiently interfaced with single photon transmitters.

Despite this relatively minimal set of requirements, very few platforms are capable of satisfying all of these requirements simultaneously. Trapped atoms in optical cavities, for example, have demonstrated atom-photon gates[20,21] as well as gates between two atoms mediated by cavity interactions[22], but combining these two experiments to create a quantum network node remains an outstanding chalelnge. In comparison, self-assembled quantum dots in GaAs, an established solid-state system, have been incorporated into nanophotonic structures, enabling an efficient on-chip spin-photon interface[23,24], but have yet to demonstrate long quantum storage times, limited primarily by the dense bath of nuclear spins intrinsic to the host crystal[25].

Finally, color centers in diamond have emerged in recent decades as especially promising candidates for building quantum network nodes. The most famous of which, the nitrogen-vacancy center (NV), has been shown to be an exceptional quantum system capable of interfacing with registers of ten qubits with extremely long coherence times[26]. Pioneering experiments with NVs have even demonstrated long-range entanglement between NVs, with rates primarily limited by their poor interface to optical photons[27].

Motivated by the successes of systems like the NV, there is significant scientific and technological motivation for finding new color centers with improved optical and coherence properties for the purposes of quantum networking and computing. Already, many new promising candidates are emerging, including novel color centers in diamond[28,29,30,31] and others[32,33,34].

0.2 The silicon-vacancy color center in diamond

Among these new platforms, the silicon-vacancy color center in diamond (SiV) stands out as particularly promising for quantum networking applications. Initially inspired by the observation of bright, narrow-band single-photon emission at room temperature[28,35], investigations of the SiV developed rapidly and established this as a result of its relatively unique D_{3d} symmetry[36,37], which renders the optical transitions insensitive to electric fields to first order[38]. This insensitivity protects SiVs from much of the disorder and noise typically present in nanostructures, and enables an efficient atom-photon interface via nanophotonic cavity quantum electrodynamics[39,40,41]. Furthermore, the SiV has a rich energy spectrum, described by a single spin-1/2 hole with both spin and orbital degrees of freedom.

Unfortunately, despite SiV insensitivity to electric field noise, coherence times for SiVs have been limited to hundreds of nanoseconds[42,43,44,45,46]. Attempts to explain this phenomenon propose phonon coupling between orbital states which introduce additional depolarization and dephasing mechanisms[44]. An understanding of this process is necessary to unlock the full potential of the SiV for technological applications such as quantum networks.

0.3 Overview of this thesis

This thesis builds on ~ 5 years of previous experiments establishing the SiV as a superior optical emitter, and work to understand and control the phonon mechanisms preventing the use of SiV as a quantum memory. Chapter 1 demonstrates one consequence of phonon coupling to the SiV, where electron-phonon processes manifest as temperature-sensitive optical transitions. This observation confirms previous results[44] and motivates the preceding chapters. It should be noted however that these optical transitions are remarkably sensitive (with $\Delta\lambda/\Delta T = 6.8(1)\,\mathrm{GHz\,K^{-1}}$, and stable (properties in 200 nm nanodiamonds deviate by less than 1% between samples). By carefully measuring the SiV spectrum as a function of temperature, we demonstrate an all-optical, calibration-free thermometer which can potentially be used as an integrated temperature sensor and actuator on the nanoscale.

The remaining chapters focus on improving the prospects of quantum information processing with the SiV by mitigating the effect of phonon-induced decoherence. Namely, by cooling SiVs below 500 mK in a dilution refrigerator, it was theorized that relevant phonon modes could be frozen out, allowing the SiV to be a quantum memory comparable to that of the NV[44]. In chapter 2, we outline the experimental results of this proposal, which extend the coherence time of SiVs by five orders of magnitude compared to previous studies using SiVs. We further show that the SiV coherence properties do not scale identically to the NV, suggesting that SiVs in bulk are not limited by the same noise baths. Even so, this work establishes the SiV as a potential qubit platform, and serves as a testbed for a set of control tools necessary for quantum control: Single-shot initialization and readout of the qubit, and coherent single-qubit gates.

In chapter 3, we place these SiV qubits into nanophotonic cavities to enable efficient atom-photon interactions. We outline fabrication and experimental upgrades to previous reports[39,40,41], and outline the technical considerations for operating SiV cavity QED experiments in a dilution fridge. The quantum control toolbox is updated to include new considerations arising from the nanophotonics platform, including generation of bipartite entangment in the form of spin-photon Bell states.

Chapters 3 and 4 then introduce a second qubit to this platform based on nearby ^{13}C nuclear spins and demonstrate electron-nuclear Bell states. These measurements finish characterizing a fully functioning SiV quantum network node, constituting of an interacting multi-qubit quantum register with long coherence times and a deterministic spin-photon interface. We highlight the capabilities of this node in chapter 4 by generating spin-spin and spin-photon Bell states in a single device, as well performing one of the crucial functions of a node: mapping a photonic qubit onto an atomic memory. This demonstration is the first step towards a quantum internet capable of distributing and purifying entanglement over long distances.

Finally, chapter 5 concludes by outlining several immediate technologies enabled by this device, including memory-enhanced distribution rates for secure quantum keys. We also outline several potential improvements to this technology, including deterministic multi-qubit registers, robust packaging, and single-sided cavity design, which will open the door to many new applications.

1

All-optical nanoscale thermometry with silicon-vacancy centers in diamond

This chapter has been published as

“All-optical nanoscale thermometry with silicon-vacancy centers in diamond”

C. T. Nguyen, R. E. Evans, A. Sipahigil, M. K. Bhaskar, D. D. Sukachev, V. N.

Agafonov, V. A. Davydov, L. M. Kulikova, F. Jelezko, and M. D. Lukin Appl. Phys. Lett. 112, 203102 (2018)

Reproduced with the permission of AIP Publishing

1.1 Introduction

Luminescent thermometers[47] utilize the sensitivity of optical transitions to temperature in order to probe thermal variations on the nanometer scale. Although these systems have lower sensitivity than, for example, scanning probes[48,49], they are non-invasive, enabling a broad class of experiments including *in vivo* biological measurements[47,50]. Current platforms for luminescent thermometry are often limited by intrinsic emitter properties: broad inhomogeneous distributions,[51,52], weak transition dipoles,[49,53,54,55], photobleaching[56,57] and small Debye-Waller factors[58]. These properties result in thermometers which require long acquisition times[51,54,55,58] and typically require individual calibration[56,57,58,59,60] in order to measure temperature variation.

Diamond based platforms have proven to be versatile for a wide range of sensing applications. The diamond crystal is chemically inert, making it naturally robust to extreme environments, and biologically compatible, capable of being located within nanometers of the sensing volume. Nitrogen vacancy color centers (NVs) in diamond, for example, utilize microwave and optical control to measure temperature[58,60] (as well as magnetic[61,62], electric[63], and strain[64] fields) with nanoscale resolution and low uncertainty. While thermometry with NVs features high sensitivity, it requires simultaneous optical and microwave control, and due to inhomogeneous broadening, each emitter must be individually calibrated before use as a thermometer. The silicon-vacancy color center (SiV) in diamond has recently emerged as a superior optical emitter, belonging to a family of interstitial defects whose favorable optical properties arise from inversion symmetry[29,30,65]. SiVs have stable optical properties featuring bright, narrowband emission, allowing for fast, accurate measurements which are consistent between emitters. This means that SiVs can be used as high-resolution, non-photobleaching thermometers without the need for calibration. In this chapter, we take advantage of the SiV's zero-phonon line (ZPL) frequency, linewidth, and quantum efficiency temperature sensitivity to realize all-optical thermometry with SiV ensembles both in bulk and in nanodiamonds.

1.2 Photoluminescence thermometry

Following previous studies[44,66,67,68], we first focus on the photoluminescence (PL) spectrum of an ensemble of SiVs in bulk diamond at room temperature [Fig. 1.1(a,b)]. We fit the ZPL spectrum[69,70] and use the ZPL peak position as the thermometry signal (PL thermometry appendix A). Although the SiV ZPL frequency shifts nonlinearly from 5K to room temperature[44,66,67,68], for a small range (295 ± 5K), it deviates by less than 1% from the linear approximation [Fig. 1.1(c)]. We measure

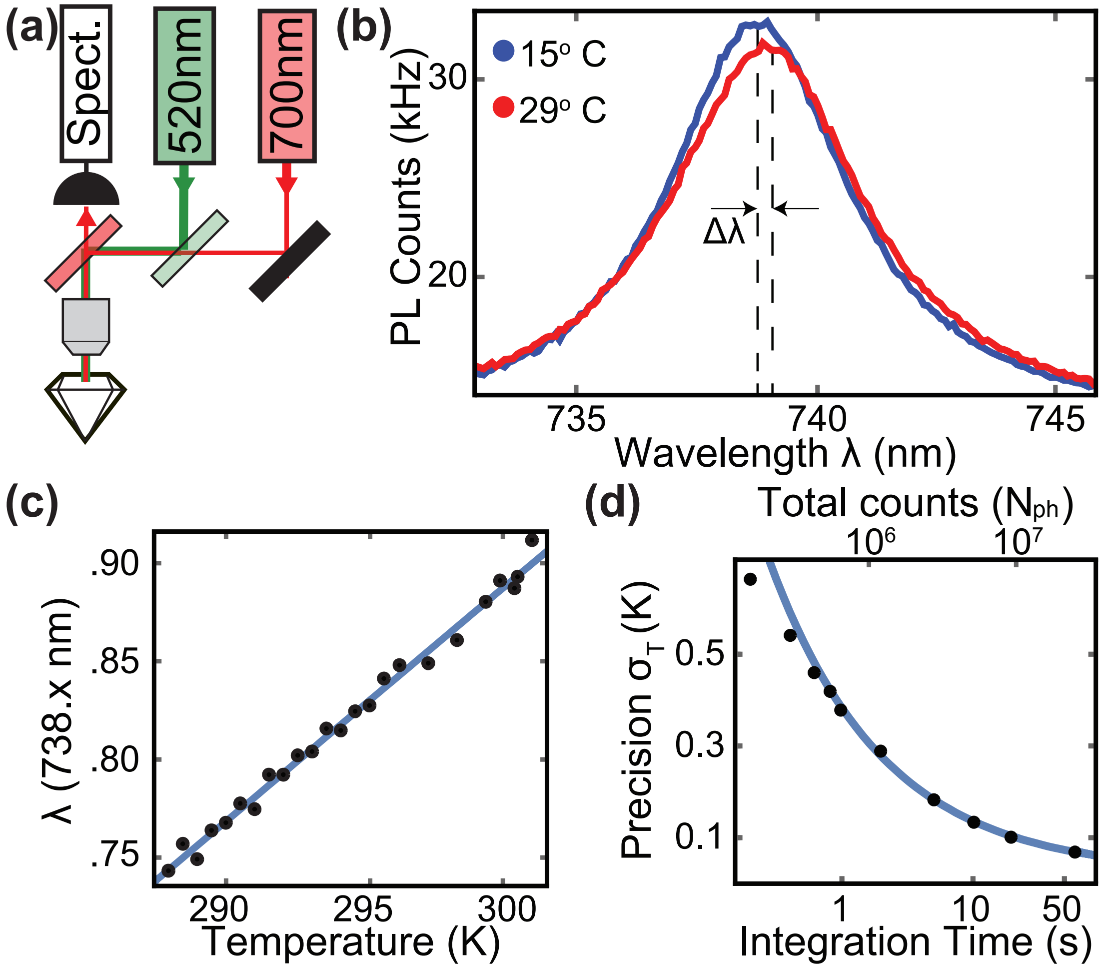

Figure 1.1: SiV PL thermometry in bulk diamond. **a.** Diamond with a high SiV density is excited off resonance and SiV fluorescence spectra are measured A. **b.** Typical spectra at $15\,°\mathrm{C}$ (blue) and $29\,°\mathrm{C}$ (red). The ZPL peak shifts to the red at higher temperatures. **c.** Peak position as a function of temperature. The peak sensitivity to tempearature is $\Delta\lambda/\Delta T = 0.0124(2)\mathrm{nm\,K^{-1}}$ $(6.8(1)\,\mathrm{GHz\,K^{-1}})$. Error bars $(\pm 1\sigma)$ for this measurement are the size of the data points. **d.** Temperature uncertainty (σ_T) of the thermometer as a function of integration time. Solid line is a fit to shot noise $1/\sqrt{N_{ph}}$. The uncertainty is $360\,\mathrm{mK}/\sqrt{\mathrm{Hz}}$.

the sensitivity of the peak wavelength to temperature, $\Delta\lambda/\Delta T = 0.0124(2)\mathrm{nm}\,\mathrm{K}^{-1}$ $(6.8(1)\,\mathrm{GHz}\,\mathrm{K}^{-1})$, consistent with previous low-resolution measurements[44,66,67,68]. The origin of this shift is thermal lattice expansion which reduces the orbital overlap between dangling carbon bonds[44].

To estimate the precision of SiV thermometry, we measure uncertainty in the peak position as a function of integration time at a fixed temperature (Fig. 1d), and extract a temperature uncertainty $\sigma_T = 360\,\mathrm{mK}/\sqrt{\mathrm{Hz}}$, giving 70 mK temperature precision after 50 s integration time. This measurement uncertainty follows the shot-noise limit $1/\sqrt{N_{ph}}$ [Fig. 1.1(d)], suggesting that the precision can be improved by increasing photon collection rates from the sample, either by increasing SiV density[71,72] or by improving collection efficiency. The stability of this thermometer is also measured by keeping the sample stage at a fixed temperature (as measured by an external temperature sensor) and recording the peak position every minute for 2 hours. In this way, we extract a repeatability uncertainty of 152 mK for a 10 s integration time, which is comparable to the measured temperature uncertainty for the same integration time.

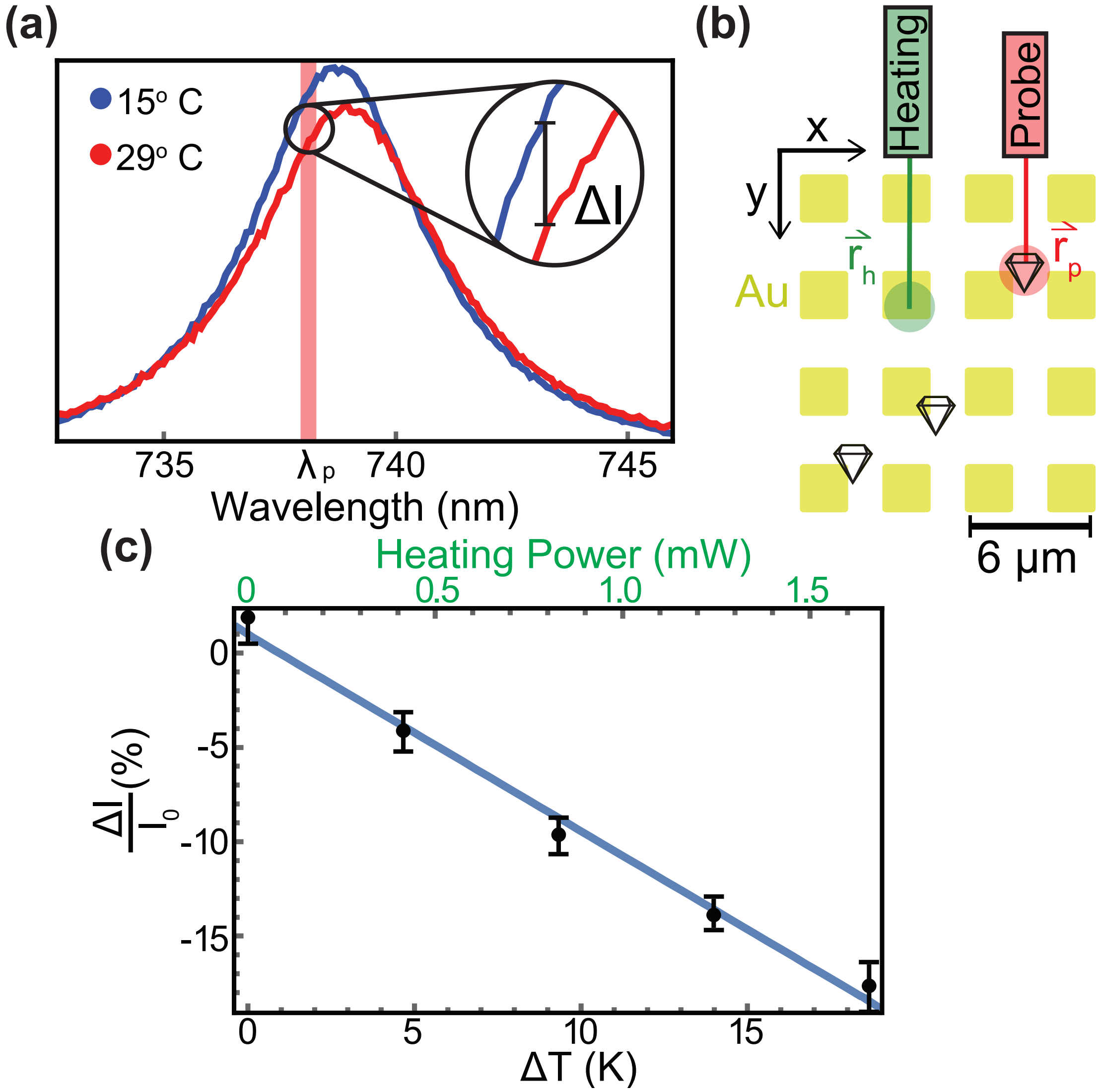

Figure 1.2: SiV PLE thermometry with nanodiamonds **a.** Scheme for PLE thermometry: Excite SiVs near resonance at λ_p and measure PLE fluorescence as a function of temperature (ΔI). **b.** $\sim 200\,\mathrm{nm}$ nanodiamonds are drop cast onto a gold targeting grid. Heat is applied via a green laser at position $\mathbf{r_h}$, which is probed via the nanodiamond at position $\mathbf{r_p}$. **c.** Lock-in fluorescence contrast vs. temperature for PLE thermometry. The heating laser power P_h is modulated, and PLE fluorescence is measured. The signal sensitivity to temperature is $\frac{\Delta I}{I_0}/\Delta T = 1.3(1)\%/\mathrm{K}$ with an uncertainty of $521\,\mathrm{mK}/\sqrt{\mathrm{Hz}}$. $\Delta T = T_{P_h \neq 0} - T_{P_h=0}$.

1.3 Photoluminescent excitation thermometry in nanodiamonds

While measurements in bulk confirm that SiVs can be used for thermometry, many applications require localized probes for *in situ* measurements. To address this, we next demonstrate nanometer-scale thermometry using SiV-containing nanodiamonds. For these experiments, we use 200(70) nm high-pressure high-temperature nanodiamonds grown with silicon included in the growth chamber A. The count rates in these nanodiamonds are $200 - 400$ kHz, suggesting that they contain fewer SiVs (< 10) in the probe volume than for the bulk diamond (~ 100). With a smaller photon flux, longer integration times are needed in order to achieve the same precision. For our spectrometer CCD (Synapse BIUV), we have a readout noise of ~ 10 counts per bin and a total of 1500 bins, which limits the detection bandwidth to 0.6 Hz for 10:1 signal to noise using the measured count rates, making the measurement sensitive to slow drifts. To overcome this limitation, we introduce a different thermometry technique based on photoluminescence excitation (PLE) spectroscopy, the near-resonant excitation of the SiV ZPL transition.

For PLE thermometry, instead of exciting SiVs off resonance and measuring the ZPL spectrum, we excite on resonance (738 nm at room temperature), and collect emission into the phonon sideband, effectively probing the absorption cross-section of the ZPL as a function of temperature. Physically, increasing the temperature red-shifts the ZPL peak and reduces the peak intensity when the SiVs are excited below saturation, caused by non-radiative decays from the excited state becoming more favorable at higher temperatures[44]. Both of these effects contribute to a reduced absorption cross-section blue of the resonance peak. We therefore excite the nanodiamonds at an experimentally determined wavelength (λ_p) of maximum contrast [Fig. 1.2(a)]. For this technique, we use an avalanche photodiode (APD) with $\sim$ 50 dark counts per second, giving a detection bandwidth of 200 Hz, much larger than PL thermometry for the same signal to noise. This high-bandwidth measurement also enables lock-in techniques (described below), which further mitigate slow experimental drifts.

We demonstrate PLE thermometry by patterning an array of 2 m wide, 50 nm thick gold pads onto a glass slide using photolithography and drop casting an isopropyl alcohol solution of nanodiamonds containing SiVs [Fig. 1.2(b)]. The gold pads absorb light at 520 nm[73] and act as a local heat source when illuminated. A nanodiamond at position $\mathbf{r_p}$ [Fig. 1.2(b)] is continually monitored while the power P_h of a heating laser applied at $\mathbf{r_h}$ is modulated. This gives rise to a PLE thermometry signal ($\frac{\Delta I}{I_0}$) defined by the normalized difference in counts between $P_h = 0$ and $P_h \neq 0$.

Unlike in PL thermometry, here we modulate the heat source rapidly in order to utilize lock-in detection. Because of this, the sample never reaches a global thermal equilibrium, necessitating a different calibration technique A. The temperature sensitivity of the intensity signal, $\frac{\Delta I}{I_0}/\Delta T = 1.3(1)\%/\mathrm{K}$[Fig. 1.2(c)], varies by less than 1% between different nanodiamonds. Therefore, SiV incorporated nanodiamonds do not need to be individually calibrated in order to be a precise relative thermometer. The temperature uncertainty is also measured to be $521\,\mathrm{mK}/\sqrt{\mathrm{Hz}}$ which, in contrast to bulk measurements, is not shot noise limited, but saturates at 700 mK. This is most likely limited by residual fluorescence noise not rejected by the lock-in technique. Although we should be able to operate at a 200 Hz lock-in modulation frequency based on count rates, the optimal sensitivity occurs around 80 Hz, suggesting the bandwidth for this measurement is limited by the speed at which we can modulate the heat source. While the uncertainty of this technique is higher than that measured for bulk diamond, it involves probing a much smaller volume ($\sim 0.004\,\mathrm{m}^3$ compared to $\sim 4\,\mathrm{m}^3$ in bulk). When normalized by sensor volume, this technique performs twenty times better than PL thermometry.

Finally, we scan the position of the heating laser, $\mathbf{r_h}$, across our sample and measure the temperature response at the probe position, $\mathbf{r_p}$. Whenever the heating laser passes over a gold pad, the temperature at the nanodiamond increases, leading to the observed pattern in [Fig. 1.3(a)]. This map is a measurement of the temperature difference ΔT at $\mathbf{r_p}$ induced by the heating laser at $\mathbf{r_h}$. According to the steady-state heat equation for a point-source load in half-space[74], we expect $\Delta T(r) = \frac{\epsilon P t a}{4\pi k |r - r_0|}$, where P is the applied laser power, t is the transmission efficiency of the objective, a is the absorption of a 50 nm gold pad illuminated at 520 nm, and k is the thermal

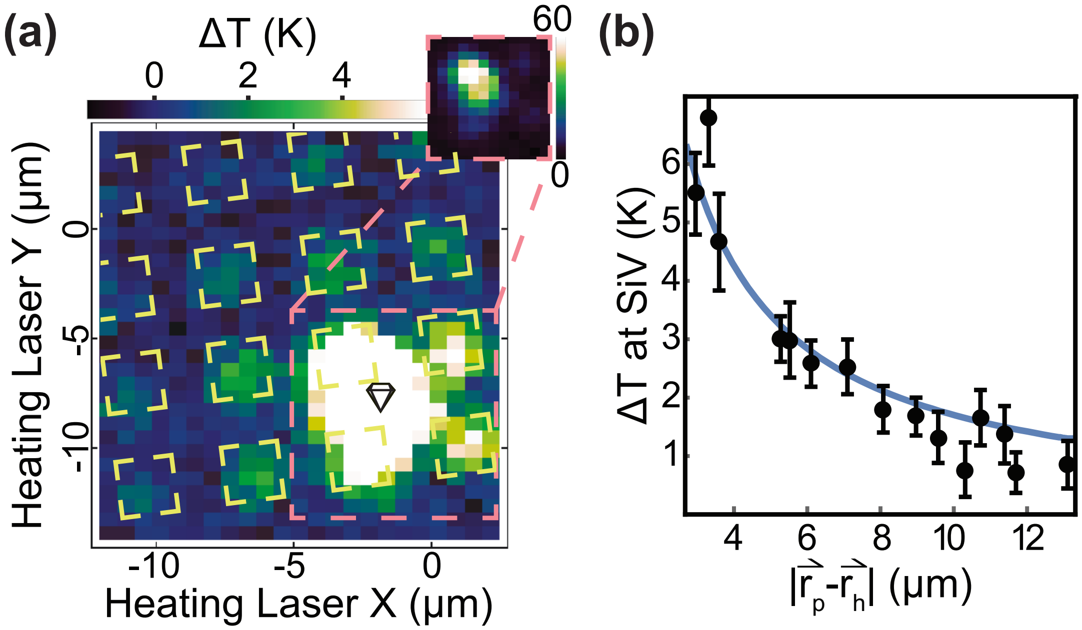

Figure 1.3: Measuring local heating via PLE thermometry **a.** Away from the nanodiamond, heating corresponds to the gold array (overlaid boxes). Near the nanodiamond (inset), off-resonant fluorescence from the heating laser dominates the signal. **b.** Temperature change on gold pads vs. their distance from the nanodiamond. These points follow a $1/|\mathbf{r_p} - \mathbf{r_h}|$ dependence as expected from solving the steady-state 2D heat equation[74], and are consistent with the absorption of a $50\,\mathrm{nm}$ gold film at $520\,\mathrm{nm}$[73].

conductivity of the glass slide. This can be seen in [Fig. 1.3(b)]. Due to fabrication imperfections, it's possible for a to deviate from the theoretical value. We account for this with a free parameter $\epsilon = 0.7$. For these measurements, the spatial resolution is limited by the nanodiamond size and the precision with which one can focus the heat source. Although not fundamental, these experiments were limited by the latter, which is the confocal microscope's optical resolution (~300 nm). By using plasmon resonances of gold nanoparticles[60] as a heat source and smaller nanodiamonds, this resolution can be improved by an order of magnitude.

1.4 Conclusion and outlook

This chapter demonstrates nanoscale thermometry based on SiV centers in diamond and achieves a temperature uncertainty of $360\,\mathrm{mK}/\sqrt{\mathrm{Hz}}$ in bulk diamond and $521\,\mathrm{mK}/\sqrt{\mathrm{Hz}}$ in 200 nm-sized nanodiamonds. The uncertainty of PL thermometry follows shot-noise limited scaling, which is not the case for PLE thermometry. We therefore infer that systematic effects dominate the uncertainty of PLE thermometry at longer integration times. This is most likely due to an inability to fully reject fluorescence intensity noise in the lock-in measurement. To address this, one can modify the lock-in technique by modulating two resonant lasers placed on the red and blue sides of the ZPL transition. Since this method does not rely on modulating the sample temperature, this modulation can be done at higher frequencies, which should further reduce noise in the measurement and improve the precision of this thermometry technique. Currently, each nanodiamond has $<$ 10 SiVs, so a straightforward method for reducing the measurement time would be to use nanodiamonds with higher SiV density. Unlike commercial nanodiamonds, which naturally contain many 1000s of NV centers[60], SiV nanodiamonds must be specifically fabricated, and thus are not widely available.

SiV thermometry features several unique benefits compared to other luminescent thermometers, especially for biological applications. The all-optical scheme eliminates the necessity of microwaves, and operates at low laser powers ($\sim$ 100 W resonant laser power), reducing measurement induced heating and potential damage to the target under investigation. In addition, SiVs have a narrow inhomogeneous distribution, which makes PL and PLE thermometry with SiVs effective as a thermometer even without individual calibration.

Other systems for luminescent thermometry[52,54,55,75] also report absolute temperature uncertainties on the order of 1 Kelvin; however, due to their low spectral density and weak transition dipoles, these measurements typically require integration for several minutes to achieve sub-Kelvin uncertainty. Our approach is comparable in probe size to these techniques and achieves a similar absolute uncertainty, but does so in significantly less time. This increased speed is crucial for many practical applications. For example, typical intracellular processes occur on the 1s timescale, which can be resolved with our technique[76]. Moreover, the SiV emission lies in the optical window for cellular imaging, a frequency-band of high transmission for a variety of biological material typically between 650 nm to 1350 nm[77], rendering SiV thermometry a promising candidate for biological *in vivo* applications[47,50]. Finally, recent studies show that color centers in nanodiamonds can also be used to vary the temperature of a local environment via optical refrigeration[78]. Combining SiV thermometry with this technique would allow these nanodiamonds to be an integrated temperature sensor and actuator at the cellular level.

2

The silicon-vacancy spin qubit in diamond: quantum memory exceeding ten milliseconds and single-shot state readout

This chapter has been published as

"Silicon-vacancy spin qubit in diamond: A quantum memory exceeding 10 ms with single-shot state readout"

D. D. Sukachev, A. Sipahigil, C. T. Nguyen, M. K. Bhaskar, R. E. Evans, F. Jelezko, and M. D. Lukin Phys. Rev. Lett. 119, 223602 (2017)

2.1 Introduction

Quantum networks require the ability to store quantum information in long-lived memories, to efficiently interface these memories with optical photons and to provide quantum nonlinearities required for deterministic quantum gate operations [79,80]. Even though key building blocks of quantum networks have been demonstrated in various systems[81,82], no solid-state platform has satisfied these requirements. Over the past decade, solid-state quantum emitters with stable spin degrees of freedom such as charged quantum dots and nitrogen-vacancy (NV) centers in diamond have been investigated for the realization of quantum network nodes[83]. While quantum dots can be deterministically interfaced with optical photons[23], their quantum memory time is limited to the s scale [84] due to interactions with their surrounding nuclear spin bath. In contrast, NV centers have an exceptionally long-lived quantum memory[85] but suffer from weak, spectrally unstable optical transitions[86]. Despite impressive proof-of-concept experimental demonstrations with these systems[87,88], scaling to a large number of nodes is limited by the challenge of identifying suitable quantum emitters with the combination of strong, homogeneous and coherent optical transitions and long-lived quantum memories.

The negatively-charged silicon-vacancy (SiV) has recently been shown to have bright, narrowband optical transitions with a small inhomogeneous broadening[35,38].

The optical coherence of the SiV is protected by its inversion symmetry[89], even in nanostructures[39]. These optical properties were recently used to show strong interactions between single photons and single SiV centers and to probabilistically entangle two SiV centers in a single nanophotonic device[40]. At 4 K, however, the SiV spin coherence is limited to ∼100 ns due to coupling to the phonon bath, mediated by the spin-orbit interaction[42,43,44,45,46].

In this chapter, we demonstrate high-fidelity coherent manipulation and single-shot readout of individual SiV spin qubits in a dilution refrigerator. In particular, we extend the coherence time of the SiV electronic spin by five orders of magnitude to 13 ms by operating at 100 mK [*].

2.2 SiV physics below 500 mK

The key idea of the present work can be understood by considering the energy level diagram of the SiV [Fig. 2.1(a)]. The ground state of the SiV is split by spin-orbit interaction and crystal strain into a lower branch (LB) and an upper branch (UB) separated by Δ_{GS}. Each branch comprises two degenerate spin sublevels[37]. Application of a magnetic field lifts the spin degeneracy and allows the use of the spin sub-

---

[*] The neutral SiV center (SiV^0) features suppressed phonon-induced dephasing of its spin state[90,91] yielding coherence times of $T_2 \sim 200$ ms in bulk measurements at $T = 15$ K[92]. However, their optical properties, including radiative quantum efficiency, are currently believed to be inferior to those of the SiV^- (SiV)[72], making it challenging to realize an efficient photonic interface.

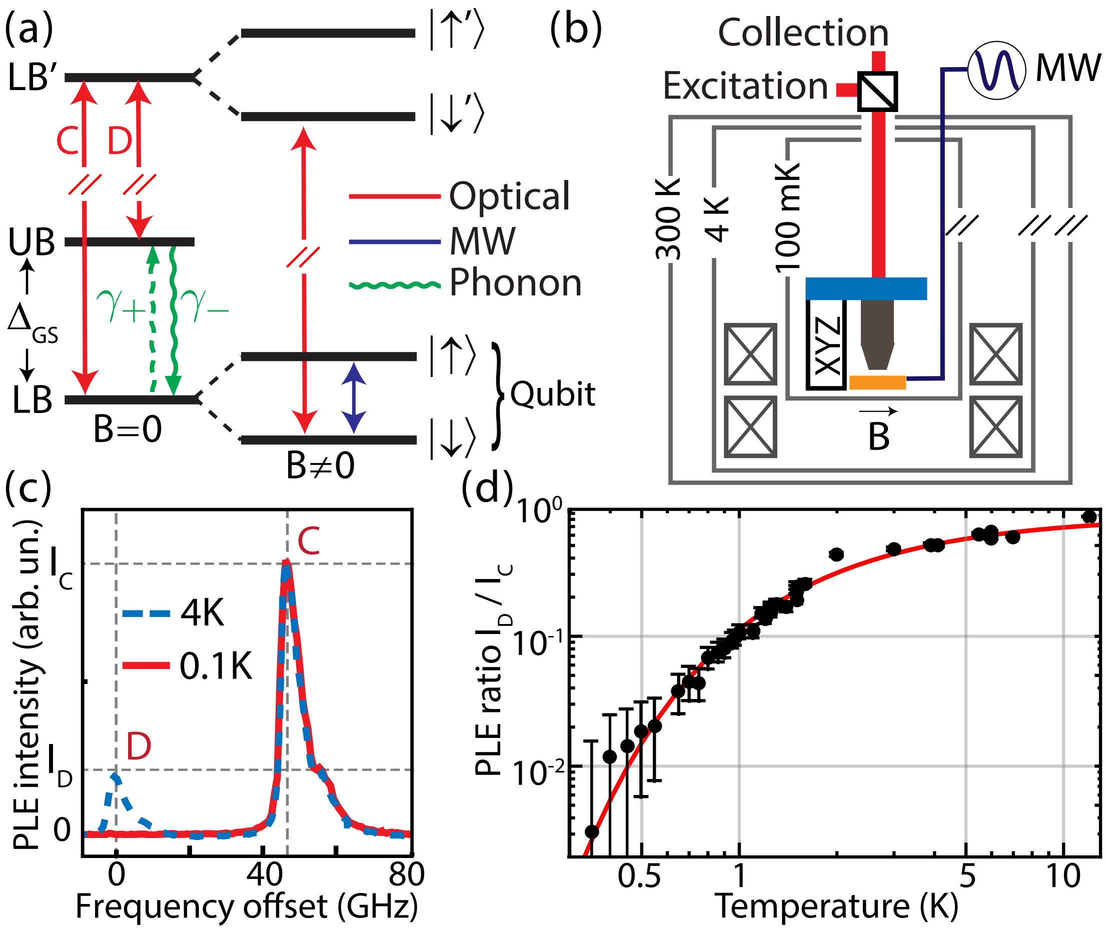

Figure 2.1: (a) SiV electronic structure. Optical transitions C and D connect the lower (LB) and upper (UB) spin-orbit branches to the lowest-energy optical excited state (LB′). Each branch is split into two spin sublevels in a magnetic field $\vec{B}$. Red and blue arrows denote optical and microwave transitions, respectively. γ_+ and γ_- are phonon-induced decay rates. (b) Schematic of the setup. An objective is mounted on piezo positioners to image the diamond sample using free-space optics. The combined system is attached to the mixing plate of a dilution refrigerator and placed inside a superconducting vector magnet. (c) PLE spectra of an SiV ensemble at $B = 0$ for $T = 4\,\mathrm{K}$ and $0.1\,\mathrm{K}$. The peak intensity I_C (I_D) is proportional to the population in the LB (UB). (d) I_D/I_C (and γ_+/γ_-) is reduced at low temperatures, following $e^{-h\Delta/k_BT}$ with $\Delta_{\text{fit}} = 42 \pm 2$ GHz in agreement with the measured $\Delta_{\text{GS}} = 48$ GHz.

levels $|\downarrow\rangle$ and $|\uparrow\rangle$ of the LB as qubit states. At 4 K, the SiV spin coherence is limited to $\sim 100\,\mathrm{ns}$[42,43,44,45,46] due to interactions with the thermal acoustic phonon bath at frequency $\Delta_{\mathrm{GS}} \sim 50\,\mathrm{GHz}$. These interactions result in a relaxation at rates γ_+ and γ_- between the levels in the LB and the UB with different orbitals and the same spin projections as shown in [Fig. 2.1(a)] and destroy spin coherence. By reducing the occupation of phonon modes at Δ_{GS} at lower temperatures, one can suppress the rate γ_+, leaving the spin qubit in a manifold free from phonon-induced decoherence, thereby increasing spin coherence [44].

We investigate SiV properties below 500 mK using a dilution refrigerator with a free-space confocal microscope and a vector magnet as shown in [Fig. 2.1(b)]. Details of the experimental setup for this experiment are outlined in appendix B. We first study the thermal population of the LB and the UB between 0.1 and 10 K using an ensemble of as-grown SiVs (Sample-A in Ref.[90]). We probe the relative populations in the LB and the UB by measuring the ensemble photoluminescence excitation (PLE) spectra of transitions C and D. Transitions C and D are both visible in PLE at 4 K, which suggests comparable thermal population in the LB and UB [Fig. 2.1(c)]. As the temperature is lowered [Fig. 2.1(d)], the ratio of the transition D and C peak amplitudes (I_D/I_C) reduces by more than two orders of magnitude and follows $e^{-h\Delta_{\mathrm{GS}}/k_B T}$[44]. These measurements demonstrate an orbital polarization in the LB of $>$ 99% below 500 mK. At these low temperatures, $\gamma_+ << \gamma_-$ and the qubit states are effectively decoupled from the phonon bath.

2.3 Extending SiV coherence

To investigate the coherence properties of single emitters, we create single SiVs at a depth of $\sim 250\,\mathrm{nm}$ via ^{28}Si ion implantation at a dose of $10^9\ /\mathrm{cm}^2$ and an energy of $380\,\mathrm{keV}$ into two type-IIa ([N]$<5\,\mathrm{ppb}$, [B]$<1\,\mathrm{ppb}$) diamond samples (Element Six). The first sample (Sample-13) has a natural abundance of 1.1% of ^{13}C isotopes with a nuclear spin $I = 1/2$. The second sample (Sample-12) is engineered to have only $10^{-3}\%$ ^{13}C to suppress hyperfine interactions between the spin qubit and the nuclear spin bath[85]. After ion implantation and high-temperature annealing[39], we fabricate a shorted coplanar waveguide on the diamond to drive microwave (MW) transitions between the qubit states [appendix B].

We use spin-selective optical transitions between states $|i\rangle$ and $|i'\rangle$ at frequencies $\mathrm{f}_{ii'}$ $(i = \{\uparrow, \downarrow\})$ [Fig. 2.2(a)] to optically initialize and readout the qubit states. Applying a magnetic field $B \sim 0.5 - 3$ kG allows us to optically resolve these transitions. Figure 2.2(b) shows the PLE spectrum of the spin-selective optical transitions at $4\,\mathrm{K}$ (red circles). These resonances disappear in continuous wave measurements at $100\,\mathrm{mK}$ (blue squares). This effect results from optical pumping of the qubit to the long-lived dark spin state. The central peak originates from off-resonant scattering from the two spin transitions.

To achieve high-fidelity readout of the spin states, it is desirable to scatter photons

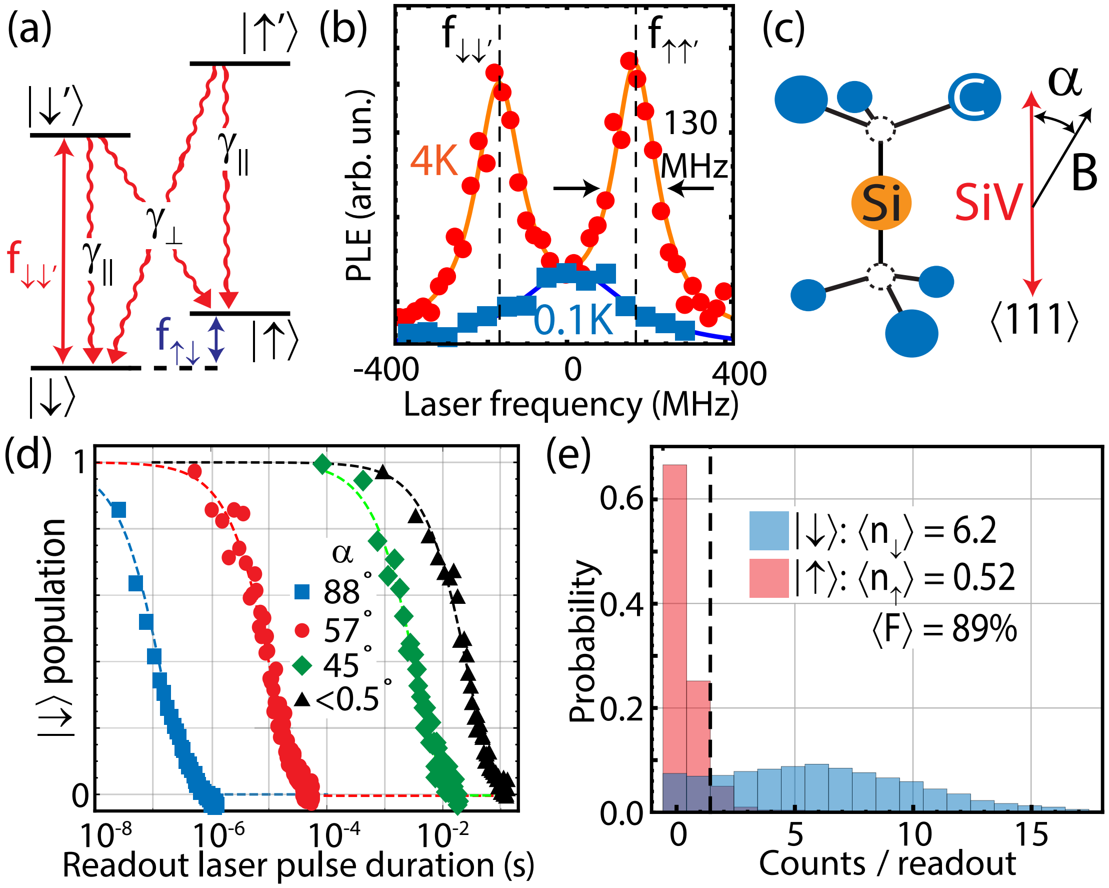

Figure 2.2: (a) Spin-selective optical transitions and branching ratios. f$_{ij}$ is the transition frequency between states i and j. $\gamma_{||}$ and $\gamma_{\perp}$ are spin-conserving and spin-flipping decay rates, respectively; $f_{\uparrow\downarrow}$ is the qubit frequency. (b) PLE spectra measured at $4\,\mathrm{K}$ and $100\,\mathrm{mK}$. (c) Schematic of the SiV molecular structure[37]. α is the angle between the magnetic field $\vec{B}$ and the SiV symmetry axis set by the two lattice vacancies (empty circles) and aligned along the $\langle 111 \rangle$ diamond axis. (d) Optical spin pumping timescale τ measured at different $\vec{B}$. Here, $\{\alpha, B, \tau\} = \{88,$ $2.9\,\mathrm{kG},\ 140\,\mathrm{ns}\}$ for the blue squares; $\{57,\ 3\,\mathrm{kG},\ 10\,\mathrm{s}\}$ for the red circles; $\{45,\ 1.7\,\mathrm{kG},\ 3\,\mathrm{ms}\}$ for the green diamonds and $\{<0.5,\ 2.7\,\mathrm{kG},\ 30\,\mathrm{ms}\}$ for the black triangles. (e) Single-shot spin readout in $B = 2.7\,\mathrm{kG}$. A $20\,\mathrm{ms}$ laser pulse at frequency f$_{\downarrow\downarrow'}$ is used for state readout. A second laser initializes the spin states via optical pumping. Spin readout photon statistics after initialization in state $|\uparrow\rangle$ (red) and $|\downarrow\rangle$ (blue). Average fidelity $F = 89\%$.

many times without causing a spin-flip[93,94]. To obtain such spin-conserving optical transitions, the cyclicity of the transition $\gamma_{\|}/(\gamma_{\perp}+\gamma_{\|})$ can be tuned by varying the angle α of the applied magnetic field with the SiV symmetry axis as shown in Figure 2.2(c)[42]. Figure 2.2(d) shows the optical spin pumping timescale for different α when the transition $\mathrm{f}_{\downarrow\downarrow'}$ is driven near saturation. We extend the optical pumping timescale by more than five orders of magnitude from 100 ns for $\alpha \sim 90$ to 30 ms in an aligned field.

The ability to optically excite the SiV $\sim 10^5$ times without causing a spin-flip [appendix B] enables high-fidelity single-shot readout of the spin state despite the low photon collection efficiency $\left(\sim 10^{-4}\right)$ in the phonon-sideband (PSB). We measure the spin state by driving the $\mathrm{f}_{\downarrow\downarrow'}$ transition near saturation and monitoring fluorescence on the PSB. Figure 2.2(e) shows the readout counts distributions for the spin initialized in state $|{\downarrow}\rangle$ (blue histogram) and $|{\uparrow}\rangle$ (red histogram) using a 150 ms pulse from a second laser at frequency $\mathrm{f}_{\uparrow\uparrow'}$ or $\mathrm{f}_{\downarrow\downarrow'}$, respectively. We detect $\langle n_{\downarrow}\rangle = 6.2$ photons from state $|{\downarrow}\rangle$ and $\langle n_{\uparrow}\rangle = 0.52$ from state $|{\uparrow}\rangle$ in a 20 ms readout window. By choosing a state-detection threshold of $n > 1$ for state $|{\downarrow}\rangle$ and $n \leq 1$ for state $|{\uparrow}\rangle$, we obtain an average readout fidelity of $F = (F_{\uparrow} + F_{\downarrow})/2 = 0.89$ where F_i is the readout fidelity for state i. For the measurements in Figs. 3 and 4, we roughly align the magnetic field with $\alpha < 5$ to operate in an efficient spin readout regime but do not optimize for the highest fidelity at each point. Under these conditions, we measure lifetimes (T_1) of the qubit states exceeding 1 s at 100 mK [appendix B].

The spin readout time ($\sim 10\,\mathrm{ms}$) is currently limited by the low collection efficiency of the setup [appendix B] and by optical pumping to the metastable UB of the ground state [appendix B] with a lifetime of $\sim 200\,\mathrm{ns}$[44]. This readout time can be reduced by several orders of magnitude by adding a repumping laser on transition D [Fig. 2.1(a)] and by using nanophotonic structures to improve the collection efficiency to above 10%[40].

To coherently control the SiV electron spin qubit we use a MW field at frequency $\mathrm{f}_{\uparrow\downarrow}$[46]. In the following experiments, single strained SiVs with $\Delta_{\mathrm{GS}} \sim 80\,\mathrm{GHz}$ are used. When crystal strain is comparable to spin-orbit coupling ($\sim 48\,\mathrm{GHz}$), the orbital components of the qubit states are no longer orthogonal[37], leading to an allowed magnetic dipole transition[46]. This MW transition is allowed for both aligned and misaligned magnetic fields, allowing simultaneous MW control and single-shot readout of the SiV spin.

We focus on single SiVs placed less than $2\,\mathrm{m}$ from the coplanar waveguide to efficiently drive the qubit transition with low MW powers and maintain a steady-state sample temperature below $100\,\mathrm{mK}$. The spin qubit frequency $f_{\downarrow\uparrow}$ is determined using a pulsed optically-detected magnetic resonance (ODMR) measurement as shown in Figures 2.3(a,b). A long laser pulse at frequency $\mathrm{f}_{\downarrow\downarrow'}$ initializes the spin in state $|\uparrow\rangle$ via optical pumping. After a microwave pulse of duration τ, a second laser pulse at $\mathrm{f}_{\downarrow\downarrow'}$ reads out the population in state $|\downarrow\rangle$. Once the ODMR resonance is found by scanning the microwave frequency [Fig. 2.3(b)], we drive the qubit transition on reso-

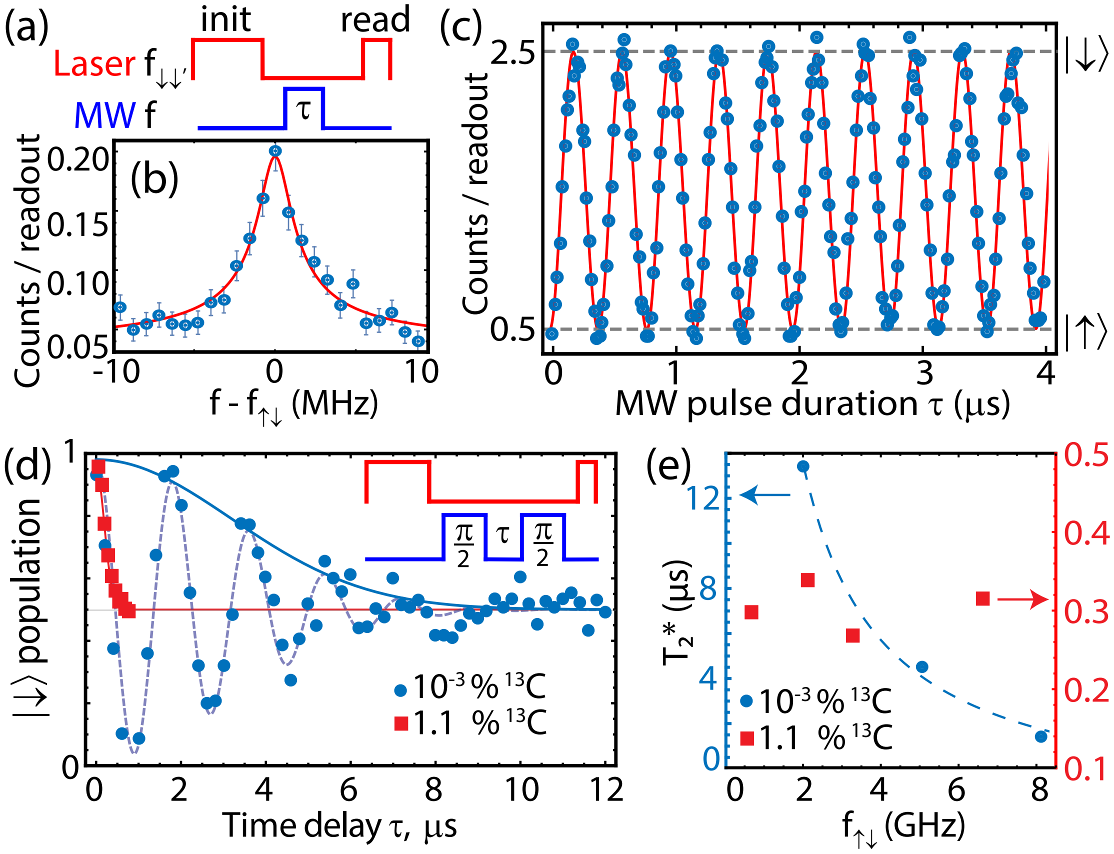

Figure 2.3: (a) Pulse sequence for ODMR and Rabi measurements. (b) Pulsed ODMR measurement for $\tau = 500\,\mathrm{s}$. Durations of the initialization and readout laser pulses are $15\,\mathrm{ms}$ and $2\,\mathrm{ms}$, respectively [appendix B]. (c) Resonant driving at frequency $f_{\uparrow\downarrow}$ results in Rabi oscillations between states $|\uparrow\rangle$ and $|\downarrow\rangle$. Data in (b) and (c) are from Sample-12. (d) Ramsey interference measurement of T_2^* for the two samples. MW pulses are detuned by $\sim 550\,\mathrm{kHz}$ from the $f_{\uparrow\downarrow}$ for the blue data. Duration of the initialization (readout) laser pulse is $15\,\mathrm{ms}$ $(2\,\mathrm{ms})$ for Sample-12 and $1.5\,\mathrm{ms}$ $(00.2\,\mathrm{ms})$ for Sample-13. (e) T_2^* as a function of qubit resonant frequency. Dashed blue line is a fit to $1/f_{\downarrow\uparrow}$ scaling [appendix B].

nance and observe Rabi oscillations [Fig. 2.3(c)]. Finally, we use Ramsey interference to measure the spin dephasing time T_2^* for both samples [Fig. 2.3(d)]. For Sample-12, which contains a low density of nuclear spins (blue circles), we measure a dephasing time in the range of $T_2^* = 1.5\,\mathrm{s}$ to $13\,\mathrm{s}$. For this sample, we find that T_2^* scales inversely with the qubit frequency $\mathrm{f}_{\uparrow\downarrow}$ as shown in Figure 2.3(e). The observed scaling $T_2^* \propto 1/\mathrm{f}_{\uparrow\downarrow}$ indicates that fluctuations of the electronic g-factor Δg likely limit the T_2^* via the relation $1/(T_2^*) \propto \Delta g \mu_\mathrm{B} B$ where μ_B is the Bohr magneton. Possible origins for Δg are discussed in appendix B. For Sample-13, which contains a natural abundance of nuclear spins (red squares), we measure $T_2^* \approx 300\,\mathrm{ns}$ independent from the magnetic field magnitude which is similar to typical values observed in NVs. These results demonstrate that the dephasing time T_2^* of SiVs in Sample-13 is primarily limited by the nuclear spin bath in the diamond host with a natural abundance of $^{13}\mathrm{C}$[95].

Dephasing due to slowly evolving fluctuations in the environment (e.g. nuclear spins) can be suppressed by using dynamical decoupling techniques[96,97]. We extend the spin coherence time T_2 by implementing Carr–Purcell (CP) sequences with $N = 1, 2, 4, 8, 16$, and 32 rephasing pulses[98] in Sample-12 [Fig. 2.4(a,b)]. Figure 2.4(c) shows that the coherence time increases approximately linearly with the number of rephasing pulses N. The longest observed coherence time is $T_2 = 13 \pm 1.7$ ms for $N = 32$. We also implement CP sequences for $N = 1, 2$, and 4 in Sample-13 and find similar coherence times T_2 as for Sample-12 [Fig. 2.4(c)]. We repeat the CP measurements at higher temperatures: at $400\,\mathrm{mK}$, the T_2 time measured by CP2 is identical to T_2 at 100 mK (red and orange data). At a temperature of 600 mK, the spin-echo (CP1) T_2 is dramatically reduced to 60 s. Spin-echo measurements with Sample-13 at a weak magnetic field of 0.2 kG show high-visibility oscillations of the electronic spin coherence [appendix B]. These dynamics are suppressed at stronger fields [appendix B] and are characteristic of coherent coupling to nearby ^{13}C nuclear spins[95].

Surprisingly, the observation in Figure 2.4 that the coherence time T_2 in both samples is identical for a given N indicates that the coherence time T_2 is not limited by the nuclear spin bath, but by another noise source. This observation is also supported by the approximately linear scaling ($T_2 \sim N$) of coherence with the number of π-pulses which deviates substantially from the expected $\sim N^{2/3}$ scaling for dipolar coupling to nuclear spins[99,100]. We also do not find a significant difference between T_2 measured at different magnetic fields [appendix B], suggesting that g-factor fluctuations are also not the limiting factor for these measurements.

While the origin of the noise source is at present not understood, the linear dependence of T_2 on N suggests that T_2 can potentially be further improved by using additional rephasing pulses. In the current measurements, errors due to imperfect π-pulses [appendix B] result in reduced state fidelities for pulse sequences with $N \geq 32$. Pulse errors can be reduced by using decoupling sequences with two-axis (XY) control[97]. The gate fidelities can also be improved using higher MW Rabi frequencies [appendix B] that can be obtained with low-loss superconducting coplanar waveguides[101].

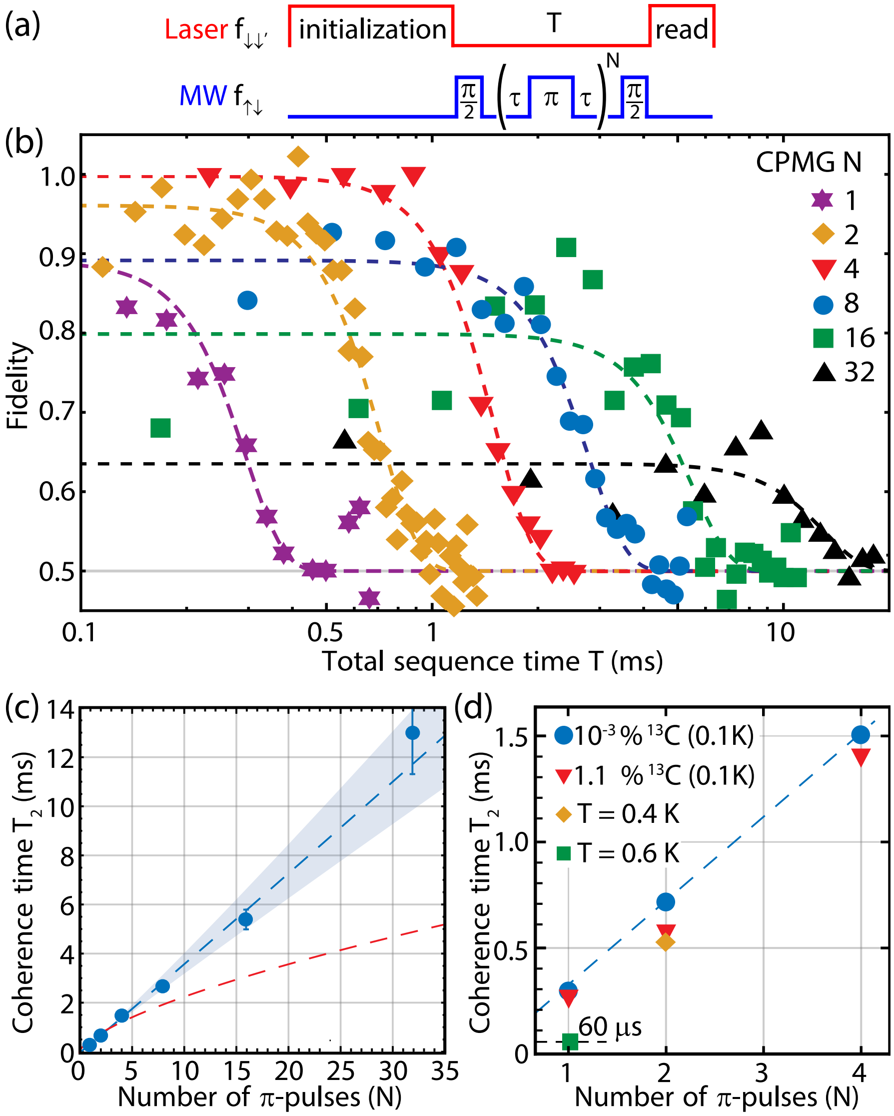

Figure 2.4: 13 ms spin coherence with dynamical decoupling. (a) CPMG sequence with N rephasing MW π-pulses. (b) Spin coherence for CP sequences with $N = 1$, 2, 4, 8, 16, and 32 pulses in Sample-12 in an aligned magnetic field $B \approx 1.6\,\mathrm{kG}$ at $100\,\mathrm{mK}$. The longest measured T_2 time is $13\,\mathrm{ms}$ for $N = 32$. State fidelity reduces with higher N due to π-pulse errors. Durations of the initialization and readout laser pulses are $\sim 100\,\mathrm{ms}$ and $\sim 15\,\mathrm{ms}$, correspondingly. Dashed lines are fits to exp$[-({}^{T}\!/\!{}_{T_2})^4]$ [appendix B]. (c) T_2 coherence vs. number of rephasing pulses N for Sample-12. Fitting to $T_2 \propto N^\beta$ gives $\beta = 1.02 \pm 0.05$ (blue dashed line), the shaded region represents a standard deviation of 0.05. For comparison, the red dashed line shows $N^{2/3}$ scaling. (d) T_2 coherence vs. number of rephasing pulses N for Sample-12 and Sample-13. Green and orange points are measured with Sample-13 at elevated temperatures.

2.4 Conclusion

These observations establish the SiV as a promising solid-state quantum emitter for the realization of quantum network nodes using integrated diamond nanophotonics[40]. Although understanding the noise bath and its effects on the SiV spin dynamics is an important area of future study, the demonstrated coherence time of 13 ms is already sufficient to maintain quantum states between quantum repeater nodes separated by 10^3 km[80]. The quantum memory lifetime could be further extended by implementing robust dynamical decoupling schemes[97] or using coherently coupled nuclear spins as longer-lived memories[102]. The SiV spin could also be strongly coupled to localized acoustic[103,104] modes by exploiting the large strain susceptibility of SiVs (PHz / strain)[103]. This offers new opportunities for realizing two-qubit gates[105,106,107] and interfacing superconducting quantum circuits with long-lived spin memories and optical photons[108].

3

An integrated nanophotonic quantum register based on silicon-vacancy spins in diamond

This chapter has been published as

"An integrated nanophotonic quantum register based on silicon-vacancy spins in diamond"

C. T. Nguyen, D. D. Sukachev, M. K. Bhaskar, B. Machielse, D. S. Levonian, E. N. Knall, P. Stroganov, C. Chia, M. J. Burek, R. Riedinger, H. Park, M. Lončar and M. D. Lukin Phys. Rev. B 100, 165428 (2019)

3.1 Introduction

Quantum networks have the potential to enable a plethora of new technologies including secure communication, enhanced metrology, and distributed quantum computing[13,14,17,18,109]. Such networks require nodes which perform quantum processing on a small register of interconnected qubits with long coherence times. Distant nodes are connected by efficiently interfacing qubits with optical photons that can be coupled into an optical fiber [Fig. 3.1(a)].

The prevailing strategy for engineering an efficient, coherent optical interface is that of cavity quantum electrodynamics (QED), which enhances the interactions between atomic quantum memories and photons[23,110,111,112,113]. Nanophotonic cavity QED systems are particularly appealing, as the tight confinement of light inside optical nanostructures enables strong, high-bandwidth qubit-photon interactions[40,114,115]. In practice, nanophotonic devices also have a number of technological advantages over

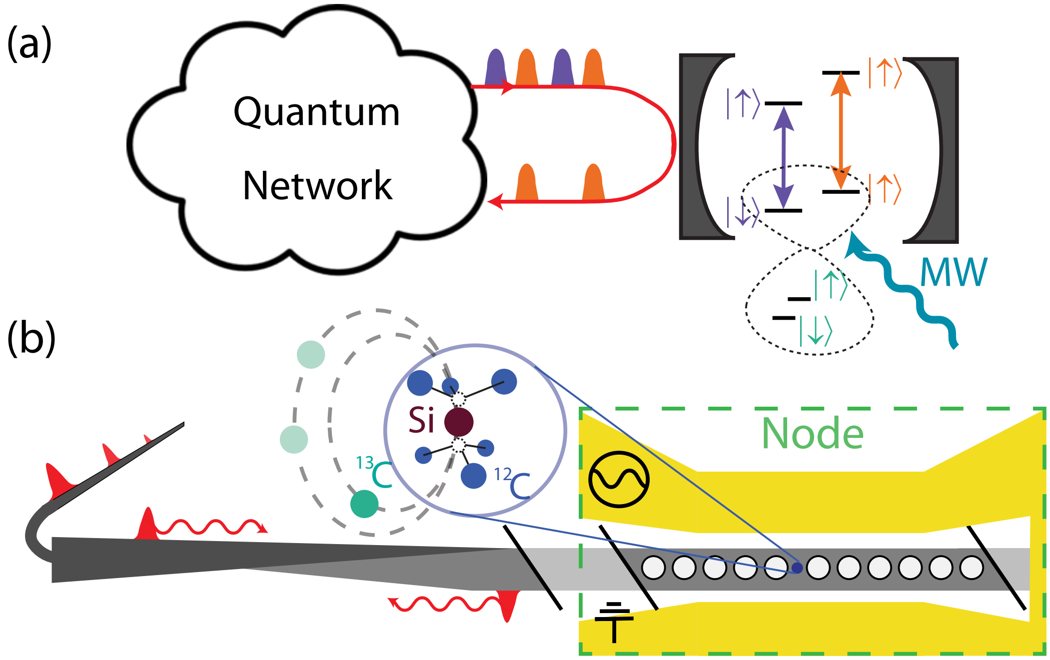

Figure 3.1: (a) Schematic of a quantum network. Nodes consisting of several qubits are coupled together via an optical interface. (b) A quantum network node based on the SiV. SiV centers and ancilla ^{13}C are incorporated into a nanophotonic device and addressed with a coupled fiber and microwave coplanar waveguide.

macroscopic optical cavities, as they can be fabricated en-masse and interfaced with on-chip electronics and photonics, making them suitable for scaling up to large-scale networks[23,116]. While strong interactions between single qubits and optical photons have been demonstrated in a number of cavity QED platforms[23,24,113,117,118,119], no single realization currently meets all of the requirements of a quantum network node. Simultaneously achieving high-fidelity, coherent control of multiple long-lived qubits inside of a photonic structure is a major outstanding challenge.

Recent work has established the silicon-vacancy color-center in diamond (SiV) as a promising candidate for quantum networking applications[41,45,120,121,122]. The SiV is an optically active point defect in the diamond lattice[37,123]. Its D_{3d} inversion symmetry results in a vanishing permanent electric dipole moment of the ground and excited states, rendering the transition insensitive to electric field noise typically present in nanostructures[39]. Recent work has independently shown that SiV centers in nanostructures display strong interactions with single photons[41] and that SiV centers at temperatures below 100 mK (achievable in dilution refrigerators) exhibit long coherence times[44], [Ch. 2]. While these results indicate the promising potential of the SiV center for future quantum network nodes, significant technical challenges must be overcome in order to combine these ingredients.

In this chapter, we outline the practical considerations and approaches needed to build a quantum network node with SiV centers in nanophotonic diamond cavities coupled to ancillary nuclear spins [Fig. 3.1(b)] [Ch. 4]. Section 3.2 describes recent improvements to the fabrication techniques used to create and incorporate SiV centers into high-quality factor, critically-coupled nanophotonic cavities with an efficient fiber-optical interface. Section 3.3 describes the millikelvin experimental apparatus and several common experimental protocols. Section 3.4 describes the SiV level structure and electronic transitions, illustrating the interplay of strain and magnetic field in enabling both coherent control of– and a photonic interface for– SiV spins. Sections 3.5, 3.6 and 3.7 outline experimental implementations of optical and microwave control of SiV centers, and use this control to create electron-photon Bell states with high fidelity in section 3.8. Section 3.9 introduces techniques for coupling to additional qubits consisting of naturally occuring ^{13}C in diamond. We describe our method for initializing and reading out these nuclear spins via the SiV, coherent control of ^{13}C with microwave and radio-frequency driving, probe the coherence of these nuclei, and finally entangle the SiV with a nearby ^{13}C and demonstrate electron-nuclear Bell states.

3.2 Nanophotonic device fabrication

3.2.1 Device design

The devices used in these experiments integrate nanophotonic cavities, implanted SiV centers, and microwave coplanar waveguides onto a single diamond chip. Here

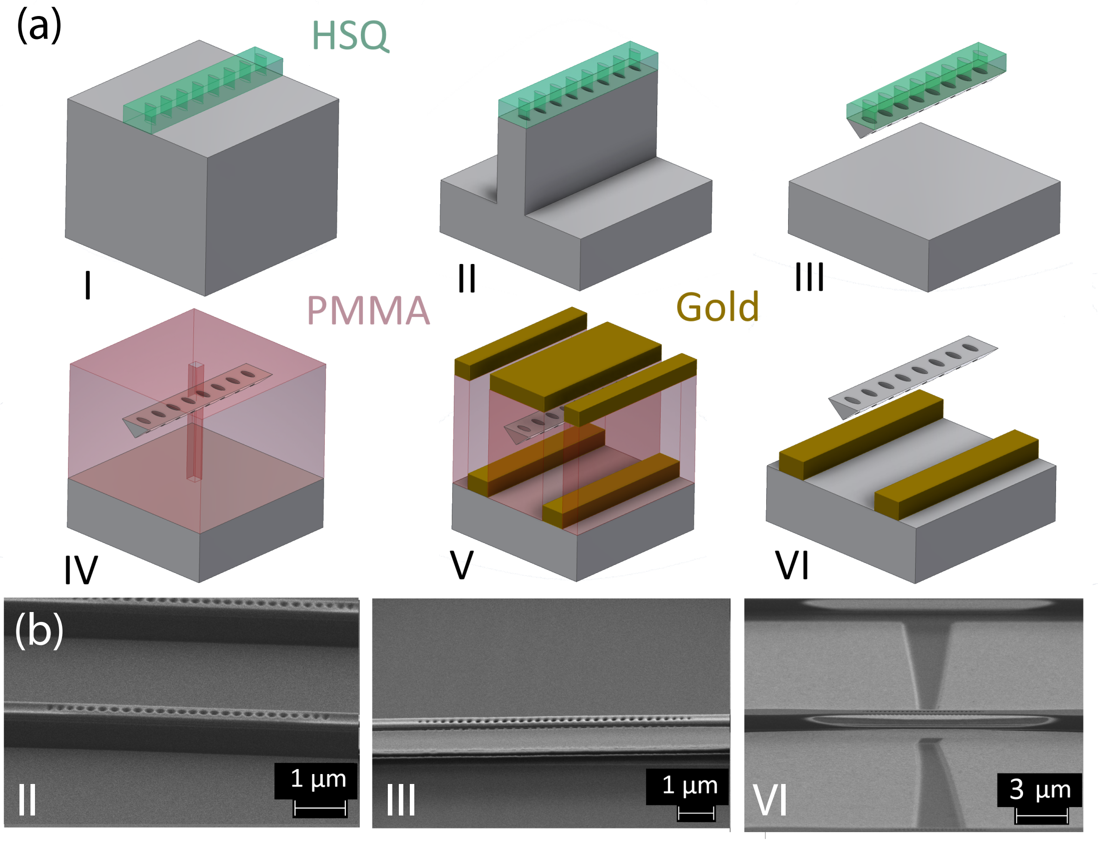

Figure 3.2: (a) Schematic of the nanofabricataion process used to produce devices. I: Titanium-HSQ mask is patterned using EBL. II: Pattern is transferred onto diamond using top down O_2 RIE. III: Angled IBE is used to separate structures from substrate. IV: Devices are covered in PMMA and implantation aperatures are formed using EBL. Device are then cleaned, implanted, and annealed. V: PMMA is used in a litoff procedure to pattern gold microwave striplines. VI: Final devices are cleaned and prepared for experiment. (b) Scanning electron micrographs corresponding to steps II, III, and VI in the fabricaton procedure.

we present the fabrication process used to realize such devices.

Typically, high-quality photonic crystal resonators are fabricated from 2-D membranes, which tightly confine light due to total internal reflection off of material boundaries. Difficulties in growing high-purity, single-crystal diamond films on non-diamond substrates are one of the key challenges to fabricating such resonators in diamond[124]. As a result, nanophotonic diamond structures must be etched out of bulk diamond, which requires non-traditional etching techniques[125,126]. In particular, two methods have emerged for creating freestanding diamond nanostructures: Isotropic undercutting[126,127] and angled ion-beam etching (IBE)[128]. In this work, we use the latter technique, resulting in freestanding, triangular-cross-section waveguides.

Preliminary design of the nanophotonic structures are described in appendix C.1, and are optimized to maximize atom-photon interaction while maintaining high waveguide coupling. To take advantage of the scalable nature of nanofabrication, these optimized devices are patterned in sets of roughly 100 with slightly modified fabrication parameters. The overall scale of all photonic crystal cavity parameters are varied between different devices on the same diamond chip to compensate for fabrication errors (which lead to unexpected variations in the resonator frequency and quality-factor). Due to these errors, roughly one in six cavities are suitable for SiV experiments. Fortunately, hundreds of devices are made in a single fabrication run, ensuring that every run yields many usable devices.

The diamond waveguide region (as opposed to the photonic crystal cavity region

[Appendix. C.1]) has two distinguishing features. First, thin support structures are placed periodically along the waveguide and are used to suspend the structures above the substrate. These supports are portions of the waveguide which are adiabatically tapered to be $\sim$ 30% wider than the rest of the waveguide, and take longer to etch away during the angled etch process. By terminating the etch after normal waveguide regions are fully etched through, these wide sections become $\sim$ 10 nm thick supports which tether the waveguide structures to the substrate while minimizing scattered loss from guided modes. Second, one end of the waveguide structure is adiabatically tapered into free-space[129]. These tapers are formed by a linear taper of the waveguide down to less than 50 nm wide over a 10 m length. This tapered region can be coupled to a similarly tapered optical fiber, allowing structures to efficiently interface with a fiber network [Sec. 3.3]. This tapered end of the waveguide is the most fragile portion of the structure, and can break after repeated fiber coupling attempts. This is often what limits the total measurement lifetime of a device.

The number of devices (and thus the relative yield of the fabrication process) is limited by the maximum packing density on the diamond chip. This is primarily limited by the need to accommodate 10 m wide microwave coplanar waveguides (CPWs) between devices, which are patterned directly onto the diamond surface to efficiently control SiV spins using microwaves. Simulations (Sonnet Inc) of prospective design geometries ensure that the CPW is impedance matched with our 50 feed lines, which minimizes scattered power from the waveguides. Tapers in the CPW near the center of the cavity regions concentrate current and increase the amplitude of the microwave field near the SiVs, and CPWs are terminated with a short in order to ensure a magnetic field maximum along the device.

3.2.2 Device fabrication

Fabrication of the diamond structures proceeds as described in ref.[129] with the notable modification that the angled etch is conducted not with a Faraday cage loaded inside a reactive ion etching chamber, but instead with an IBE. The Faraday cage technique[125,130] offered the benefit of simplicity and accessibility—requiring only that the reactive ion etching chamber in question was large enough to accommodate the cage structure—but suffered from large fluctuations in etch rate across the surface of the sample, as well as between different fabrication runs, due to imperfections in the Faraday cage mesh. These irregularities could be partially compensated for by repeatedly repositioning and rotating the cage with respect to sample during the etch, but this process proved to be laborious and imprecise. Instead, IBE offers collimated beams of ions several cm in diameter, leading to almost uniform etch rates across the several mm diamond chip. This technique allowed for consistent fabrication of cavities with $Q > 10^4$, $V < 0.6[\lambda/(n = 2.4)]^3$, and resonances within $\sim 10\,\text{nm}$ of SiV optical frequencies.

Once the diamond cavities are fabricated [Fig. 3.2(a I-III)], SiV centers must be incorporated. To ensure the best possible atom-photon interaction rate [Sec. 3.5], SiVs should be positioned at the cavity mode maximum. Ideally, this requires implantation accuracy of better than 50 nm in all 3 dimensions due to the small mode volume ($\sim 0.5[\lambda/(n = 2.4)]^3$) of the cavities used. In the past, implantation of silicon ions (which form SiV centers following a high-temperature anneal) was done using focused ion-beam implantation, but this technique required specialized tools and lacked the accuracy necessary for maximally efficient mode coupling[40]. Instead, we adapt the standard masked implantation technique and use commercial foundaries for ion implantation.

For the implantation process, we repeatedly spin and bake MMA EL11 and PMMA C4 (Microchem) to cover the nanophotonic cavities completely with polymer resist. We then spin-coat a conductive surface layer of Espacer (Showa Denko). An E-beam lithography (EBL) tool then aligns with large markers underneath the polymer layer, allowing it to expose an area surrounding smaller, high-resolution alignment markers on the diamond. The exposed regions are developed in a 1:3 mixture of MIBK:IPA. Espacer is again spin-coated, and a second EBL write can be done, aligned to the high-resolution markers. Based on these alignment markers, holes of less than 65 nm diameter (limited by the resolution of PMMA resist) are patterned onto the center of the photonic crystal cavity which, after subsequent development, act as narrow apertures to the diamond surface [Fig. 3.2(a IV)]. The rest of the diamond surface is still covered in sufficiently thick PMMA to prevent ions from reaching masked portions of the device. Diamonds are then sent to a commercial foundry (Innovion) where they are implanted with silicon ions at the appropriate energy and dose [Fig. 3.2 (b)]. Annealing in a UHV vacuum furnace (Kurt-Lesker) at ∼1400 K converts these implanted ions into SiV centers[39,131].

CPWs are fabricated using a liftoff process similar to that used to create masked implantation windows. The most notable difference is an additional oxygen plasma descum after development to remove PMMA residue from the surface. Following development, a 10 nm titanium film serves as an adhesion layer for a 250 nm thick gold CPW [Fig. 3.2 (a V)]. Liftoff is performed in heated Remover PG (Microchem) [Fig. 3.2 (a VI)]. The metal thicknesses used here are chosen to improve adhesion of the gold, as well as prevent absorption of cavity photons by the metallic CPW. We observe that the cavity quality factor significantly degrades with gold films $>$ 300 nm. Due to ohmic heating, which can degrade the coherence properties of SiV spins [Sec. 3.6], the length of the CPW is constrained to address a maximum of roughly 6 devices.

Future improvements in diamond device performance will be predicated on improvements of the fabrication technology. Device quality factors are currently limited by deviations in device cross section caused by imperfect selectivity of the HSQ hard mask to oxygen etching. Replacing this mask with a sufficiently smooth metal mask could result in improved etch selectivity and device performance. Isotropic undercut etching could also lead to improved control over device cross sections and facilitate more sophisticated device geometries[127,132] at the cost of reduced control over isotropically etched surface roughness. Various techniques exist for the formation of smaller implantation apertures[133,134], but these techniques are difficult to use in conjunction with implantation into completed nanophotonic devices. Finally, the use of superconducting striplines could reduce heating, which would enable the CPW to potentially address all devices on the diamond chip and allow for faster driving of SiV spin and nuclear transitions [Sec. 3.6, 3.9].

3.3 Experimental Setup

Experiments are performed in a home-built photonic-probe setup inside of a dilution refrigerator (DR, BlueFors BF-LD250) [Fig. 3.3(a)]. The diamond substrate is mounted to a gold-plated copper sample holder via indium soldering below the mixing chamber in the bore of a (6,1,1) T superconducting vector magnet (American Magnetics Inc.) anchored to the 4 K stage. A thermal link between the device and the mixing chamber plate is provided by gold-plated copper bars, as well as oxygen-free copper braids (Copper Braid Products), ensuring maximal thermal conductivity between the mixing chamber plate and the sample, which reaches a base temperature of roughly 60 mK. We address single nanophotonic devices via a tapered optical fiber, which can be coupled *in-situ* with collection efficiencies exceeding 90%[129]. The tapered fiber is mounted to a 3-axis piezo stepper (ANPx101, ANPz101), and imaged in free-space by

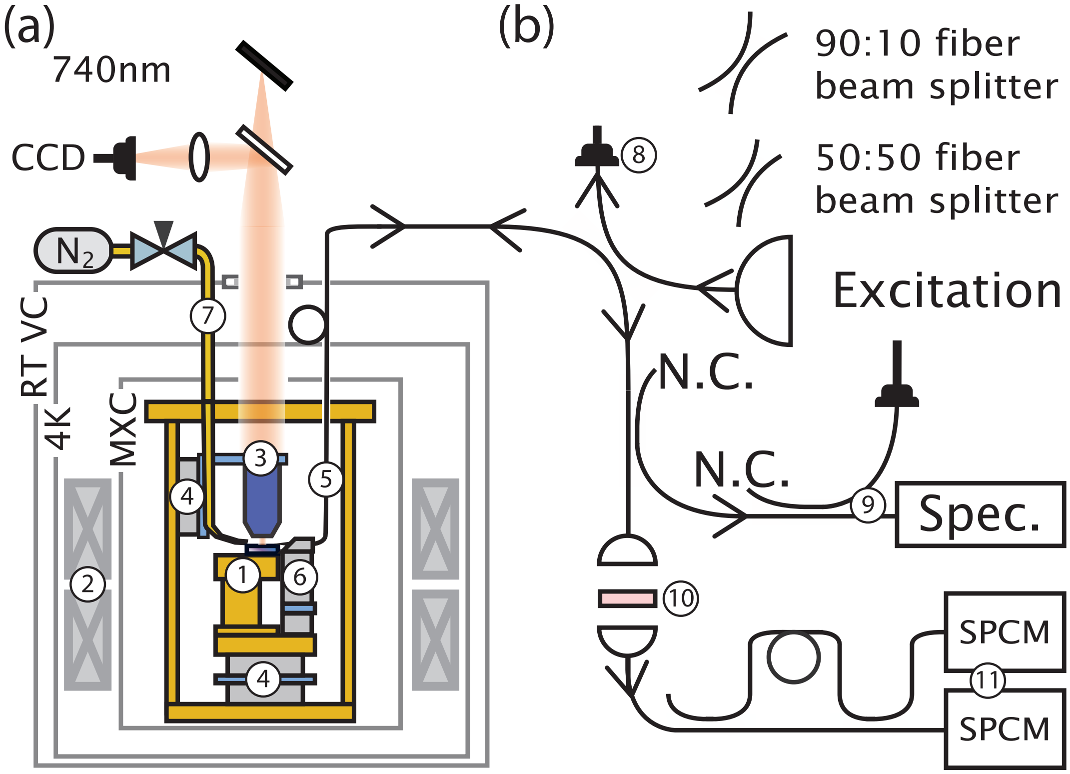

Figure 3.3: (a) Experiment schematic. Devices ① are mounted in the bore of a SC magnet ② inside of a dilution refrigerator, and imaged with wide-field imaging ③ and piezo steppers ④. Devices are addressed with a tapered optical fiber ⑤ positioned using a second set of piezo steppers ⑥. Cavities are tuned using a nitrogen ⑦. (b) Fiber network used to probe devices. Excitation light is monitored ⑧ and sent to the device. Collected light is monitored ⑨ and filtered ⑩ then sent to one or several SPCMs ⑪. N.C. indicates no connection.

an $8f$ wide-field scanning confocal microscope which focuses onto a cryo-compatible objective (Attocube LT-APO-VISIR). This setup allows for coupling to several cavities during a single cooldown.

Once coupled, the cavity resonance is red-shifted via nitrogen gas condensation[41]. A copper tube is weakly thermalized with the 4 K plate of the DR and can be heated above 80 K in order to flow N_2 gas onto the devices. This gas condenses onto the photonic crystal, modifying its refractive index and red-shifting the cavity resonance. When the copper tube is not heated, it thermalizes to 4 K, reducing the blackbody load on the sample and preventing undesired gas from leaking into the vacuum chamber.

After red-tuning all devices in this way, each cavity can be individually blue-tuned by illuminating the device with a ∼100 W broadband laser via the tapered fiber, locally heating the device and evaporating nitrogen. This laser-tuning can be performed very slowly to set the cavity resonance with a few GHz. The cavity tuning range exceeds 10 nm without significantly degrading the cavity quality factor, and is remarkably stable inside the DR, with no observable drift over several months of measurements.

In previous work[41], SiVs were probed in transmission via the free-space confocal microscope focused onto a notch opposing the tapered fiber. Mechanical vibrations arising from the DR pulse tube (∼1 m pointing error at the sample position) result in significant fluctuations in power and polarization of incoupled light. In this work, we demonstrate a fully integrated solution by utilizing the same tapered fiber to both probe the device and collect reflected photons. This approach stabilizes the excitation path and improves the efficiency of the atom-photon interface, allowing for deterministic interactions with single itinerant photons. High-contrast reflection measurements are enabled by the high-cooperativity, critically-coupled atom-cavity system. Resonant light is sent via the fiber network [Fig. 3.3(b)] and reflected off of the target device. We pick off a small fraction ($\sim 10\%$) of this signal and use it to monitor the wide-band reflection spectrum on a spectrometer (Horiba iHR-550) as well as calibrate the coupling efficiency to the nanocavity. The remaining reflection is then routed either directly to a single-photon counting module (SPCM, Excelitas SPCM-NIR), or into a time-delay interferometer for use in spin-photon experiments [Sec. 3.8]. Due to this high-efficiency fiber-coupled network, we observe overall collection efficiencies of $\sim 40\%$, limited by the quantum efficiency of our APDs.

3.4 Optimal strain regimes for SiV spin-photon experiments

Similar to other solid state emitters[135,136], the SiV is sensitive to local inhomogeneity in the host crystal. In the case of the SiV, which has D_{3d} symmetry, the dominant perturbation is crystal strain. In this section, we describe the effects of strain on the

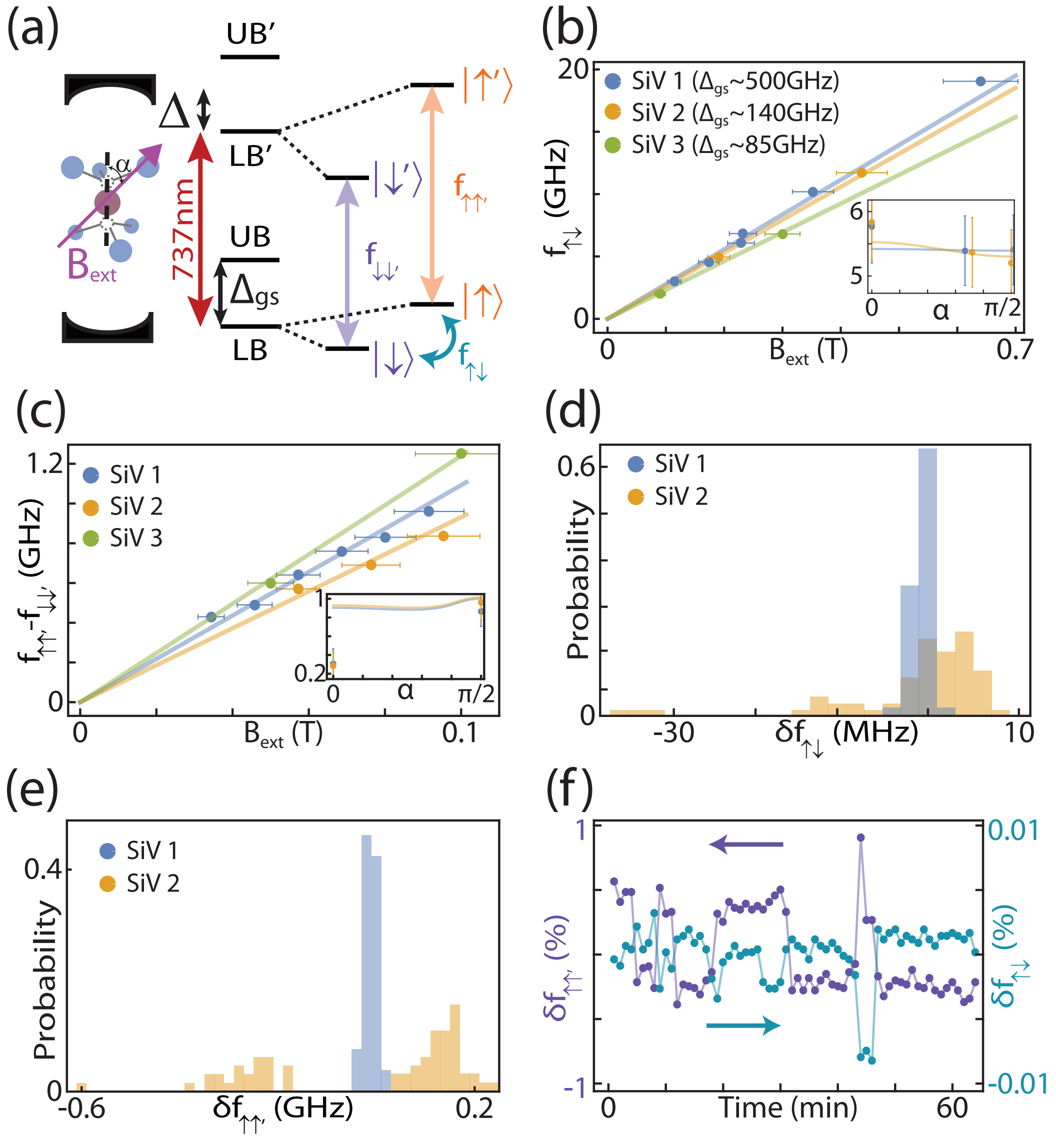

Figure 3.4: (a) SiV level diagram. Optical transitions $f_{\uparrow\uparrow'}, f_{\downarrow\downarrow'}$ $\sim 737\,\mathrm{nm}$ are coupled to a nanophotonic cavity with mean detuning Δ. Microwaves at frequency $f_{\uparrow\downarrow}$ drive rotations in the lower branch (LB). (b) Qubit frequency $f_{\uparrow\downarrow}$ for differently strained emitters. Modeled splitting for ground state g-factors $\mathrm{g_{gs1}} = 1.99, \mathrm{g_{gs2}} = 1.89, \mathrm{g_{gs3}} = 1.65$ (solid lines) based on independent measurements of Δ_{gs}. (inset) Angle dependence of $f_{\uparrow\downarrow}$ at fixed field $B_{\mathrm{ext}} = 0.19\,\mathrm{T}$. Solid lines are predictions using the same model parameters. (c) Optical splitting $f_{\uparrow\uparrow'} - f_{\downarrow\downarrow'}$. Fits extract excited state g-factors $\mathrm{g_{es1}} = 1.97, \mathrm{g_{es2}} = 1.83, \mathrm{g_{es3}} = 1.62$ (solid lines). (inset) Angle dependence of $f_{\uparrow\uparrow'} - f_{\downarrow\downarrow'}$ at fixed field $B_{\mathrm{ext}} = 0.1\,\mathrm{T}$. (d) Histogram of MW transition frequency for two different emitters. (e) Histogram of Optical transition frequency for two different emitters. (f) Simultaneous measurement of $f_{\uparrow\downarrow}$ and $f_{\uparrow\uparrow'}$ reveals correlations between optical and microwave spectral diffusion for emitter 2.

SiV spin and optical properties, and how they can enable efficient microwave and optical control of SiV centers inside nanostructures.

3.4.1 SiV Hamiltonian in the presence of strain and spin-orbit coupling

The SiV electronic structure is comprised of spin-orbit eigenstates split by spin-orbit interactions. Optical transitions connect the ground state manifold (LB, UB) and excited state manifold (LB', UB') [Fig. 3.4(a)]. In a DR, phonon absorption $LB \rightarrow UB$ (and $LB' \rightarrow UB'$) is supressed, resulting in thermal polarization into LB.

We consider the ground state SiV Hamiltonian with spin-orbit and strain interactions, in the combined orbital and spin basis $\{|e_y \uparrow\rangle, |e_y \downarrow\rangle, |e_x \uparrow\rangle, |e_x \downarrow\rangle\}$[37,121]

$$\mathcal{H}_{SiV} = \mathcal{H}_{SO} + \mathcal{H}_{\text{strain}} \tag{3.1}$$

$$= \begin{pmatrix} \alpha-\beta & 0 & \gamma-i\lambda & 0 \\ 0 & \alpha-\beta & 0 & \gamma+i\lambda \\ \gamma+i\lambda & 0 & \alpha+\beta & 0 \\ 0 & \gamma-i\lambda & 0 & \alpha+\beta \end{pmatrix} \tag{3.2}$$

where α corresponds to axial strain, β and γ correspond to transverse strain, and λ is the strength of spin-orbit interaction. Diagonalizing this reveals the orbital character of the lower branch:

$$LB \propto \begin{cases} |e_x \uparrow\rangle - \frac{1+\sqrt{1+(\gamma/\beta)^2+(\lambda/\beta)^2}}{\gamma/\beta - i\lambda/\beta}|e_y \uparrow\rangle \\ \\ |e_x \downarrow\rangle - \frac{1-\sqrt{1+(\gamma/\beta)^2+(\lambda/\beta)^2}}{\gamma/\beta - i\lambda/\beta}|e_y \downarrow\rangle \end{cases} \tag{3.3}$$

We investigate these electronic levels in the context of the SiV as a spin-photon interface.

3.4.2 Effects of strain on the SiV qubit states

In the limit of zero crystal strain, the orbital factors simplify to the canonical form[37]

$$LB = \begin{cases} |e_+ \downarrow\rangle \\ \\ |e_- \uparrow\rangle \end{cases} \tag{3.4}$$

In this regime, the spin-qubit has orthogonal electronic orbital and spin components. As result, one would need to simultaneously drive an orbital and spin flip to manipulate the qubit, which is forbidden for direct microwave driving alone. Thus, in the low strain regime, two-photon optical transitions between the qubit states in a misaligned external field, already demonstrated at millikelvin temperatures in[120], are likely necessary to realize a SiV spin qubit.

In the high strain limit ($\sqrt{\beta^2+\gamma^2} \gg \lambda$), these orbitals become

$$LB = \begin{cases} (\cos(\theta/2)|e_x\rangle - \sin(\theta/2)|e_y\rangle) \otimes |\downarrow\rangle \\ \\ (\cos(\theta/2)|e_x\rangle - \sin(\theta/2)|e_y\rangle) \otimes |\uparrow\rangle \end{cases} \tag{3.5}$$

where $\tan(\theta) = \frac{\beta}{\gamma}$. In this regime, the ground state orbital components are identical, and the qubit states can be described by the electronic spin degree of freedom only. As such, the magnetic dipole transition between the qubit states is now allowed and can be efficiently driven with microwaves.

In addition to determining the efficiency of qubit transitions, the spin-orbit nature of the SiV qubit states also determines its susceptibility to external fields. In an externally applied magnetic field, LB splits due to magnetic moments associated with both spin– and orbital– angular momenta. This splitting is parameterized by an effective g-tensor which, for a fixed angle between the external field and the SiV symmetry axis, can be simplified to an effective g-factor: $\mu\,\mathrm{g}\,B_{\mathrm{ext}}/h = f_{\uparrow\downarrow}$. In the limit of large strain, the orbital component of the two LB wavefunctions converge, and g trends towards that of a free electron (g $=$ 2). As a result, the qubit states behave akin to a free-electron in the high strain regime, and there is no dependence of g on external field angle or small perturbations in crystal strain.

While it is difficult to probe β or γ directly, they relate to the energy difference between UB and LB via $\Delta_{\mathrm{gs}} = 2\sqrt{\beta_{\mathrm{gs}}^2+\gamma_{\mathrm{gs}}^2+\lambda_{\mathrm{gs}}^2}$ [Fig. 3.4(a)]. From this, we extract

$\sqrt{\beta^2 + \gamma^2}$, given the known value of λ_{gs} =46 GHz[37,42,123]. Numerically diagonalizing the SiV Hamiltonian using the extracted values for β and γ closely matches the measured ground state splitting, both as a function of applied field magnitude and angle [Fig. 3.4(b)].

3.4.3 Effects of strain on the SiV spin-photon interface

Strain also plays a crucial role in determining the optical interface to the SiV spin qubit. The treatment shown above can be repeated for the excited states, with the caveat that the parameters β, γ, and λ are different in the excited state manifold as compared to the ground state manifold[121]. These differences give rise to a different g-factor in the excited state (g_{es}). If the strain is much larger than both λ_{gs} =46 GHz and λ_{es} =255 GHz, then $\mathrm{g}_{\mathrm{gs}} \approx \mathrm{g}_{\mathrm{es}} \approx 2$. In this case, the two spin-cycling transition frequencies $f_{\uparrow\uparrow'}$ and $f_{\downarrow\downarrow'}$ are identical, and the only spin-selective optical transitions are the dipole-forbidden spin-flipping transitions $f_{\uparrow\downarrow'}$ and $f_{\downarrow\uparrow'}$.

Under more moderate strain, the difference $\delta\mathrm{g} = |\mathrm{g}_{\mathrm{es}} - \mathrm{g}_{\mathrm{gs}}|$ splits the degenerate optical transitions $f_{\uparrow\uparrow'}$ and $f_{\downarrow\downarrow'}$, making them spin-selective as well. Due to differences in the anisotropic g-tensor in the ground and excited states, $\delta\mathrm{g}$ depends on the orientation of the magnetic field as well, and is minimized in the case of a $\langle 111 \rangle$-aligned field [Fig 3.4(c), inset]. In such an external field aligned with the SiV symmetry axis, optical transitions become highly spin-conserving [Ch. 2], allowing many photons to scatter without altering the SiV spin state. This high cyclicity enables high-fidelity single-shot readout of the spin state [Ch. 4], even without high collection efficiencies [Ch. 2]. This makes working with the spin-cycling transitions highly desirable, at the expense of a reduced ability to resolve spin-selective transitions for a given field magnitude. The need to resolve individual transitions suggests an optimal strain regime where $\sqrt{\beta_{\mathrm{gs}}^2 + \gamma_{\mathrm{gs}}^2} \gg \lambda_{\mathrm{gs}}$, where MW driving is efficient, while $\sqrt{\beta_{\mathrm{es}}^2 + \gamma_{\mathrm{es}}^2} \lesssim \lambda_{\mathrm{es}}$, where one can independently address $f_{\uparrow\uparrow'}$ and $f_{\downarrow\downarrow'}$ [Fig. 3.4(c)].

3.4.4 Effects of strain on SiV stability

Despite the SiV's symmetry-protected optical transitions, spectral diffusion of the SiV has been observed in many experiments[38,39] (but still much smaller compared to emitters without inversion symmetry, for example, nitrogen-vacancy centers[86,137]). While the exact nature of this diffusion has not been studied in depth, it is often attributed to the second-order Stark effect or strain fluctuations, both of which affect the energies of SiV orbital wavefunctions. In this chapter, we also observe significant fluctuations of the spin qubit frequency.

As can be seen in reference[121], for an appropriately low static strain value, fluctuating strain can give rise to fluctuations in the g-tensor of the ground state, causing spectral diffusion of the qubit frequency $f_{\uparrow\downarrow}$ [Fig. 3.4(d)]. Since g_{gs} asymptotically approaches 2 as the static strain increases[121], the qubit susceptibility to this fluctuating strain is reduced in the case of highly strained SiV centers, resulting in a more stable qubit.

While spectral diffusion of the optical transition should not saturate in the same way as diffusion of the microwave transition, we observe qualitatively different spectral diffusion properties for different emitters [Fig. 3.4(e) and Fig. C.2]. SiV 1 ($\Delta_{\mathrm{gs}} = 500\,\mathrm{GHz}$) displays slow drift of the optical line which is stable to $<100\,\mathrm{MHz}$ over many minutes [Appendix. C.3]. We do not observe significant fluctuations ($> 500\,\mathrm{kHz}$) of the microwave transition for this SiV. On the other hand, SiV 2 ($\Delta_{\mathrm{gs}} = 140\,\mathrm{GHz}$) drifts over a wider range, and also exhibits abrupt jumps between several discrete frequencies [Appendix. C.3].

We simultaneously record the optical transition and qubit frequency for SiV 2 and observe correlations between the two frequencies [Fig. 3.4(f)], indicating that they could arise from the same environmental perturbation. In Appendix C.2, we calculate the qubit and optical transition frequencies using the strain Hamiltonian (eq. 3.2) and find that both correlations and absolute amplitudes of spectral diffusion can simultaneously be explained by strain fluctuations on the order of 1% ($\sim 10^{-7}$ strain) [Appendix C.2].

In this work we rely on static strain, likely resulting from damage induced by ion implantation and nanofabrication, and select for spectrally stable SiVs with appropriate strain profiles. This is characterized by first measuring Δ_{gs} in zero magnetic field at $4\,\mathrm{K}$ by exciting the optical transition $LB \rightarrow LB'$ and measuring emission from the

$LB' \to UB$ on a spectrometer. We use this to screen for SiVs with $\Delta_{gs} > 100\,\text{GHz}$ to ensure efficient MW driving of the spin qubit. We further apply a static external magnetic field and measure spectral stability properties as well as $f_{\uparrow\uparrow'} - f_{\downarrow\downarrow'}$ to guarantee a good spin-photon interface. We measured ~ 10 candidate emitters, and found 4 which satisfy all of the necessary criteria for spin-photon experiments.

3.5 Regimes of cavity-QED for SiV spin-photon interfaces

Efficient spin-photon interactions are enabled by incorporating SiV centers into nanophotonic cavities. In this section, we describe SiV-cavity measurements in several regimes of cavity QED, and comment on their viability for spin-photon experiments.

3.5.1 Spectroscopy of cavity-coupled SiVs

We measure the spectrum of the atom-cavity system at different atom-cavity detunings in order to characterize the device and extract key cavity QED parameters [Fig. 3.5(a)]. The reflection spectrum of a two-level system coupled to a cavity is modeled by solving the frequency response of the standard Jaynes-Cummings Hamiltonian

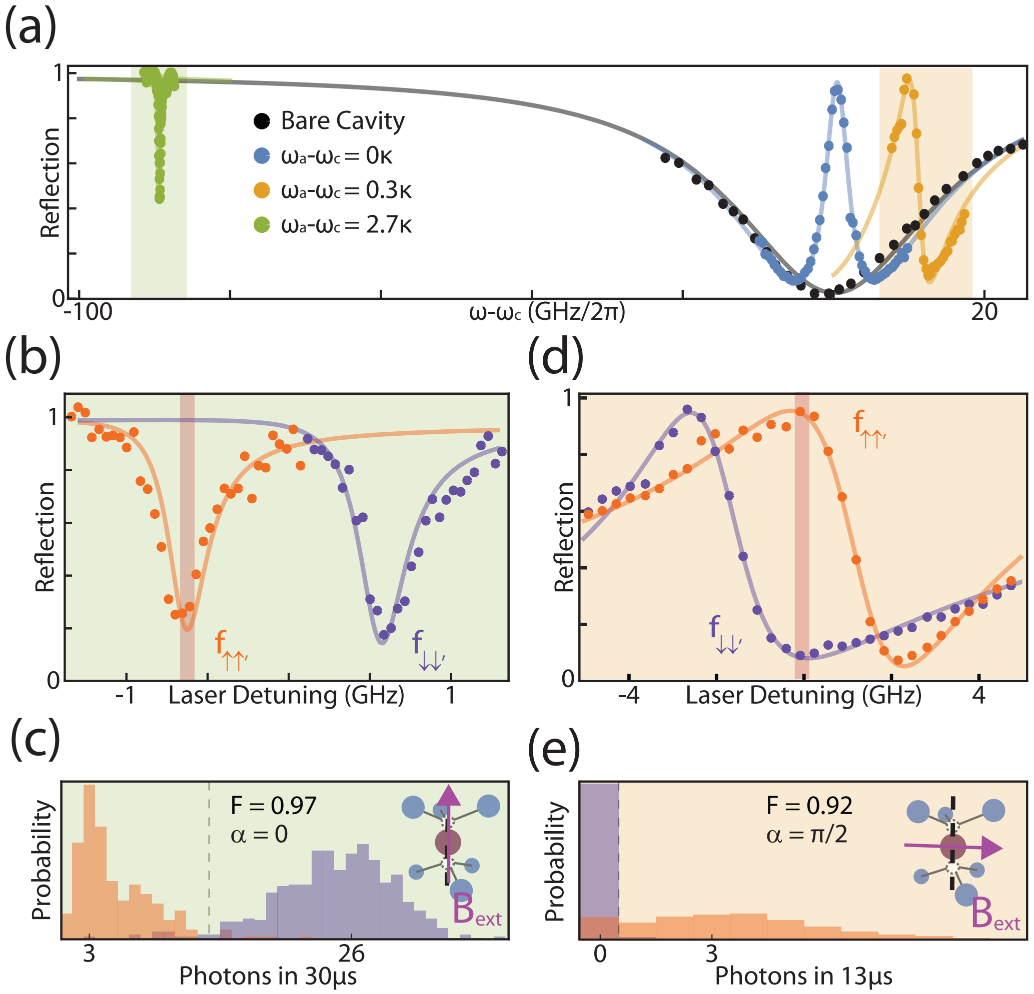

Figure 3.5: (a) SiV-cavity reflection spectrum at several detunings. The bare cavity spectrum (black) is modulated by the presence of the SiV. When the atom cavity detuing is small (Blue, orange), high-contrast, broad features are the result of Purcell enhanced SiV transitions. Far from the cavity resonance (green), interaction results in narrow SiV-assisted transmission channels. (b) Spin-dependent reflection for large SiV-cavity detuning $\Delta \approx -3\kappa$, $B_{\text{ext}} = 0.35\,\mathrm{T}$. In this regime, SiV spin states can be individually addressed. (c) Probing either transmission dip results in high-fidelity single-shot readout in an aligned field ($F = 0.97$, threshold on detecting 13 photons). (d) Spin-dependent reflection near resonance $\Delta \approx 0.5\kappa$, $B_{\text{ext}} = 0.19\,\mathrm{T}$. Dispersive lineshapes allow for distinguishable reflection spectra from both SiV spin states. (e) A probe at the frequency of maximum contrast (f_Q) can determine the spin state in a single shot in a misaligned field($F = 0.92$, threshold on detecting > 1 photon).

using input-output formalism for a cavity near critical coupling[111]:

$$\mathcal{R}(\omega) = \left| 1 - \frac{2\kappa_l}{i(\omega - \omega_c) + \kappa_{\text{tot}} + g^2/(i(\omega - \omega_a) + \gamma)} \right|^2, \tag{3.6}$$

where κ_l is the decay rate from the incoupling mirror, κ_{tot} is the cavity linewidth, $\omega_c(\omega_a)$ is the cavity (atom) resonance frequency, g is the single-photon Rabi frequency, and γ is the bare atomic linewidth. Interactions between the SiV optical transition and the nanophotonic cavity result in two main effects. First, the SiV center can modulate the reflection spectrum of the bare cavity, as seen in the colored curves of figure 3.5(a). Second, the coupling to the cavity can broaden the linewidth of the SiV based on the Purcell effect:

$$\Gamma \approx \gamma + 4g^2/\kappa \frac{1}{1 + 4(\omega_c - \omega_a)^2/\kappa^2}$$

When the cavity is far detuned from the atomic transition $|\omega_c - \omega_a| \equiv \Delta > \kappa$ [Fig. 3.5(a), green], Purcell enhancement is negligible and the cavity and atomic linewidths $\kappa, \gamma = 2\pi \times \{33, 0.1\}$ GHz are estimated. When the cavity is on resonance with the atom ($\Delta = 0$), we fit (3.6) using previously estimated values of κ and γ to extract $g = 2\pi \times 5.6$ GHz. Together, these measurements allow us to determine the atom-cavity cooperativity $C = 4g^2/\kappa\gamma = 38$. Importantly, interactions between the SiV and single photons becomes deterministic when $C > 1$.

As mentioned in section [Sec. 3.4], we would like to make use of spectrally resolved spin conserving optical transitions ($f_{\uparrow\uparrow'}, f_{\downarrow\downarrow'}$) to build a spin-photon interface using the SiV. Here, we make this criteria more explicit: $f_{\uparrow\uparrow'}$ and $f_{\downarrow\downarrow'}$ can be resolved when $|f_{\uparrow\uparrow'} - f_{\downarrow\downarrow'}| \gtrsim \Gamma$.

3.5.2 Cavity QED in the detuned regime

In the detuned regime ($\Delta > \kappa$), $\Gamma \approx \gamma$, and narrow atom-like transitions are easily resolved under most magnetic field configurations, including when the field is aligned with the SiV symmetry axis [Fig. 3.5(b)]. In this case [sec. 3.4, Ch.2], optical transitions are highly spin-conserving, and many photons can be collected allowing for high-fidelity single-shot readout of the SiV spin state ($F = 0.97$) [Fig. 3.5(c)]. Rapid, high-fidelity, non-destructive single-shot readout can enable projective-readout based initialization: after a single measurement of the SiV spin state, the probability of a measurement-induced spin flip is low, effectively initializing the spin into a known state.

While this regime is useful for characterizing the system, the maximum fidelity of spin-photon entanglement based on reflection amplitude is limited. As seen in figure 3.5(b), the contrast in the reflection signal between an SiV in $|\uparrow\rangle$ (orange) vs. $|\downarrow\rangle$ (purple) is only $\sim 80\%$, implying that in 20% of cases, a photon is reflected from the cavity independent of the spin state of the SiV, resulting in errors. We note that the residual 20% of reflection can be compensated by embedding the cavity inside an interferometer at the expense of additional technical stabilization challenges, discussed below.

3.5.3 Cavity QED near resonance

Tuning the cavity onto the atomic resonance ($\Delta \approx 0$) dramatically improves the reflection contrast [Fig. 3.5(a) (blue curve)]. Here, we observe nearly full contrast of the reflection spectrum due to the presence of the SiV. Unfortunately, this is associated with a broadened atomic linewidth ($\Gamma = \gamma(1 + C)$ $\sim$4 GHz). While it is, in principle, still possible to split the atomic lines by going to higher magnetic fields, there are several technical considerations which make this impractical. Large magnetic fields ($|B_{\text{ext}}|$ >0.5 T) correspond to large qubit frequencies ($f_{\uparrow\downarrow}$), which can induce spontaneous qubit decay due to phonon emission ($|\uparrow\rangle \rightarrow |\downarrow\rangle$), as well as increased local heating of the device from microwave dissipation, both of which reduce the SiV spin coherence time rendering it ineffective as a quantum memory.

At intermediate detunings ($0 < \Delta < \kappa$), the SiV resonance is located on the cavity slope and results in high-contrast, spin-dependent Fano lineshapes which exhibit sharp features smaller than Γ [Fig. 3.5(a), orange curve]. By working at an optimal B_{ext} where the peak of one spin transition is overlapped by the valley of the other, the best features of the resonant and far-detuned regimes are recovered [Fig. 3.5(e)]. Probing the system at the point of maximum contrast ($f_Q \approx (|f_{\uparrow\uparrow'} - f_{\downarrow\downarrow'}|)/2$, contrast $> 90\%$) enables single-shot readout of the SiV spin state for an arbitrary field orientation, even when transitions are not cycling [Fig. 3.5(f)].

This demonstrates an optical regime of cavity QED where we simultaneously achieve high-contrast readout while maintaining spin-dependent transitions. In this regime, we still expect residual reflections of about 10%, which end up limiting spin-photon entanglement fidelity. This infidelity arises because the cavity is not perfectly critically coupled ($\kappa_l \neq \kappa_{tot}/2$), and can in principle be solved by engineering devices that are more critically coupled. Alternatively, this problem can be addressed for any cavity by interfering the signal with a coherent reference to cancel unwanted reflections. In this case, one would have to embed the cavity in one arm of a stabilized interferometer. This is quite challenging, as it involves stabilizing $\sim 10\,\mathrm{m}$ long interferometer arms, part of which lie inside the DR (and experience strong vibrations from the pulse-tube cryocooler).

A fundamental issue with critically coupled cavities is that not all of the incident light is reflected from the device. If the spin is not initialized in the highly-reflecting state, photons are transmitted and not recaptured into the fiber network. Switching to overcoupled (single-sided) cavities, where all photons are reflected with a spin-dependent phase, could improve both the fidelity and efficiency of spin-photon entanglement. Once again, however, measurement of this phase would require embedding the cavity inside of a stabilized interferometer. As such, the un-compensated reflection amplitude based scheme employed here is the most technically simple approach to engineering spin-photon interactions.

3.6 Microwave spin control

While the optical interface described in previous sections enables high-fidelity initialization and readout of the SiV spin qubit, direct microwave driving is the most straightforward path towards coherent single-qubit rotations. Typically, microwave manipulation of electron spins requires application of significant microwave power. This presents a challenge, as SiV spins must be kept at local temperatures below 500 mK in order to avoid heating-related dephasing. In this section, we implement coherent microwave control of SiV centers inside nanostructures at temperatures below 500 mK.

3.6.1 Generating microwave single-qubit gates

The SiV spin is coherently controlled using amplitude and phase controlled microwave pulses generated by a Hittite signal generator (HMC-T2220). A target pulse sequence is loaded onto an arbitrary waveform generator (Tektronix AWG 7122B), which uses a digital channel to control a fast, high-extinction MW-switch (Custom Microwave Components, CMCS0947A-C2), and the analog channels adjust the amplitude and phase via an IQ-mixer (Marki, MMIQ-0416LSM). The resulting pulse train is subsequently amplified (Minicircuits, ZVE-3W-183+) to roughly 3 W of power, and sent via

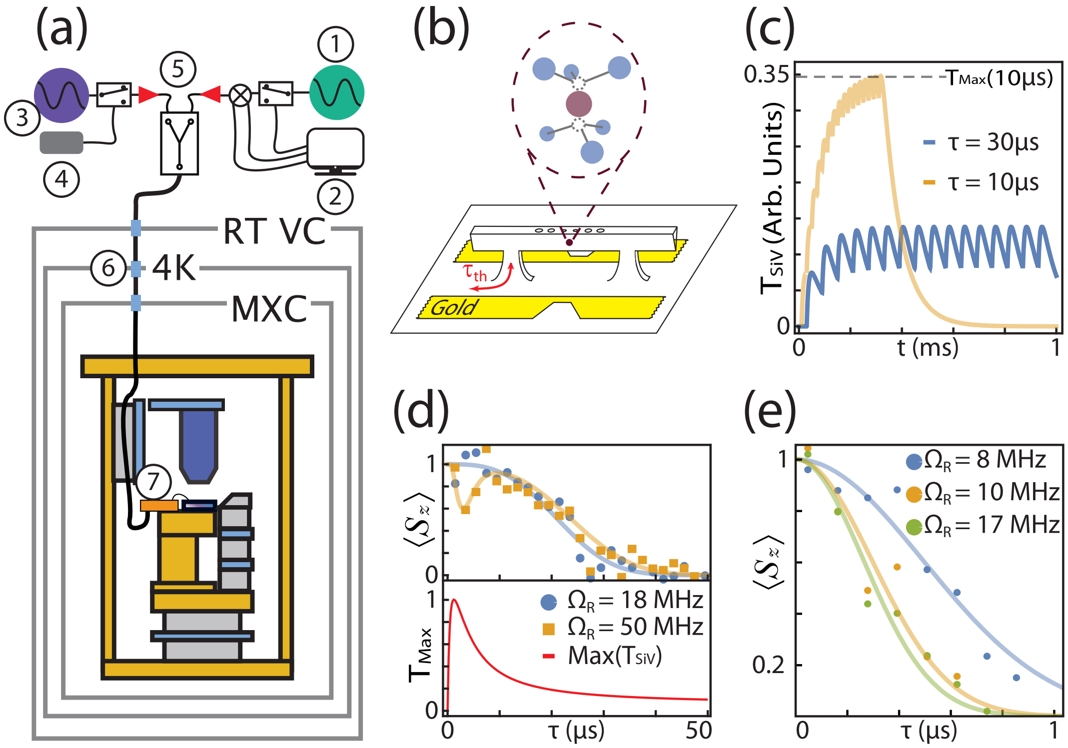

Figure 3.6: (a) Experimental schematic for microwave control. The amplitude and phase of a CW microwave source ① are modulated via a microwave switch and IQ mixer controlled externally by an AWG ②. A CW radio frequency source ③ is controlled using a digital delay generator ④. Both signals are amplified by 30dB amplifiers ⑤ before entering the DR. 0dB cryo-attenuators ⑥ thermalize coax cables at each DR stage, ultimately mounted to a PCB ⑦ on the sample stage and delivered to the devices. (b) Schematic depicting microwave-induced heating of devices. (c) Modeled temperature at the SiV from a dynamical decoupling sequence. At long τ, device cools down between each decoupling pulse, resulting in low temperatures. At short τ, devices are insufficiently cooled, resulting in a higer max temperature ($T_{\max}$). (d) Effects of microwave heating on SiV coherence time. (Top panel) At high Rabi frequencies, SiV coherence is temporarily reduced for small τ. (Bottom panel) The local temperature ($T_{\max}$) at the SiV calculated by taking the maximum value of the plots in figure (c). (e) Hahn-echo for even lower Rabi frequencies, showing coherence times that scale with microwave power

a coaxial cable into the dilution refrigerator. At each cryogenic flange, a 0 dB attenuator is used to thermalize the inner and outer conductors of the coaxial line while minimizing microwave dissipation. The signal is then launched into a coplanar waveguide on a custom-built circuit board (Rogers4003C, Bay Area Circuits) so it can be wire-bonded directly to the diamond chip [Sec. 3.2, Fig. 3.6(c)]. The qubit frequency ($f_{\downarrow\uparrow}$) is measured by its optically detected magnetic resonance spectrum (ODMR) identically to the method described in chapter 2. We observe ODMR from 2 GHz to 20 GHz (corresponding to fields from 0.1 T to 0.7 T), implying that microwave control of SiV centers in this configuration is possible at a wide variety of external field magnitudes. This allows the freedom of tuning the field to optimize other constraints, such as for resolving spin transitions [Sec. 3.5] and identifying ancillary nuclear spins [Sec. 3.9].

Once the qubit frequency has been determined for a given field, single-qubit gates are tuned up by measuring Rabi oscillations. The frequency of these oscillations scales with the applied microwave power $\Omega_R \sim \sqrt{P}$ and determines the single-qubit gate times. We can perform π-pulses (R^{π}_{ϕ}) in under 12 ns, corresponding to a Rabi frequency exceeding 80 MHz [Ch. 4]. This coherent control is used to implement pulse-error correcting dynamical decoupling sequences, either CPMG-N sequences of the form $R^{\pi/2}_x - \left(\tau - R^{\pi}_y - \tau\right)^N - R^{\pi/2}_x = x - (Y)^N - x$[98] or XY8-N sequences of the form $x - (XYXYYXYX)^N - x$[138]. Sweeping the inter-pulse delay τ measures the coherence time T_2 of the SiV.

3.6.2 Effects of microwave heating on coherence

As mentioned in sections 3.3 and 3.4, thermally induced T_1 relaxation can dramatically reduce SiV coherence times. To explain this phenomenon, we model the nanobeam as a $1D$ beam weakly coupled at two anchor points to a uniform thermal bath [Fig. 3.6(b)]. Initially, the beam is at the steady-state base temperature of the DR. A MW pulse instantaneously heats the bath, and the beam rethermalizes on a timescale τ_{th} set by the thermal conduction of diamond and the beam geometry. Once the pulse ends, this heat is extracted from the beam on a similar timescale. By solving the time-dependent 1-D heat equation, we find that the change in temperature at the SiV caused by a single pulse (starting at time t_0) scales as $T_{\mathrm{SiV}} \propto (e^{-(t-t_0)/\tau_{\mathrm{th}}} - e^{-9(t-t_0)/\tau_{\mathrm{th}}})$. We take the sum over N such pulses to model the effects of heating from a dynamical-decoupling sequence of size N.

At early times ($\tau < \tau_{\mathrm{th}}$), the SiV does not see the effects of heating by the MW line, and coherence is high. Similarly, at long times ($\tau \gg \tau_{\mathrm{th}}$) a small amount of heat is able to enter the nanostructure and slightly raise the local temperature, but this heat is dissipated before the next pulse arrives [Fig. 3.6(c), blue curve]. At intermediate timescales however, a situation can arise where the nanobeam has not fully dissipated the heat from one MW pulse before the second one arrives [Fig. 3.6(c), orange curve]. We plot the maximum temperature as seen by the SiV as a function of pulse spacing [Fig. 3.6(d), lower panel], and observe a spike in local temperature for a specific inter-pulse spacing τ, which depends on τ_{th}. Dynamical-decoupling sequences using high Rabi frequency pulses reveal a collapse in coherence at a similar time [Fig. 3.6(d), upper panel]. This collapse disappears at lower Rabi frequencies, suggesting that it is associated with heating-related dephasing. We fit this collapse to a model where the coherence time T_2 depends on temperature[44], and extract the rate of heating $\tau_{\text{th}} = 70\,\text{s}$.

Typically, faster π-pulses improve measured spin coherence by minimizing finite-pulse effects and detuning errors. Unfortunately, as seen above, faster pulses require higher MW powers which cause heating-related decoherence in our system. We measure Hahn-echo at lower MW powers [fig. 3.6(e)], and find MW heating limits T_2 even at $\Omega_R \sim 10\,\text{MHz}$. For applications where long coherence is important, such as electron-nuclear gates [Sec. 3.9], we operate at an optimal Rabi frequency $\Omega_R = 2\pi \times 10\,\text{MHz}$ where nuclear gates are as fast as possible while maintaining coherence for the entire gate duration. For applications such as spin-photon entangling gates where fast gates are necessary [Sec. 3.8], we operate at higher Rabi frequencies $\Omega_R = 2\pi \times 80\,\text{MHz}$ at the cost of reduced coherence times.

Heating related effects could be mitigated by using superconducting microwave waveguides. This approach would also enable the fabrication of a single, long superconducting waveguide that could simultaneously address all devices on a single chip. However, it is still an open question whether or not superconducting waveguides with appropriate critical temperature, current, and field properties can be fabricated

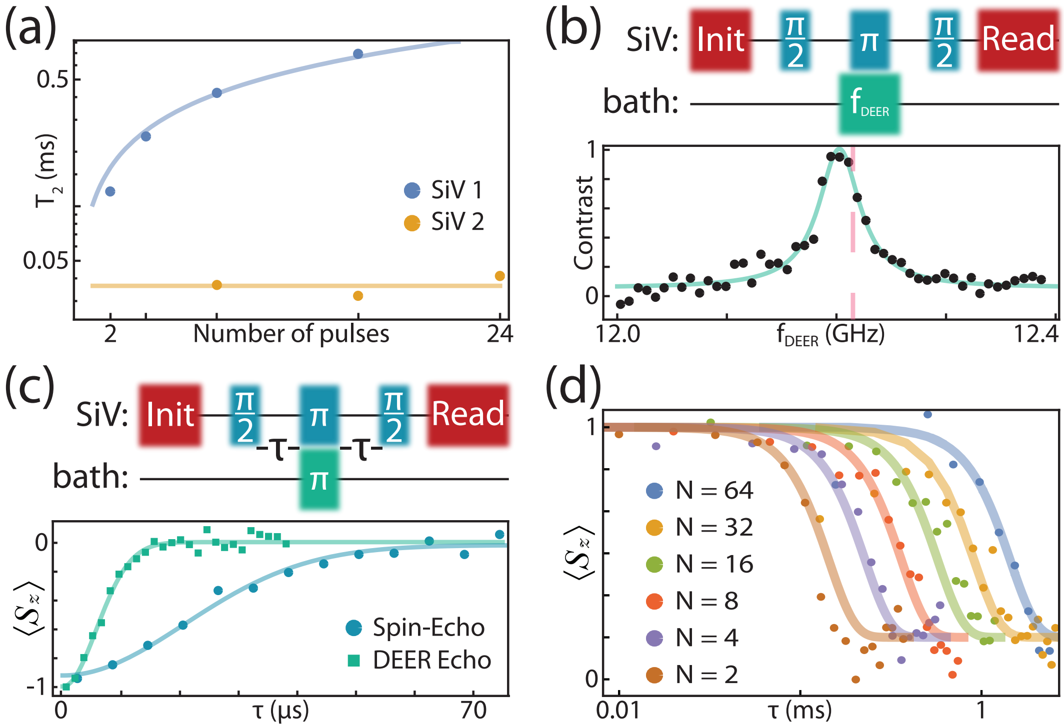

Figure 3.7: (a) T2 scaling for two different SiVs. SiV 2 exhibits no scaling with number of pulses ($T_{2,\mathrm{SiV2}} = 30\,\mathrm{s}$). (b) DEER ESR on SiV 2. Vertical red line is the expected frequency of a $\mathrm{g} = 2$ spin based on our ability to determine the applied external field (Typically to within 10%). (c) DEER Echo on SiV 2. $T_{2,DEER} = 10\,\mathrm{s}$. (d) Dynamical-decoupling on SiV 1. Data points are T_2 measurements used in part (a, blue curve), and solid lines are a noise model consisting of two Lorentzian noise baths.

around diamond nanostructures.

3.7 Investigating the noise bath of SiVs in nanostructures

At low temperatures, the coherence time of SiV centers drastically depends on the surrounding spin bath, which can differ from emitter to emitter. As an example, we note that the T_2 of two different SiV centers in different nanostructures scales differently with the number of applied decoupling pulses [Fig. 3.7(a)]. Surprisingly, the coherence time of SiV 2 does not scale with the number of applied pulses, while the coherence time of SiV 1 does scale as $T_2(N) \propto N^{2/3}$. Notably, both scalings are different as compared to what was previously measured in bulk diamond: $T_2(N) \propto N^1$ [Ch. 2]. In this section, we probe the spin bath of these two SiVs in nanostructures to investigate potential explanations for the above observations.

3.7.1 Double electron-electron resonance spectroscopy of SiVs in nanostructures

In order to investigate the poor coherence of SiV 2, we perform double electron-electron resonance (DEER) spectroscopy[139] to probe the spin bath surrounding this SiV. We perform a Hahn-echo sequence on the SiV, and sweep the frequency of a second microwave pulse (taking the RF path in figure 3.6(a)), contemporaneous with the echoing SiV π-pulse [Fig. 3.7(b), upper panel]. If this second pulse is resonant with a spin bath coupled to the SiV, the bath can flip simultaneously with the SiV, leading to increased sensitivity to noise from the bath [Fig. 3.7(b), lower panel]. We observe a significant reduction of coherence at a frequency consistent with that of a free-electron spin bath ($\mathrm{g}_{\mathrm{bath}} = 2$) (resonance expected at 12(1) GHz).

Next, we repeat a standard Hahn-echo sequence where a π-pulse resonant with this bath is applied simultaneously with the SiV echo pulse (DEER echo). The coherence time measured in DEER echo is significantly shorter than for standard spin-echo, indicating that coupling to this spin bath is a significant source of decoherence for this SiV. One possible explanation for the particularly severe bath surrounding this SiV is a thin layer of alumina (Al_2O_3) deposited via atomic layer deposition on this device in order to tune cavities closer to the SiV transition frequency. The amorphous oxide layer–or its interface with the diamond crystal–can be host to a large number of charge traps, all located within $\sim$50 nm of this SiV. Unfortunately, we could not measure this device without alumina layer due to our inability to gas-tune the nanophotonic cavity close enough to the SiV resonance [Sec. 3.3].

These observations are further corroborated by DEER measurements in SiV 1, where the alumina layer was not used (only N_2 was used to tune this cavity). In this device, we observe longer coherence times which scale $T_2(N) \propto N^{2/3}$, as well as no significant signatures from $\mathrm{g}_{\mathrm{bath}} = 2$ spins using DEER spectroscopy. We fit this scaling to a model consisting of two weakly-coupled spin baths [Fig. 3.7(d), Appendix. C.4], and extract bath parameters $b_1 = 5\,\mathrm{kHz}$, $\tau_1 = 1\,\mathrm{s}$, $b_2 = 180\,\mathrm{kHz}$, $\tau_2 = 1\,\mathrm{ms}$, where b corresponds to the strength of the noise bath, and τ corresponds to the correlation time of the noise[97,140].

While the source of this noise is an area of future study, we find that the b_2 term (likely due to bulk impurities) is the dominant contribution towards decoherence in the system [Appendix. C.4]. Removing this term from the model results in coherence times up to a factor of 1000 times larger than measured values. Higher-temperature[39] or *in situ*[141] annealing could potentially mitigate this source of decoherence by eliminating paramagnetic defects such as vacancy clusters. Additionally, by accompanying Si implantation with electron irradiation[71], SiV centers could be created more efficiently, and with reduced lattice damage. Finally, working with isotopically purified diamond samples with very few ^{13}C, a spin-1/2 isotope of carbon, could also result in a reduced spin bath [Ch. 2, Appendix. C.4].

3.8 Spin-photon entanglement

The previous sections of this chapter characterize the SiV as an efficient spin-photon interface and a quantum memory with long-lived coherence. Here, we combine these two properties to demonstrate entanglement between a spin qubit and a photonic qubit. The mechanism for generating entanglement between photons and the SiV can be seen in figure 3.5(b,d): Depending on the spin state of the SiV, photons at the

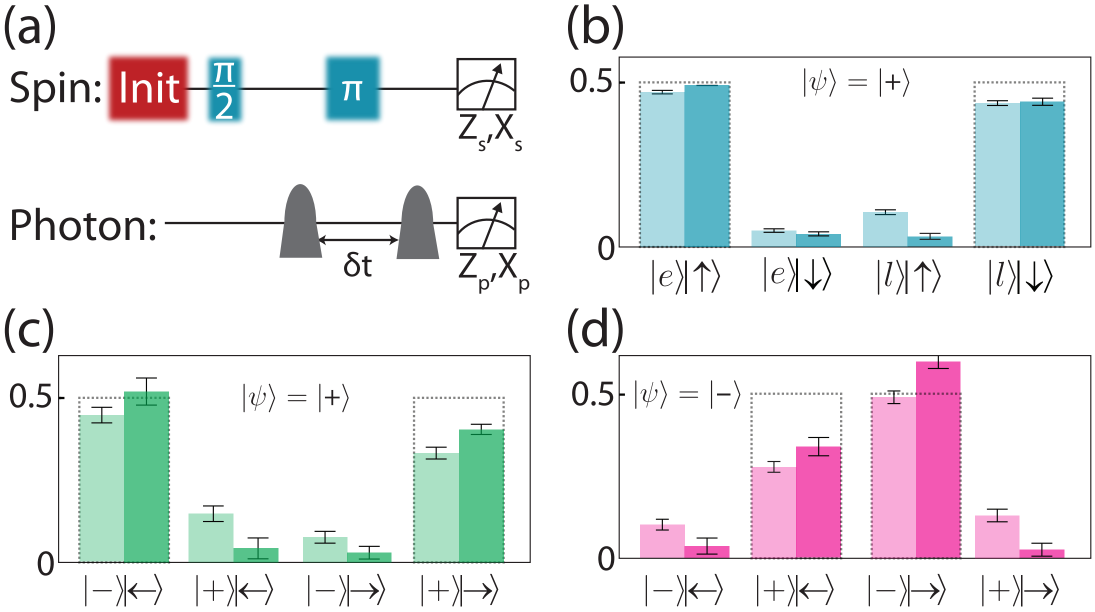

Figure 3.8: (a) Experimental sequence for generating and verifying spin-photon entanglement. A time-bin encoded qubit is reflected by the cavity, and both the SiV and the photonic qubits are measured in the Z and X bases. (b) Spin-photon correlations measured in the Z-Z basis. Light (dark) bars are before (after) correcting for known readout error associated with single-shot readout of the SiV. (c) Spin-photon correlations measured in the X-X basis. Bell-state preparation fidelity of $F \geq 0.89(3)$ and a concurrence $\mathcal{C} \geq 0.72(7)$. (d) Preparation of second spin-photon Bell state. Changing the phase of the incoming photonic qubit prepares a Bell-state with inverted statistics in the X basis.

probe frequency are either reflected from the cavity and detected, or are transmitted and lost.

3.8.1 Generating time-bin qubits

We begin by explaining our choice of time-bin encoding for photonic qubits. One straightforward possibility is to use the Fock state of the photon. However, it is extremely challenging to perform rotations on a Fock state, and photon loss results in an error in the computational basis. Another, perhaps more obvious possibility is to use the polarization degree of freedom. While the SiV spin-photon interface is not polarization selective (both spin states couple to photons of the same polarization), one could consider polarization based spin-photon entangling schemes already demonstated in nanophotonic systems[142,143]. However, this requires embedding the nanostructure inside of a stabilized interferometer, which has a number of challenges [Sec. 3.5]. In addition, it requires careful fabrication of overcoupled, single-sided cavities (unlike the critically coupled diamond nanocavities used here [Sec. 3.2]). As such, we believe time-bin encoding is a natural choice given the critically-coupled SiV-cavity interface described here [Sec. 3.5].

These qubits are generated by passing a weak coherent laser though a cascaded AOM, amplitude-EOM, and phase-EOM. The time-bins are shaped by an AWG-generated pulse on the amplitude-EOM, and are chosen to be much narrower than the delay δt between time bins. We can choose to prepare arbitrary initial photonic states by using the phase-EOM to imprint an optional phase shift to the second bin of the photonic qubit. Since we use a laser with Poissonian photon number statistics, we set the average photon number $\langle n_{ph} \rangle = 0.008 \ll 1$ using the AOM to avoid events where two photons are incident on the cavity.

Using this encoding, measurements in a rotated basis (X-basis) become straightforward. We send the time-bin qubit into an actively stabilized, unbalanced, fiber-based, Mach-Zender interferometer, where one arm passes through a delay line of time δt. With 25% probability, $|e\rangle$ enters the long arm of the interferometer and $|l\rangle$ enters the short arm, and the two time bins interfere at the output. Depending on the relative phase between the two bins, this will be detected on only one of the two arms of the interferometer output [Fig. 3.3(b)], corresponding to a measurement in the X basis of $|\pm\rangle$.

3.8.2 Spin-photon Bell states

We prepare and verify the generation of maximally entangled Bell states between the SiV and a photonic qubit using the experimental sequence depicted in figure 3.8(a). First, the SiV is initialized into a superposition state $|{\rightarrow}\rangle = 1/\sqrt{2}(|{\uparrow}\rangle + |{\downarrow}\rangle)$. Then photons at frequency f_Q [Sec. 3.5] are sent to the cavity, corresponding to an incoming photon state $|+\rangle = 1/\sqrt{2}(|e\rangle + |l\rangle)$, conditioned on the eventual detection of only one photon during the experiment run. Before any interactions, this state can be written as an equal superposition: $\Psi_0 = |\rightarrow\rangle \otimes |+\rangle = 1/2(|e\uparrow\rangle + |e\downarrow\rangle + |l\uparrow\rangle + |l\downarrow\rangle)$. The first time bin is only reflected from the cavity if the the SiV is in state $|\uparrow\rangle$, effectively carving out $|e\downarrow\rangle$ in reflection[22]. A π-pulse on the SiV transforms the resulting state to $\Psi_1 = 1/\sqrt{3}(|e\downarrow\rangle + |l\downarrow\rangle + |l\uparrow\rangle)$. Finally, reflection of the late time-bin off of the cavity carves out the state $|l\downarrow\rangle$, leaving a final entangled state $\Psi_2 = 1/\sqrt{2}(|e\downarrow\rangle + |l\uparrow\rangle)$. To characterize the resulting state, we perform tomography on both qubits in the Z and X bases [Fig. 3.8(a)].

In order to enable high-bandwidth operation and reduce the requirements for laser and interferometric stabilization in generating and measuring time-bin qubits, it is generally beneficial to set δt as small as possible. The minimum δt is determined by two factors: First, each pulse must be broad enough in the time-domain (narrow enough in the frequency domain) so that it does not distort upon reflection off of the device. From figure 3.5(d), the reflection specturm is roughly constant over a $\sim$ 100 MHz range, implying that $\sim$ nanosecond pulses are sufficient. The second consideration is that a microwave π-pulse must be placed between the two pulses. In this experiment, we drive fast (12 ns) π-pulses. As such, we set $\delta t = 30$ ns and use 5 ns optical pulses to satisfy these criteria.

3.8.3 Spin-photon entanglement measurements

For Z-basis measurements, photons reflected from the cavity are sent directly to a SPCM and the time-of-arrival of the time-bin qubit is recorded. Afterwards, the SiV is read out in the Z-basis [Sec. 3.5]. Single-shot readout is calibrated via a separate measurement where the two spin-states are prepared via optical pumping and read out, and the fidelity of correctly determining the $|\uparrow\rangle$ ($|\downarrow\rangle$) state is $F_\uparrow = 0.85$ ($F_\downarrow = 0.84$), limited by the large 0 component of the geometric distribution which governs photon statistics for spin-flip systems [Sec. 3.5]. In other words, since we work in a misaligned field in this experiment, the probability of a spin flip is high, making it somewhat likely to measure 0 photons regardless of initial spin state. Even before accounting for this known error [Appendix. C.5], we observe clear correlations between the photonic and spin qubits [Fig. 3.8(b), light-shading]. Error bars for these correlation histograms (and the following fidelity calculations) are estimated by statistical bootstrapping, where the scattered photon histograms (post-selected on the detection of $|e\rangle$ or $|l\rangle$) are randomly sampled in many trials, and the variance of that ensemble is extracted.

Measurements in the X-basis are performed similarly. The photon is measured through an interferometer as described above, where now the detector path information is recorded for the overlapping time-bin. After a $R_y^{\pi/2}$ pulse on the SiV, the scattered photon histograms again reveal significant correlations between the '+' and '-'

detectors and the SiV spin state [fig. 3.8(c)]. By adding a π-phase between the early and late time bins, we can prepare an orthogonal Bell state. Measured correlations of this state are flipped in the X-basis [Fig. 3.8(d)].

Measurements of this Bell state in the Z- and X-bases are used to estimate a lower bound on the fidelity: $F = \langle \Psi^+ | \rho | \Psi^+ \rangle \geq 0.70(3)$ ($F \geq 0.89(3)$ after correcting for readout errors) [Appendix. C.5]. The resulting entangled state is quantified by its concrrence $\mathcal{C} \geq 0.42(6)$ ($\mathcal{C} \geq 0.79(7)$ after correcting for readout errors) [Appendix. C.5]. This high-fidelity entangled state between a photonic qubit and a quantum memory is a fundamental resource for quantum communication[109] and quantum computing schemes[13], and can be used, for example, to demonstrate heralded storage of a photonic qubit into memory [Ch. 4].

3.9 Control of SiV-^{13}C register

While demonstrations of a quantum node with a single qubit is useful for some protocol, nodes with several interacting qubits enable a wider range of applications, including quantum repeaters[79]. In this section, we introduce additional qubits based on ^{13}C naturally occurring in diamond [sec. 3.7].

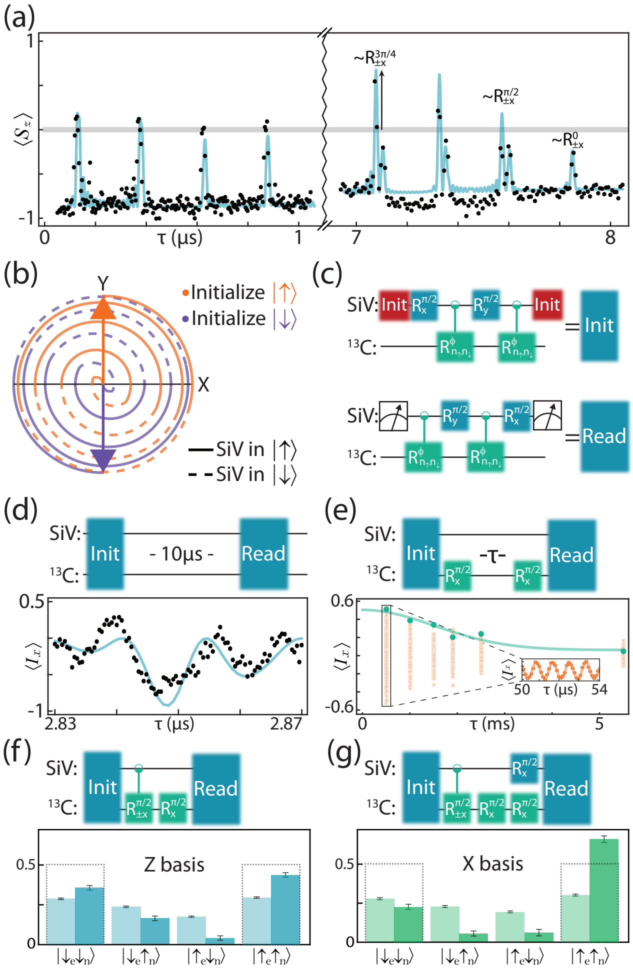

Figure 3.9: (a) XY8-2 spin echo sequence reveals coupling to nuclear spins. (Left panel) Collapses $\langle S_x \rangle = 0$ at short times indicate coupling to many nuclei. (Right panel) Collapses $\langle S_x \rangle \neq 0$ at long times indicate conditional gates on a single nuclear spin. (b) Trajectory of ^{13}C on the Bloch sphere during a maximally entangling gate. Orange (purple) lines correspond to the SiV initially prepared in state $|\uparrow\rangle$ ($|\uparrow\rangle$); transitions from solid to dashed lines represent flips of the SiV electronic spin during the gate. (c) Maximally entangling gates of the form $\mathcal{R}^{\phi}_{\vec{n_\uparrow},\vec{n_\downarrow}}$ are used to initialize and readout the two-qubit register. (d) Tuning up an initialization gate. Inter-pulse spacing τ for Init and Read gates are swept to maximize polarization. Solid line is the modeled pulse sequence using the hyperfine parameters extracted from (a). (e) Nuclear Ramsey measurement. Driving the ^{13}C using composite gates on the SiV reveals $T_2^* \ =2.2\,\mathrm{ms}$. (Inset) Orange points are coherent oscillations of the Ramsey signal due to hyperfine coupling to the SiV. (f) Electron-nuclear correlations measured in the ZZ-basis. Light (dark) bars are before (after) correcting for known errors associated with reading out the SiV and ^{13}C. (g) Electron-nuclear correlations measured in the XX-basis. We estimate a Bell state preparation fidelity of $F \geq 0.59(4)$ and a concurrence $\mathcal{C} \geq 0.22(9)$.

3.9.1 Coupling between the SiV and several ^{13}C

For all of the emitters investigated in section 3.6, we observe collapses in the echo signal corresponding to entanglement with nearby nuclear spins [Fig. 3.9(a)]. As the diamond used in this work has 1% ^{13}C [Sec. 3.7], we typically observe several such nuclei, with all of their resonances overlapping due to their second-order sensitivity to hyperfine coupling parameters [Ch. 4]. Consequently, during a spin echo sequence the SiV entangles with many nuclei, quickly losing coherence and resulting in a collapse to $\langle S_z \rangle = 0$ [Fig. 3.9(a), left side]. If single ^{13}C can be addressed however, this entanglement results in coherent population transfer and echo collapses which can, in some cases, completely flip the SiV spin state ($\langle S_z \rangle = \pm 1$). This entanglement forms the basis for quantum gates [Fig. 3.9(a), right side]. These gates can be tuned by changing the alignment of B_{ext} with respect to the hyperfine coupling tensor, or by using different timings. Unfortunately, as a result of the complicated nuclear bath for this device, a majority of field orientations and amplitudes only show collapses to $\langle S_z \rangle = 0$. The highest fidelity nuclear gates demonstrated here are based on echo resonances with the largest contrast which, crucially, were not commensurate with an aligned field. Thus, in this device, single ^{13}C could only be isolated at the cost of lower SSR fidelity [Sec. 3.5].

3.9.2 Initializing the nuclear spin

Once a single nuclear spin is identified, resonances in spin-echo form the building block for quantum gates. For example, a complete flip of the SiV is the result of the nuclear spin rotating by π conditionally around the axes ±X ($\mathcal{R}^{\pi}_{\pm x,\mathrm{SiV-C}}$), depending on the state of the SiV. We can vary the rotation angle of this pulse by choosing different spacings τ between pulses [Fig. 3.9(a)], or by using different numbers of π-pulses. We find a maximally entangling gate ($\mathcal{R}^{\pi/2}_{\pm x,\mathrm{SiV-C}}$) by applying $N = 8$ π-pulses separated by $2\tau = 2 \times 2.859\,\mu\mathrm{s}$. This can be visualized on the Bloch sphere in figure 3.9(b), where the state of the SiV (orange or purple) induces different rotations of the ^{13}C.

A similarly constructed entangling gate ($\mathcal{R}^{\phi}_{\vec{n_\uparrow},\vec{n_\downarrow}}$, discussed in Appendix C.6) is used to coherently map population from the SiV onto the nuclear spin or map population from the nuclear spin onto the SiV [Fig. 3.9(c)]. The fidelity of these gates is estimated by polarizing the SiV, mapping the population onto the ^{13}C, and waiting for $T \gg T_2^*$ (allowing coherence to decay) before mapping the population back and reading out [Fig. 3.9(d)]. We find that we can recover 80% of the population in this way, giving us an estimated initialization and readout fidelity of $F = 0.9$.

Based on the contrast of resonances in spin-echo (also 0.9), this is likely limited by entanglement with other nearby ^{13}C for this emitter, as well as slightly sub-optimal choices for τ and N. Coupling to other ^{13}C results in population leaking out of our two-qubit register, and can be improved by increasing sensitivity to single ^{13}C, or by looking for a different emitter with a different ^{13}C distribution. The misaligned external field further results in slight misalignment of the nuclear rotation axis and angle of rotation, and can be improved by employing adapted control sequences to correct for these errors[144,145].

3.9.3 Microwave control of nuclear spins

As demonstrated above, control of the ^{13}C via composite pulse sequences on the SiV is also possible. A maximally entangling gate has already been demonstrated and used to initialize the ^{13}C, so in order to build a universal set of gates, all we require are unconditional single-qubit rotations. This is done following reference[146], where unconditional nuclear rotations occur in spin-echo sequences when the inter-pulse spacing τ is halfway between two collapses. For the following gates, we use an unconditional $\pi/2$-pulse composed of 8 π-pulses separated by $\tau = 0.731\,\mathrm{s}$.

We use this gate to probe the coherence time T_2^* of the ^{13}C. After mapping population onto the nuclear spin, the SiV is re-initialized, and then used to perform unconditional $\pi/2$-rotations on the ^{13}C [Fig. 3.9(d)]. Oscillations in the signal demonstrate Larmor precession of the nucleus at a frequency determined by a combination of the external field as well as ^{13}C-specific hyperfine interactions [Ch. 4, which are seen as the orange data points in figure 3.9(d). The green envelope is calculated by fitting the oscillations and extracting their amplitude. The decay of this envelope T_2^* =2.2 ms shows that the ^{13}C has an exceptional quantum memory, even in the absence of any dynamical decoupling.

We characterize the fidelity of our conditional and unconditional nuclear gates by generating and reading out Bell states between the SiV and ^{13}C [Appendix. C.5]. First, we initialize the 2-qubit register into one of the 4 eigenstates: $\{|\uparrow_e\uparrow_N\rangle, |\uparrow_e\downarrow_N\rangle, |\downarrow_e\uparrow_N\rangle, |\downarrow_e\downarrow_N\rangle\}$, then perform a $\pi/2$-pulse on the electron to prepare a superposition state. Afterward, a CNOT gate, comprised of an unconditional $\pi/2$ pulse followed by a maximally entangling gate, prepares one of the Bell states $|\Psi_\pm\rangle, |\Phi_\pm\rangle$ depending on the initial state [Fig. 3.9 (e,f)]. Following the analysis outlined in appendix C.5, we report an error corrected fidelity of $F \geq 0.59(4)$ and $\mathcal{C} \geq 0.22(9)$, primarily limited by our inability to initialize the ^{13}C [Ch. 4].

3.9.4 Radio-frequency driving of nuclear spins

The previous section demonstrated a CNOT gate between SiV and ^{13}C using composite MW pulses. This approach has several drawbacks. First, the gate fidelity is limited by our ability to finely tune the rotation angle of the maximally entangled gate which can not be done in a continuous fashion [Fig. 3.9(a)]. Second, this gate requires a specific number of MW pulses and delays between them, making the gate duration (~50 s in this work) comparable to the SiV coherence time. Finally, this scheme re-

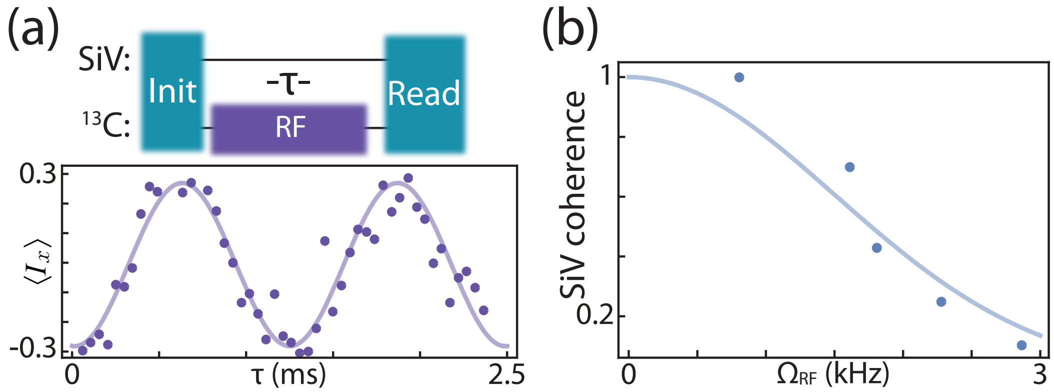

Figure 3.10: (a) RF Rabi oscillations. Applying an RF tone directly drives nuclear rotations of a coupled ^{13}C. (b) SiV coherence in the presence of an RF drive. As the strength of the RF drive is increased, local heating from the CPW reduces the SiV T_2.

lies on a second order splitting of individual ^{13}C resonances to resolve individual ones; residual coupling to additional ^{13}C limits the fidelity for a pulse sequence of given total length.

Direct RF control[122] would be a simple way to make a fast and high-fidelity CNOT gate since it would require a single RF π-pulse on a nuclear spin transition[147]. Furthermore, since the nuclear spin transition frequencies depend on the hyperfine coupling to leading order, these pulses could have higher ^{13}C selectivity and potentially shorter gate duration.

We use the RF port inside the DR [Sec. 3.6] to apply RF pulses resonant with nuclear spin transitions. Figure 3.10(a) shows RF Rabi oscillations of the nuclear spin. Since the ^{13}C gyromagnetic ratio is about 3 orders of magnitude smaller compared to the SiV spin, RF driving is much less efficient than MW one and requires much more power. To investigate local heating of the SiV [Sec. 3.6] we measured the SiV spin coherence contrast in spin-echo sequence right after applying off-resonant RF pulse of 100 s at different power (calibrated via RF rabi oscillations) [Figure 3.10(b)]. Unfortunately, Even modest Rabi frequencies (Ω_{RF} ~1 kHz) result in 20% loss in SiV coherence. Replacing the gold CWG used in this work by superconducting ones may solve heating issue and make RF driving practically useful.

3.10 Conclusion

The SiV center in diamond has rapidly become a leading candidate to serve as the building block of a future quantum network. In this work, we describe the underlying technical procedures and optimal parameter regimes necessary for utilizing the SiV-nanocavity system as a quantum network node. In particular, we discuss the effect of static and dynamic strain on the properties of the SiV spin qubit and its optical interface, with direct application to quantum networking experiments. We demonstrate techniques for coherently controlling and interfacing SiV spin qubits inside of nanophotonic structures at millikelvin temperatures to optical photons. Finally, we identify and coherently control auxiliary nuclear spins, forming a nanophotonic two-qubit register.

The work presented here and in the following chapter illustrates the path towards the realization of a first-generation quantum repeater based on SiV centers inside diamond nanodevices. We note that a key ingredient enabling future, large-scale experiments involving several solid-state SiV-nanocavity nodes will be the incorporation of strain tuning onto each device[148]. Precise tuning of both the static and dynamic strain can overcome the limitations of inhomogeneous broadening and spectral diffusion, and enable scalable fabrication of quantum repeater nodes [Sec. 3.4].

4

Quantum network nodes based on diamond qubits with an efficient nanophotonic interface

This chapter has been published as

"Quantum network nodes based on diamond qubits with an efficient nanophotonic interface"

C. T. Nguyen, D. D. Sukachev, M. K. Bhaskar, B. Machielse, D. S. Levonian, E. N. Knall, P. Stroganov, R. Riedinger, H. Park, M. Lončar and M. D. Lukin Phys. Rev. Lett. 123, 183602 (2019)

4.1 Introduction

The realization of quantum networks is one of the central challenges in quantum science and engineering with potential applications to long-distance communication, non-local sensing and metrology, and distributed quantum computing[13,14,17,18,109]. Practical realizations of such networks require individual nodes with the ability to process and store quantum information in multi-qubit registers with long coherence times, and to efficiently interface these registers with optical photons. Cavity quantum electrodynamics (QED) is a promising approach to enhance interactions between atomic quantum memories and photons[23,111,112,113,149]. Trapped atoms in optical cavities are one of the most developed cavity QED platforms for quantum processing, and have demonstrated gates between atoms and photons[20] as well as interactions between multiple qubits mediated by the optical cavity[22]. While these experiments have demonstrated all of the individual components needed for a quantum network, combining them to realize a full-featured node remains an outstanding challenge.

Nanophotonic cavity QED systems with solid-state emitters are appealing candidates for realizing quantum nodes as they can be interfaced with on-chip electronic control and photonic routing, making them suitable for integration into large-scale networks[23,116]. Numerous advances towards the development of such nodes have been made recently. Self-assembled quantum dots in GaAs have been efficiently interfaced with nanophotonic structures, enabling a fast, on-chip spin-photon interface[23,24]. Nitrogen-vacancy color centers in diamond (NVs) have demonstrated multi-qubit quantum processors with coherence times approaching one minute[26], and have been used to implement quantum error correction[118] and teleportation[119]. Despite this rapid progress, functional nodes combining all the necessary ingredients in a single device have not yet been realized. For example, quantum memory times in quantum dots are limited to a few s by the dense bath of surrounding nuclear spins[25]. Conversely, an efficient nanophotonic interface to NVs remains elusive, in part due to the degradation of their optical properties inside nanostructures arising from electrical noise induced by the fabrication[86,150].

In this chapter, we demonstrate an integrated network node combining all key ingredients required for a scalable quantum network. This is achieved by coupling a negatively charged silicon-vacancy color-center (SiV) to a diamond nanophotonic cavity and a nearby nuclear spin, illustrated schematically in Fig. 4.1(a). The SiV is an optically active point defect in the diamond lattice[37,123]. Its D_{3d} inversion symmetry

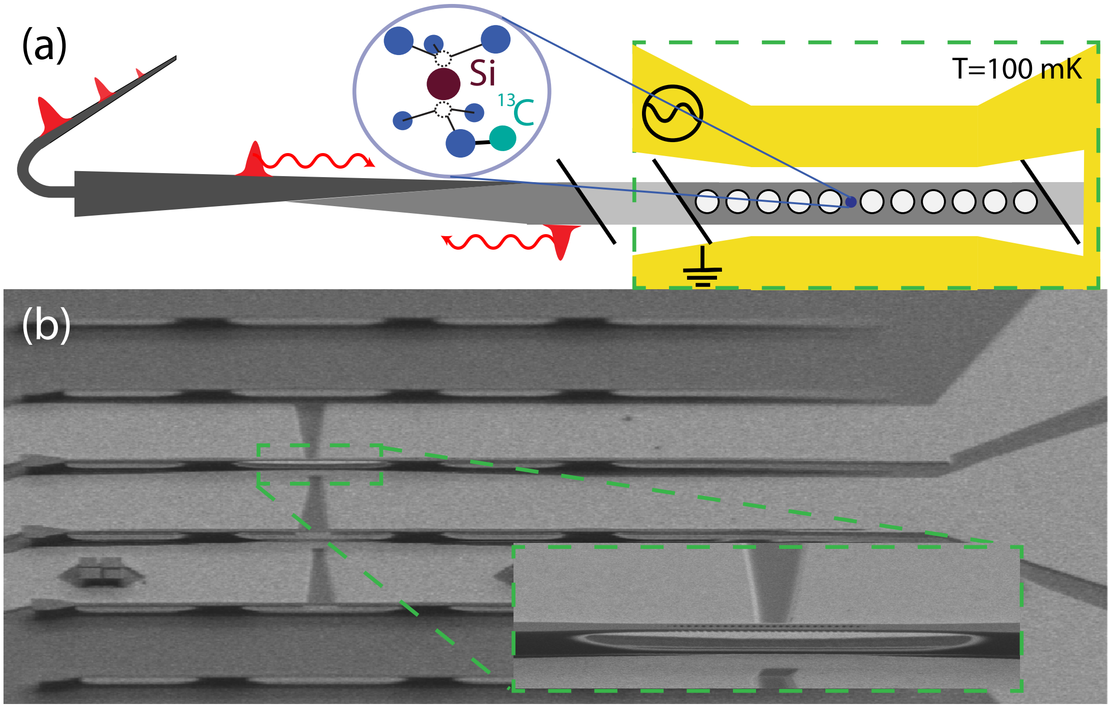

Figure 4.1: (a) Schematic of a SiV-nanophotonic quantum register. A diamond nanostructure with embedded SiV centers and ancillary ^{13}C nuclei are coupled via a waveguide to a fiber network. Spins are controlled by an on-chip microwave CPW at $0.1\,\mathrm{K}$. (b) Scanning electron micrograph of several devices. The gold CPW is designed to localize microwave fields around the cavity center (green inset).

results in a vanishing electric dipole moment of the ground and excited states, rendering optical transitions insensitive to electric field noise typically present in nanofabricated structures[40,89]. We enhance interactions between SiVs and optical photons by incorporating them into nanocavities [Ch. 3], which are critically coupled to on-chip waveguides. Itinerant photons in a fiber network are adiabatically transferred to this waveguide, allowing for the collection of reflected photons with efficiencies exceeding 90%[129]. After an initial optical characterization of the devices, a shorted, gold coplanar waveguide (CPW) is deposited in close proximity to a small subset of cavities [Fig. 4.1 (b), inset, Ch. 3]. This enables coherent microwave manipulation of the SiV ground state spin in a cryogenic environment ($T < 0.1\,\mathrm{K}$), where phonon-mediated dephasing and relaxation processes are mitigated[44,46].

In what follows, we characterize these devices in the context of the three key ingredients of a quantum network node: (i) an efficient spin-photon interface, (ii) a long-lived quantum memory, and (iii) access to multiple interacting qubits.

4.2 The SiV spin-photon interface

The efficient spin-photon interface is enabled by coupling to a diamond nanophotonic cavity. For critically-coupled cavities, the presence of an SiV modulates the bare nanocavity reflection spectrum with the strength of this modulation parametrized by the cavity cooperativity $C = 4g^2/(\kappa\gamma) \sim 38$ (with the single photon Rabi fre-

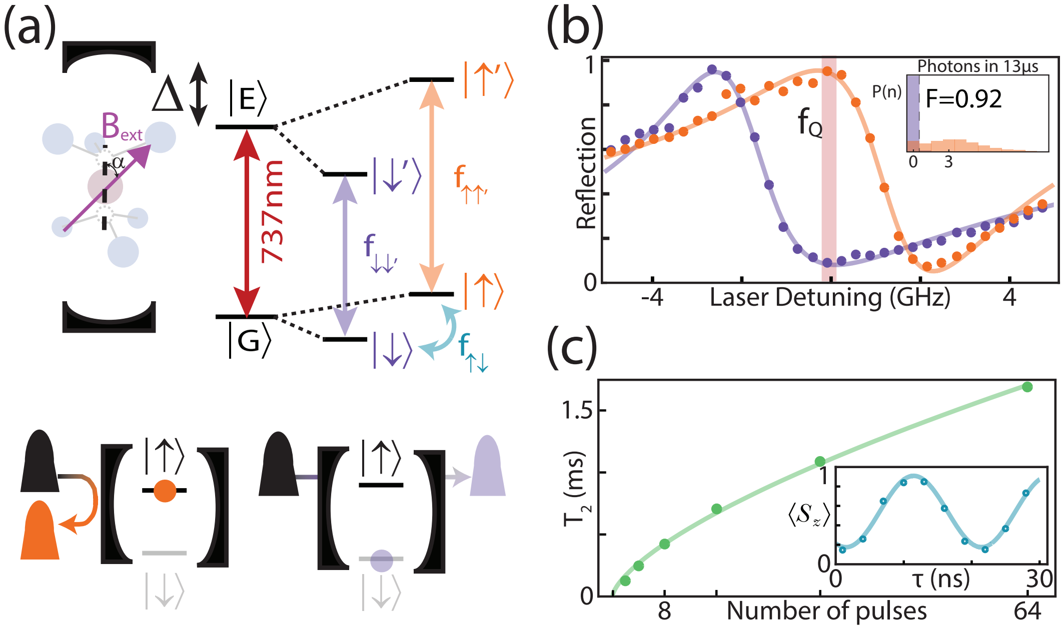

Figure 4.2: (a) Level structure of SiV spin-cavity system. The SiV optical transition at $737\,\mathrm{nm}$ is coupled to the nanocavity with detuning Δ. Spin conserving transitions (purple, orange) are split by an external magnetic field ($\mathbf{B}_{\mathrm{ext}}$), at an angle α with respect to the SiV symmetry axis. Photons at frequency f_Q are preferentially reflected by the cavity when the SiV is in state $|\uparrow\rangle$. Microwave fields at frequency $f_{\uparrow\downarrow}$ coherently drive the qubit states. (b) Spin-dependent reflection spectrum for $B_{ext} = 0.19\mathrm{T}$, $\alpha \approx \pi/2$ at $\Delta = 0.25\kappa$. Probing at the point of maximum contrast (f_Q) results in high-fidelity spin-photon correlations and single-shot readout (inset, $F = 0.92$). (c) SiV spin coherence time $T_2(N=64) > 1.5\,\mathrm{ms}$ with dynamical decoupling. (inset) Fast microwave Rabi driving of the SiV spin.

quency, cavity, and atomic energy decay rate $\{g, \kappa, \gamma\} = 2\pi \times \{5.6, 33, 0.1\}$ GHz). For $C > 1$, we expect high-contrast modulation for a small detuning (Δ) between the cavity and the SiV resonance near 737nm. An external field B_{ext} lifts the degeneracy of the SiV spin-$\frac{1}{2}$ sub-levels, creating spin-dependent reflection: photons at the frequency of maximum contrast (f_Q) are reflected from the cavity only when the SiV is in a specific spin state ([Fig. 4.2(a)], $|\uparrow\rangle$). In previous works, spin readout of the SiV was performed with B_{ext} parallel to the SiV symmetry axis, where the spin-conserving transitions are highly cycling [Ch. 2]. The high collection efficiency into a tapered fiber allows for fast single-shot readout of the SiV even in a misaligned field [Fig. 4.2(b)], which is necessary for the nuclear spin control described below. We observe a readout fidelity of $F = 0.92$ in 13 s even when only a few (~ 10) photons are scattered.

We next demonstrate that the SiV spin in a nanocavity is a suitable quantum memory. Microwave pulses at $f_{\uparrow\downarrow} = 6.7\,\text{GHz}$ coherently manipulate the SiV spin qubit. The resulting Rabi oscillations, which can be driven in excess of 80 MHz while maintaining acceptable sample temperatures [Ch. 3], are shown in the inset of Fig. 4.2(c). These rotations are used to probe the coherence properties of the spin via dynamical decoupling sequences [Fig. 4.2(c)][96,151]. We measure the coherence time of the SiV inside the nanocavity to be $T_2 > 1.5\,\text{ms}$ for XY8 dynamical decoupling sequences [Ch. 3], and scale with the number of decoupling pulses as $T_2 \propto N^{2/3}$. The coherence scaling observed here differs from that observed in bulk diamond [Ch. 2], and is similar to NVs near surfaces[140]. This suggests that SiV memory in nanostructures is limited by an electron spin bath, for example residing near the surface of the nanostructure or resulting from implantation-induced damage [Ch. 3].

4.3 Storing photonic qubits in SiV memory

We now combine the efficient spin-photon interface and control over the SiV spin state to demonstrate heralded storage of photonic qubit states in the spin-memory, a key feature of a network node[112]. Fig. 4.3(a) outlines the experimental scheme, where photonic qubits are prepared using time-bin encoding and mapped onto the SiV spin. In our experiments, the SiV is first initialized into a superposition state $|{\rightarrow}\rangle \propto |{\uparrow}\rangle + |{\downarrow}\rangle$ by optical pumping followed by a microwave $\frac{\pi}{2}$-pulse. A pair of weak coherent pulses separated by $\delta t = 30\,\mathrm{ns}$ at frequency f_Q are then sent to the cavity. The single photon sub-space corresponds to an incoming qubit state $|\Psi_{\mathrm{i}}\rangle \propto \beta_e |e\rangle + \beta_l |l\rangle$, where $|e\rangle$ ($|l\rangle$) denotes the presence of a photon in the early (late) time-bin. As a photon can only be reflected from the device if the SiV is in state $|{\uparrow}\rangle$ [Fig. 4.2(a)], particular components of the initial product state can be effectively ”carved out”[22]. We invert the SiV spin with a π-pulse between the arrival of the two time bins at the cavity, such that a photon detection event indicates that the final state has no $|e\uparrow\rangle$ or $|l\downarrow\rangle$ component. This leaves the system in the final spin-photon entangled state $|\Psi_{\mathrm{f}}\rangle \propto \beta_e |e\downarrow\rangle + \beta_l |l\uparrow\rangle$. The reflected photon enters a time-delay interferometer, where one arm passes through a delay line of length δt, allowing the two time-bins to

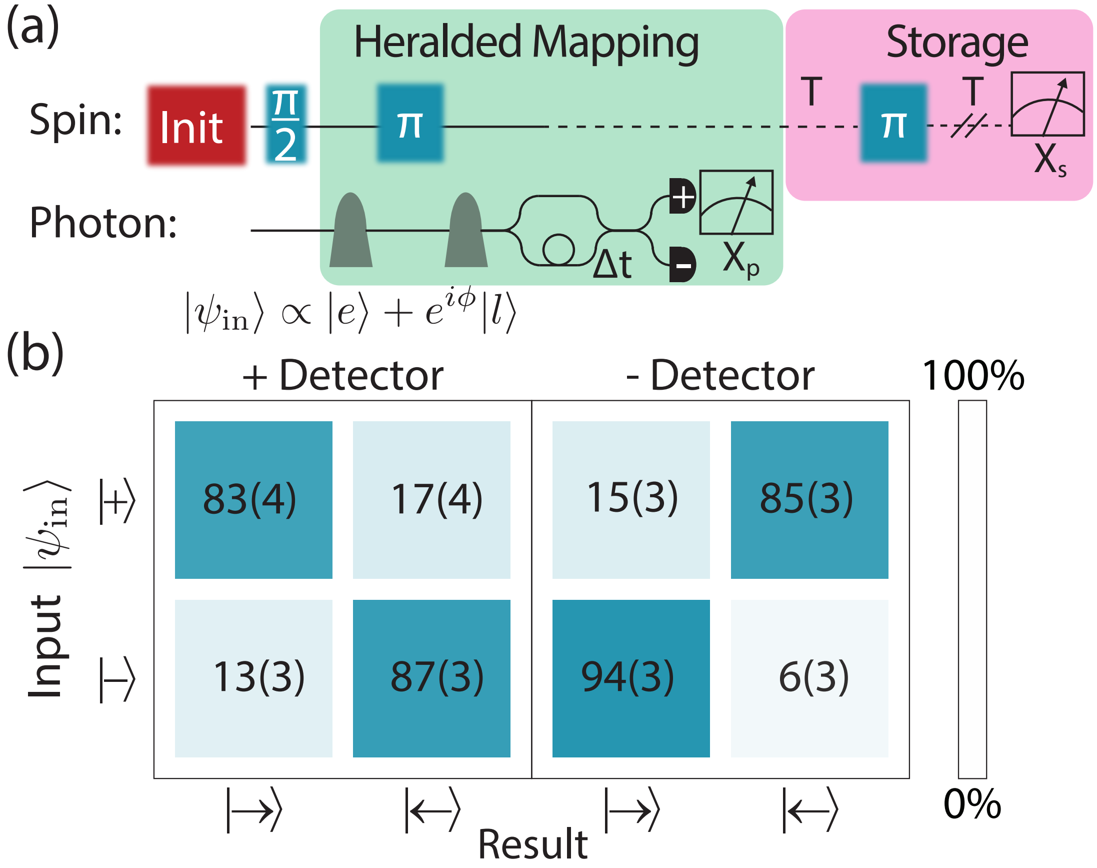

Figure 4.3: (a) Schematic for heralded photon storage. First, the SiV is prepared in a superpostion of two spin states, then a photonic qubit is reflected off the device, flipping the spin state between the time bins. Detection of the photon in the X basis (X_p) heralds mapping of the qubit onto the spin (green box). The qubit is stored in memory for $2T = 20\,\mathrm{s}$ with dynamical decoupling on the SiV (pink box). (b) Spin-photon storage fidelity. The state $|\pm\rangle = |\downarrow\rangle \pm |\uparrow\rangle$ is mapped onto the SiV, with average fidelity $\mathcal{F} = 87(6)\%$.

interfere and erase which-time-bin information. As can be seen by expressing the final state in the corresponding photon basis:

$$|\psi\rangle_{\mathrm{f}} \propto |+\rangle\,(\beta_e\,|{\downarrow}\rangle + \beta_l\,|{\uparrow}\rangle) + |-\rangle\,(\beta_e\,|{\downarrow}\rangle - \beta_l\,|{\uparrow}\rangle), \tag{4.1}$$

a detection event on either the '+' or '−' arm of the interferometer represents a measurement in the X-basis ($|\pm\rangle \propto |e\rangle \pm |l\rangle$), effectively teleporting the initial photonic state onto the electron (up to a known local rotation). We experimentally verify generation of the entangled state $|\psi\rangle_{\mathrm{f}}$ for input states $|\psi\rangle_{\mathrm{i}} = |\pm\rangle$ by measuring spin-photon correlations [Appendix C], and use it to extract a teleportation fidelity of 0.92(6).

After detection of the heralding photon, we store the teleported photonic states (initially prepared in $|+\rangle$ or $|-\rangle$) in spin memory for 20 s by applying an additional decoupling π-pulse on the SiV spin. Finally, we measure the SiV spin state via local rotations followed by projective readout, and find that the overall fidelity of teleportation and storage is $F = 0.87(6)$ after corrected for readout errors [Fig. 4.3(b)]. The quantum storage time can be extended by additional decoupling sequences [Fig. 4.2(c)], enabling entanglement distribution up to a T_2-limited range of 500 km.

4.4 Multi-qubit registers in diamond cavities

In order to extend this range and to enable more generic quantum communication protocols, we next demonstrate a two-qubit register based on the cavity coupled SiV electronic spin and a nearby ^{13}C nuclear memory. The ^{13}C isotope of carbon is a spin-$\frac{1}{2}$ nucleus which has $\sim$ 1% natural abundance in diamond, and is known to exhibit exceptional coherence times[26]. While direct radio-frequency manipulation of nuclear spins is impractical due to heating concerns [Ch. 3], control over ^{13}C spins can be achieved by adapting electron mediated techniques developed for Nitrogen vacancy (NV) centers[117,146,152,153]. The physical principle of the SiV-^{13}C interaction is depicted in Fig. 4.4(a). The SiV generates a spin-dependent magnetic field $\mathbf{B}_{\mathrm{SiV}}$ at the position of the ^{13}C, which is located a few lattice sites away. This is described by a hyperfine interaction Hamiltonian:

$$\hat{H}_{\mathrm{HF}} = \hbar A_{\parallel} \frac{\hat{S}_z}{2} \frac{\hat{I}_z}{2} + \hbar A_{\perp} \frac{\hat{S}_z}{2} \frac{\hat{I}_x}{2} \tag{4.2}$$

where $\hat{S}_{z,x}$ ($\hat{I}_{z,x}$) are the Pauli operators for the electron (nuclear) spin, and $A_{\parallel,\perp}$ are the coupling parameters related to the parallel and perpendicular components of B_{SiV} with respect to the bias field B_{ext}[146,153,154]. Hyperfine interactions manifest themselves in spin-echo measurements as periodic resonances[146], shown in Fig. 4.4(b) for an XY8-2 decoupling sequence $\pi/2 - (\tau - \pi - \tau)^{16} - \pi/2$, where τ is the free evolution time. The coherence envelope for this sequence is $T_2(N = 16) = 603\,\mathrm{s}$ [Fig. 4.4(b), upper panel].

For weakly coupled ^{13}C ($A_\perp \ll \omega_l$, and $A_\parallel \ll \omega_l$, as used in this letter), the positions of the resonances[146]

$$\tau_k \approx \frac{2k+1}{2\omega_l}\left(1 - \frac{1}{2}\left(\frac{A_\perp}{2\omega_l}\right)^2\right), \tag{4.3}$$

where ω_l is the larmor frequancy of a bare ^{13}C, are insensitive to specific ^{13}C hyperfine parameters at first order, rendering them indistinguishable at early times ($\tau_k \ll 4\,\mathrm{s}$, [Fig. 4.4(b), red inset]). Individual ^{13}C can be isolated at longer times[146], and are used to engineer gates between a single ^{13}C and the SiV [Fig. 4.4(b), green inset] [*]. The fundamental two-qubit gate associated with such interaction is a conditional $\pm\pi/2$ rotation of the ^{13}C-spin around the X axis ($R_x^{\pm\pi/2}$), which is a maximally entangling gate. Together with unconditional rotations of the nuclear spin (which are also generated via dynamical decoupling sequences), and MW rotations on the SiV, these sequences form a universal set of gates for the register[146].

We characterize the ^{13}C via Ramsey spectroscopy [Fig. 4.4(c)]. The nuclear spin is initialized and read out via the optically addressable SiV spin by transferring population between the SiV and ^{13}C [Ch. 3]. Depending on the SiV state before the Ramsey sequence, we observe oscillations of the nuclear spin at its eigenfrequencies

---

[*] This is in contrast with the NV center, which is a spin-1 system and therefore features a linear shift of the resonances with coupling strength $A_\parallel$ in the $S = \{0, -1\}$ sub-system.

$\omega_{\uparrow,\downarrow}^2 = \left(\omega_l \pm A_{\parallel}/2\right)^2 + (A_{\perp}/2)^2)$, allowing us to determine the hyperfine parameters $\{\omega_l, A_{\parallel}, A_{\perp}\} = 2\pi\{2.0, 0.70, -0.35\}$MHz. This coherence persists for $T_2^* > 2\,\mathrm{ms}$ [Ch. 3], and can be further extended to $T_2 > 0.2\,\mathrm{s}$ by applying a single dynamical decoupling π-pulse on the nucleus, demonstrating the exceptional memory of the ^{13}C nuclear spin [Fig. 4.4(d)].

We benchmark the two-qubit register by demonstrating an SiV-controlled X-gate (CNOT) on the ^{13}C-spin by combining a $R_x^{\pm\pi/2}$ with an unconditional nuclear $\pi/2$ rotation [Ch. 3]. This gate results in a spin flip of the ^{13}C only if the SiV spin is in the state $|\downarrow\rangle$ [Fig. 4.4(e)]. We use this gate to prepare a Bell state by initializing the register in $|\downarrow\downarrow\rangle$, and applying a $\pi/2$-rotation gate on the SiV spin followed by a CNOT gate. Correlation measurements yield a concurrence of $\mathcal{C} = 0.22(9)$ corresponding to a Bell state fidelity of $F = 0.59(4)$ after correcting for readout errors [Appendix C].

4.5 Conclusion

Our experiments demonstrate the first prototype of a nanophotonic quantum network node combining all necessary ingredients in a single physical system. We emphasize that both spin-photon and spin-spin experiments are performed in the same device under identical conditions (cavity detuning and bias field), thereby providing simultaneous demonstration of all key requirements for a network node.

The main limitation on the demonstrated fidelities are related to the specific ^{13}C in

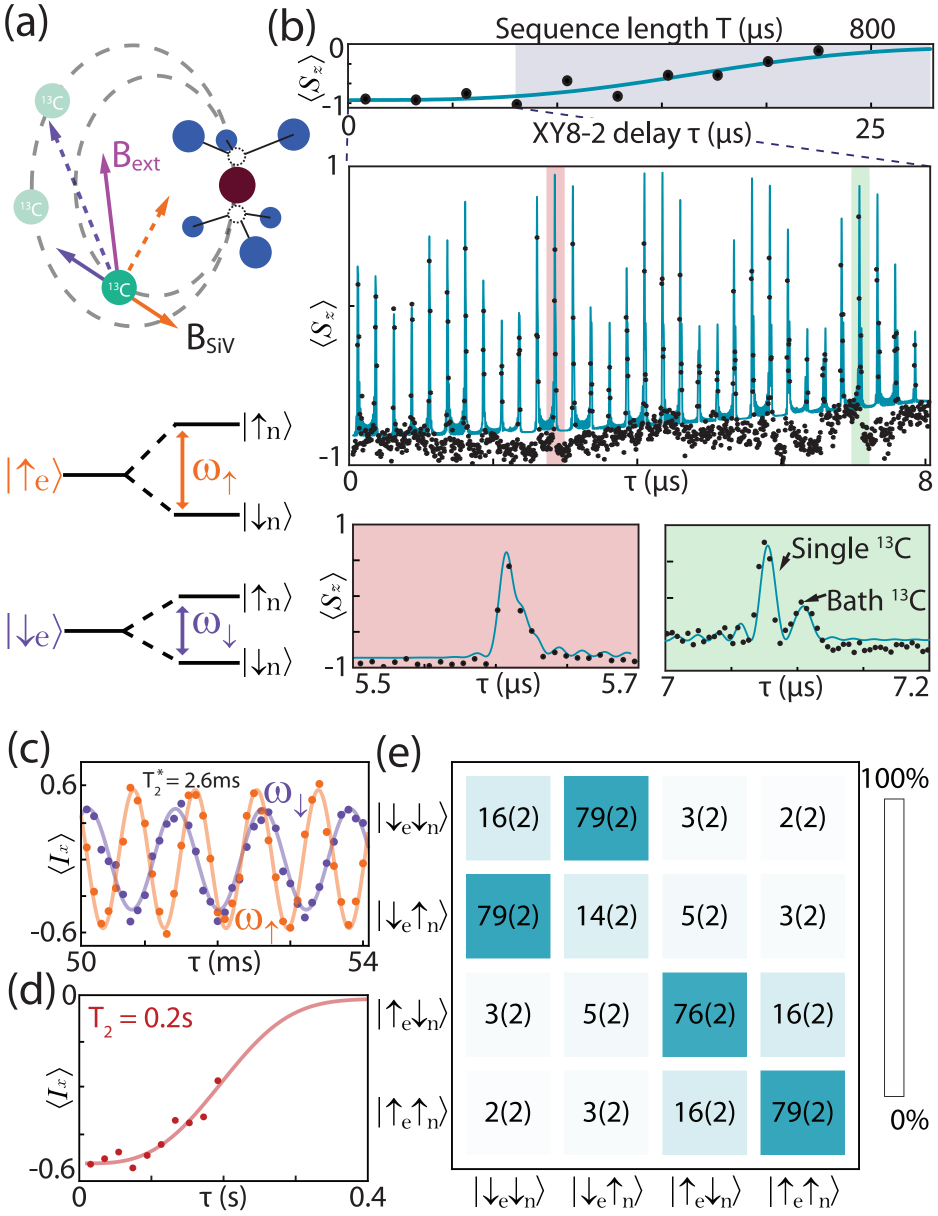

	$\lvert\downarrow_e\downarrow_n\rangle$	$\lvert\downarrow_e\uparrow_n\rangle$	$\lvert\uparrow_e\downarrow_n\rangle$	$\lvert\uparrow_e\uparrow_n\rangle$
$\lvert\downarrow_e\downarrow_n\rangle$	16(2)	79(2)	3(2)	2(2)
$\lvert\downarrow_e\uparrow_n\rangle$	79(2)	14(2)	5(2)	3(2)
$\lvert\uparrow_e\downarrow_n\rangle$	3(2)	5(2)	76(2)	16(2)
$\lvert\uparrow_e\uparrow_n\rangle$	2(2)	3(2)	16(2)	79(2)

Figure 4.4: (a) Schematic of an SiV coupled to nearby ^{13}C nuclear spins. Orange (purple) vectors are conditional fields when the SiV is in state $|\uparrow\rangle$ ($|\downarrow\rangle$). (b) XY8-2 spin-echo. (Top) envelope for spin-echo shows a $T_2(N = 16)$ $=603\,\mathrm{s}$. XY8-2 at early times (Center) exhibits collapses in signal due to interaction with nuclear spins. Single ^{13}C cannot be identified at early times (red inset), but can be separated from the bath at long times (green inset). (c) Ramsey measurement on the ^{13}C nuclear spin. The nuclear spin precesses at a different Larmor frequency depending on whether the SiV is prepared in $|\uparrow\rangle$ (orange) or $|\downarrow\rangle$ (purple). Coherent oscillations persist for $T_2^* > 2\,\mathrm{ms}$ [Ch. 3]. (d) Spin echo on ^{13}C, revealing $T_2 > 0.2\,\mathrm{s}$ (e) Reconstructed amplitudes for a CNOT gate transfer matrix.

the proximity of the SiV, requiring an unfavorable alignment of the external magnetic field in order to isolate a single ^{13}C. Specifically, the fidelity of two-qubit gates is limited by residual coupling to bath nuclei, SiV decoherence during the gate operations, and under/over-rotations of the nuclear spin arising from the granularity of spin-echo sequences. To reduce these errors, fine-tuned adaptive pulse sequences can be used to enhance sensitivity to specific nearby ^{13}C, and tailor the rotation angle and axis of rotation[144,145]. Alternatively, replacing gold with superconducting microwave coplanar waveguides will significantly reduce ohmic heating, and allow direct radio-frequency control of nuclear spins. These improvements could also enable the realization of a deterministic two-qubit register based on ^{29}SiV, which contains both electronic and nuclear spins in a single defect[42].

The fidelity of the heralded photon mapping ($> 90\%$) is competitive with spin-photon correlations achievable in other solid state platforms[155,156], and is limited primarily by imperfect critical coupling of the cavity. The improvements of the nuclear spin control mentioned above would allow for working in an external magnetic field aligned to the SiV axis, which would improve readout fidelity from $F \sim 0.90$ (reported here) to 0.99[41]. The impedance mismatch of the cavity used in this experiment also gives rise to residual reflections which are not entangled with the SiV. By using a critically coupled cavity, we have recently realized memory-enhanced quantum communication based on the techniques demonstrated in the present work[157]. Switching to over-coupled cavities would also enable the use of a SiV spin-dependent phase flip for reflected photons, improving both the fidelity and success probability of spin-photon interactions.

In conjunction with recent advances in controlling emitter inhomogeneity via improved fabrication procedures and electromechanical tuning[158], these techniques should allow for chip-scale fabrication of quantum network nodes, laying the groundwork for the realization of scalable quantum repeater[79,109] architectures. The ability to store quantum information in highly coherent ^{13}C nuclei, as well as the opportunity to extend these results to other group-IV color-centers, may open up the possibility of operating such nodes at at temperatures $> 1\,\mathrm{K}$[31,122,159,160]. Finally, by utilizing on-demand single photon sources, the efficient quantum network node demonstrated in this Letter could enable generation of multi-dimensional cluster states of many photons, which could facilitate realization of novel, ultra-fast one-way quantum communication architectures[161].

5

Conclusion

This thesis builds on the vast body of work on diamond color centers, and focuses on understanding the SiV in the context of a spin-photon interface. Although the specifics of the SiV are fundamentally different than its cousin the NV, studies with this defect have progressed along similar lines, and opened the door for a rich understanding of diamond color centers for quantum technologies.

5.1 Outlook for SiV nanoscale sensing

Chapter 1 identifies one application for SiVs in nanodiamonds, where they can be used as optically controlled thermometers. Unlike other systems for luminescent thermometery (including the NV), the SiV excels due to its bright, homogeneous optical transitions which render it nearly calibration free, with fast readout times, suitable for time-sensitive applications, including intracellular biological processes. Despite these advantages, this application is limited in part due to the SiV's low quantum efficiency (only about 10% of excited state decay is radiative). While this can potentially be overcome by phonon engineering (for example by using small nanodiamonds where relevant phonon modes are suppressed), it could also be solved through the discovery of novel color centers more suitable for this application. Diamond is known to be host to a wide array of color centers, many of which have yet to be carefully investigated[162]. As this work with the SiV shows, an increased understanding and familiarity with these color centers has the potential to uncover new platforms and applications for academic and industrial research. In fact, current understanding of the SiV's favorable symmetry properties has motivated the search for a family of color centers based on group-IV point defects in diamond, all of which appear to have similar symmetry and electronic structure[29,30,31], while also having higher intrinsic quantum efficiency[163]. Naturally, these centers also make for useful nanoscale thermometers[164,165].

Looking forward, we note that SiV thermometry is enabled primarily by the orbital component of the electronic wavefunctions, which are sensitive to both thermal lattice expansion and phonon-induced energy shifts. This naturally suggests other potential sensing schemes with SiVs, including strain. Recently, it has been measured that SiV electronic levels are highly sensitive to strain fluctuations[121,148] [Ch. 3]. This sensitivity might prove useful in its own right as a stress sensor[166], or to motivate research in engineering SiV-SiV phononic coupling[167,168].

5.2 Outlook for SiV quantum networks

Chapters 2-4 represent the main results of this thesis, where we outline our efforts to establish the SiV nanocavity platform as a quantum network node. We demonstrate that this system fulfills all of the necessary criteria for building a quantum network: a small register of interacting qubits with high fidelity gates and long quantum memory times, which feature a deterministic photonic interface. Although there remains much room for improvement with this platform, the current generation of these nodes (as developed in this thesis) are already sufficient for basic applications, such as quantum key distribution[16,169,170].

In essence, quantum key distribution protocols are based on measuring quantum correlations between distributed quantum states, and are secured by the no-cloning theorem[171,172]. This represents a new paradigm of security compared to current security protocols, which are typically backed by classically difficult computations. The rate of successful communication in these schemes scales with the distance between communicating parties due to photon loss. In the case of memory-less implementations (built by shaping weak coherent laser sources or single photon wavepackets using linear optics), photon losses in optical fibers are are fundamentally rate limiting, resulting in an exponential scaling of key distribution rate with distance[173].

While new linear optics protocols are being explored to improve the pre-factors of this scaling[174], networking schemes based on quantum memories promise polynomial communication rates, based on the quantum repeater protocol[79,80]. It turns out, with only slight modifications to the experiments presented in chapter 4, the SiV electron spin can be used to perform asynchronous Bell-state measurements between photonic qubits[157], one implementation of quantum key distribution which provides a rate enhancement compared to other (memory-less) schemes. By adding additional storage qubits (such as the ^{13}C nuclear spin described in 4) and scaling to several nodes, this system is well suited for implementing the full quantum repeater protocol[79,80].

While quantum key distribution is but one of the many proposed applications of quantum networks, it serves as a useful testbed for various experimental control and diagnostic sequences, and can be extended for a variety of applications. For example, the multi-photon gate operations already demonstrated for the SiV platform[157] can be adapted to generate correlations between large clusters of entangled photons[175], which are a resource for fault-tolerant quantum communication[161,176] and one-way quantum computing[177]. Furthermore, by scaling up the number of nodes in the network, this platform has the potential for generating long-lived entanlged states separated by large distances. This entanglement is a valuable resource for non-local metrology[17,18,178] and distributed quantum computing[13].

5.3 Outlook for ongoing experiments

In order to facilitate some of these proposed experiments, it is worth discussing potential technical improvements to the system presented in this thesis. Currently, incorporating additional qubits based on ^{13}C nuclear spins into our platform has the greatest room for improvement. We report [chapter 3] two-qubit entanglement with fidelity $\sim 60\%$, limited by the weak hyperfine coupling to the target ^{13}C, the uncontrolled coupling to additional nearby ^{13}C, and the inability to perform direct driving of the target qubit. Besides this, a second equally concerning issue is that this additional qubit relies on a statistical distribution of ^{13}C in the host diamond lattice, which results in the probabilistic (as opposed to deterministic) realization of useful devices. This, in addition to the rest of the fabrication stack (probabilistic distribution of cavity frequencies, probabilistic nature of ion implantation, and probabilistic strain distribution of SiVs in nanostructures) presents a severe bottleneck to the practical scalability of this platform.

One potential way forward is by switching to a deterministic two-qubit system in diamond, based on silicon nuclear spins. While the work presented above utilizes the ^{28}Si isotope of silicon (a nuclear spin-0 isotope) for its simplicity, there exists a stable ^{29}Si isotope which is nuclear spin-1/2. The strong contact interaction between the SiV electron spin and the ^{29}Si nuclear spin in this system ($\sim$30 MHz[42]) could enable fast single- and two-qubit gates for this system, without infidelities arising from coupling to a nearly-resonant bath. While this cannot be naturally scaled to many qubits, it could be used to augment the ^{13}C register presented in this thesis to increase the yield of many-qubit devices, or to facilitate entangling many SiV-cavity nodes by creating deterministic storage/communication qubit pairs within many nanophotonic cavities.

Improving the fidelity and efficiency of spin-photon gates represents another area with great potential for improvement. Current limits in this system are primarily due to the impedance mismatch between the cavity and waveguide regions of target devices, which gives rise to a residual reflection signal not correlated with SiV spin state. Although tuning this mismatch to be more critically coupled would in principle solve this problem, it is perhaps more promising to consider working with strongly over-coupled cavities, where all light entering the device is reflected, independent of spin state. With such a system, interactions with the SiV would result in a spin-dependent phase flip in reflected photons, which could be measured interferometrically, potentially improving both fidelity and efficiency of entanglement protocol.

Finally, there are a number of intrinsic challenges in an SiV-based system, (as briefly discussed in section 5.1) such as strain-induced spectral inhomogeneity, quantum efficiency, phonon-limited spin T_1, and optical transition frequency. The optical transition frequency of SiVs, while fairly well suited for biological sensing applications, is not particularly compatible with long-range quantum networks. Losses in optical fibers vary dramatically with wavelength, and these losses are orders of magnitude worse for photons at 740 nm compared to typical telecom photons. Thus, one necessary development for this platform will be frequency conversion, as has been demonstrated already for NVs[179].

Similarly, spectral inhomogeneity limits the scalability of building quantum networks, as it is unlikely for several SiVs to all be optically resonant with each other. While this can in principle be addressed by the same frequency conversion described above, this process is lossy, and (especially for local networks) it would be useful to have a mechanism by which to tune several SiVs onto resonance with each other. Several schemes have already been proposed and demonstrated for this, including Raman-tuning of SiV emission[40] and strain tuning of SiV resonances via electromechanics[148]. As described in chapter 3, heating by both optical and microwave control fields locally heats the SiV and activates thermal phonons at the ground state splitting frequency and reduces coherence times. Strain tuning once again can mitigate this process by increasing the relevant energy scales for phonon relaxation[121,148].

Finally, the intrinsic quantum efficiency of the SiV (as described in section 5.1) limits the total cooperativity of the SiV-cavity system, and thus limits the maximum theoretical fidelity of the spin-photon interface. Although it is conceivable to engineer more complicated opto-acoustic cavities which suppress unwanted photonic and phononic decay channels[44], this represents a challenging fabrication effort.

Conversely, many of these challenges could be addressed by choosing alternative color centers to the SiV. Although a number of diamond electronic transitions have been observed in the telecom band[162], to the best of our knowledge, no careful study has been done investigating their prospects for quantum applications. Despite this, the wealth of research on known quantum emitters suggests that this search could prove fruitful. For example, studies with heavier group-IV vacancy centers have revealed similar electronic structure and symmetry, featuring larger intrinsic ground-state orbital splitting and higher quantum efficiency as compared to the SiV[29,30,31,163]. This larger ground-state splitting gives an enhanced protection to thermal phonon decoherence, suggesting that these systems might have long coherence times at more accessible temperatures (i.e. without requiring an expensive dilution fridge)[180]. Alternatively, finding an inversion-symmetric orbital-singlet defect might allow for a system with the superior optical properties of the SiV, combined with the superior coherence properties of the NV. In fact, preliminary studies with the SiV^0 charge state (as compared to the more conventional SiV^- studied in this work) is proposed to be exactly such a system[72,92].

Current efforts in the development of quantum technologies have been focused on engineering existing, well established quantum systems to try and tackle known problems. In light of the rapid development in diamond and related solid state platforms over recent years, there is a strong motivation taking an alternative approach based on a systematic experimental and theoretical effort investigating new color centers in the context of specific applications, selecting the particular quantum system best suited for the task.

A

Supplementary information for chapter 1

A.1 Bulk CVD diamond growth

In order to achieve a high density of SiVs in a diamond chip, we overgrow a Type IIa diamond using plasma-enhanced chemical vapor deposition (PECVD) in a Seki Technotron AX5010-INT PECVD reactor. A Si wafer is placed in the plasma, where it is etched and incorporated into the overgrown layer. The growth conditions for this layer are microwave power: 950 W, chamber pressure: 60 Torr, gas flow: 300 sccm 1:99 $CH_4 : H_2$ for 20 minutes[181]. After growth, 1 m tall islands can be found on the edges of the seed diamond, each of which has a high SiV density.

A.2 SiV nanodiamond growth

To grow nanodiamonds, we use high-pressure high-temperature synthesis with luminescent SiV and NV centers based on homogeneous mixtures of naphthalene, fluorinated graphite ($CF_{1.1}$), and tetrakis(trimethylsilyl)silane without catalyst metals. Cold-pressed pellets of the initial mixture (5 mm diameter and 3 mm height) are inserted into a graphite container and then placed into a high-pressure cell. High-pressure high-temperature treatment of the samples is performed with the use of a high pressure apparatus of the “Toroid” type. Details of the experimental procedure are described in the preliminary report[182]. The obtained diamond products are then isolated by quenching to room temperature under pressure.

Separation of nano-size ($\sim$15-400 nm) diamonds was carried out in several stages that consisted of ultrasonic dispersing of the diamond particles using UP200Ht dispersant (Hielscher Ultrasonic Technology), chemical treatment of the samples in a 40% solution of hydrogen peroxide, and subsequent centrifugation of aqueous or alcohol dispersion of diamond powders. The diamonds used in this work were measured to have a size distribution of 200(70) nm using a DelsaNano C particle analyzer.

A.3 PL thermometry setup

In order to measure temperature, the diamond is mounted onto an external heater and excited off resonance with 700 nm and 520 nm light (10 mW and 5 mW respectively) using a home-built confocal microscope. SiV fluorescence is filtered around the ZPL (Semrock FF01-740/13) and directed to either an APD or a spectrometer (Horiba iHR550 + Synapse CCD, 1800gr, 0.025 nm resolution). Based on fluorescence counts on an APD (10 MHz), we expect to be addressing $\sim$100 SiVs. Interference effects on the collection arm induce a fluctuating spectral signal modulating our spectrum. To correct for this, we measure the transfer function of a blackbody source traveling through the same optical path and subtract it from the measured signal. Fitting a preliminary spectrum to a lorentzian at some fixed temperature and using the fit residuals to find the transfer function agrees to within 10%. This method has the added benefit of not requiring a separate calibration step, as the first spectrum in a given measurement can be used for calibration.

A.4 PLE fitting procedure

Afterward, we fit each spectrum to a Lorentzian using an affine-invariant Markov-Chain Monte-Carlo estimator[69,70] and extract the ZPL peak position, peak width, and peak intensity, as well as estimated contributions to the noise from both photon shot noise and CCD readout noise[183]. While the fit parameters achieved with this technique are almost identical to those acquired using a more naive least-squares fit, this technique is able to give a more convincing estimate for the uncertainties in the fit parameters and agrees with systematic errors extracted via repetitive measurement. As mentioned in the main text, the ZPL peak position sensitivity to temperature is $0.0124(2)\mathrm{nm\,K^{-1}}$ with an uncertainty of $337\,\mathrm{mK}/\sqrt{\mathrm{Hz}}$. In comparison, the ZPL linewidth broadens by $0.030(1)\mathrm{nm\,K^{-1}}$ with an unceratinty of $636.7\,\mathrm{mK}/\sqrt{\mathrm{Hz}}$, and the integrated ZPL intensity does not have a statistically significant sensitivity to temperature. Local strain in the diamond causes different SiV sub-ensembles to have different intrinsic ZPL peak positions and widths corresponding to an offset of ±2 K at room temperature. Despite this, the sensitivity to temperature varies by only ±3%, meaning there is no need for calibration in order to measure relative temperature changes.

A.5 PLE thermometry calibration

To calibrate the PLE thermometer, we first measure how the ZPL peak position varies as a function of applied laser power using PL thermometry ($\Delta\lambda/\Delta P_h$). Dividing the temperature sensitivity of the peak position measured in bulk diamond ($\Delta\lambda/\Delta T$) by this quantity gives the laser induced temperature change as a function of laser power ($\Delta P_h/\Delta T$). Finally, we measure the intensity contrast as a function of laser power ($\frac{\Delta I}{I_0}/\Delta P_h$), which is converted to the temperature sensitivity of the intensity signal $\frac{\Delta I}{I_0}/\Delta T = 1.3(1)\%/\mathrm{K}$.

B

Supplementary information for chapter 2

B.1 Dilution refrigerator setup

We use a BlueFors BF-LD250 cryogen-free dilution refrigerator (DR) modified to obtain free-space optical access [Fig. B.1]. For optical excitation and collection, we use a home-built confocal microscope. We excite SiVs with off-resonant 520 nm light and resonant $\sim 737\,\mathrm{nm}$ light combined on a dichroic mirror (DM). SiV fluorescence in the phonon side-band (PSB) is collected using a 90:10 non-polarizing beam-splitter cube (BSC), coupled to a multi-mode (MM) fiber, and sent to a single-photon detector (APD). For spectral filtering, we use a short-pass filter (SP) in the excitation arm and band-pass filters (BP) in the collection arm. The optics used to deliver light into and to collect light from the DR are mounted on a breadboard (Thorlabs PBG12102) on top of the frame supporting the DR. This allows for DR venting and sample exchange without realignment of the optics.

A collimated laser beam enters at the top of the DR through a vacuum viewport ① using the central line-of-sight port. The optical beam is focused on the diamond sample ⑫ by a low-temperature compatible objective ④. To reduce the heat load due to black-body radiation at the mixing chamber plate (MXC), 10 mm apertures② are installed at each stage inside the DR. In this configuration, the base temperature at the MXC is 20 mK. We do not use any cold windows along the optical path inside the DR.

A 6-1-1 T cryogen-free superconducting vector magnet ⑭ is mounted below the MXC and thermally linked to the 4 K plate of the DR. The diamond sample ⑫ is soldered with indium to a fixed copper sample holder ⑬ and placed inside the magnet bore on a science plate ⑪. We operate this magnet in a persistent mode to reduce SiV spin dephasing due to fluctuations of applied magnetic fields.

A vented cryo-compatible objective ④ is mounted on 3-axis piezo steppers ⑧, ⑩,

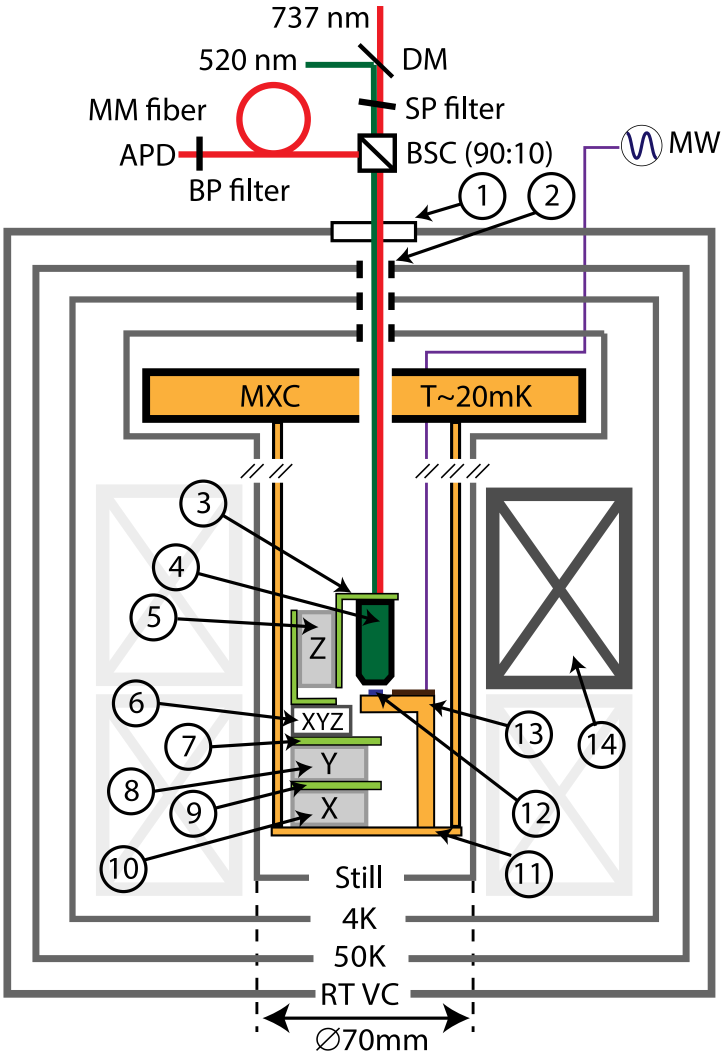

Figure B.1: Schematic of a dilution refrigerator with free-space optical access. MXC: Mixing chamber plate; Still: Still plate; 4K: 4K plate; 50K: 50K plate; RT VC: Outer vacuum can; SP: 758-nm short-pass filter (Semrock FF01-758/SP-25), tilted by a small angle to tune the cut-off frequency; BP: Band-pass filters (Semrock FF01-775/46-25 and FF01-785/62-25); MM: 25 um-core MM fiber; DM: dicroic mirror (Semrock Di03-R561-t1-25x36); APD: Single-photon counting module; BSC: Non-polarizing beam-splitter cube with T:R = 90:10; ① vacuum viewport; ② $10\,\mathrm{mm}$ apertures at $50\,\mathrm{K}$, $4\,\mathrm{K}$ and Still plates of the DR; ③ Objective L-bracket ④ Low-temperature, vacuum compatible objective (Attocube LT-APO-VISIR) with NA = 0.82; ⑤ Attocube stepper (ANPx311) which moves the objective vertically; ⑥ Three-axis Attocube scanner (ANSxyz100); ⑦, ⑨ Thermalization plates, each braided to ⑪; ⑧, ⑩ 2 Attocube steppers ANPx311 which position the sample laterally; ⑪ A science plate positioned inside a vector magnet ⑭ and thermally anchored to the MXC; ⑫ Diamond sample; ⑬ Sample holder; ⑭ Cryogen-Free MAxes 6-1-1 T superconducting vector magnet with persistent switches (American Magnetics Inc.).

⑤ and 3-axis piezo scanners ⑥ via L-brackets ③. X-Y steppers ⑧, ⑩ are mounted on the science plate ⑪ which is connected to the MXC via two copper rods (not shown). The diamond sample holder ⑬ and the science plate ⑪ are thermally anchored to the MXC via oxygen-free copper braids (Copper Braid Products). Thermalization plates ⑦, ⑨ and the objective L-bracket ③ are thermally anchored to the science plate via copper braids ⑪. Microwave (MW) pulses are delivered to the diamond sample via coaxial lines (semi-rigid 2.19 mm SCuNi-CuNi lines between room temperature and 4 K, superconducting 0.86 mm NbTi-NbTi lines between 4 K and MXC) which are thermalized at each stage. A temperature sensor (Lake Shore Cryotronics, RX-102B-CB) is placed on the sample holder ⑬ and measures a sample temperature of ≤ 100 mK in the absence of microwave driving.

We fabricate a shorted coplanar waveguide (CPW) on the diamond surface to efficiently deliver MW pulses [Fig. B.2(a,b)]. To fabricate the CPW, we first deposit 50 nm of Ti and 600 nm of Au onto the diamond surface using thermal evaporation. Next, a photolithography mask is patterned on the surface, and the unmasked Au and Ti are selectively etched away using Transene Gold Etchant Type TFA diluted 2:1 with water for 120 s, then 5.6% HF by weight (49% HF diluted 9:1 with water) for 30 s.

We adjust focus with stepper ⑤ and use steppers ⑧, ⑩ for coarse positioning. We take confocal images of the diamond sample by moving the objective using piezo scanners ⑥. Optical resolution of the microscope is ≈ 3 m [Fig. B.2(c)] and is limited by

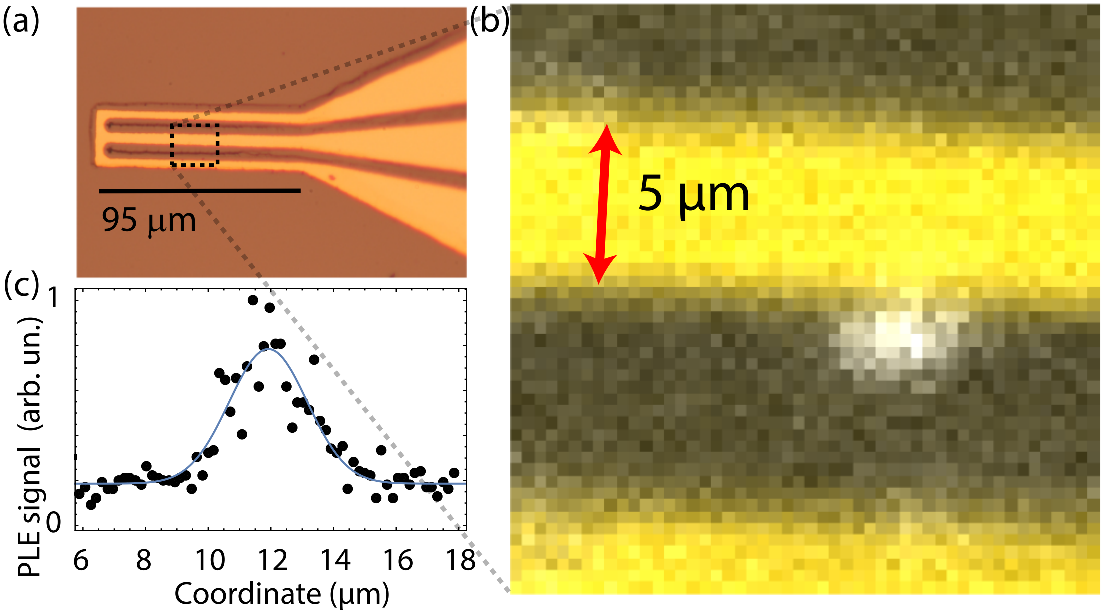

Figure B.2: (a) Room temperature micrograph of the shorted gold coplanar waveguides fabricated on the diamond surface. (b) Low temperature false color reflection image of the diamond surface (black) and the coplanar waveguide (gold), overlaid with the PLE image of an SiV (white). (c) Cross-section of the SiV PLE image. The optical resolution is 3 m.

residual mechanical noise from a pulse tube and the collection pinhole diameter (25 m) set by the MM fiber.

B.2 3-level saturation measurements

In Figure 2.1(d), we compare the PSB counts during resonant excitation of transitions C and D (PLE spectroscopy). Laser driving can affect steady-state population of the UB or the LB via optically pumping to the opposite branch [Fig. B.3(a)]. This effect is minimized when laser power is below the three-level saturation intensity set by the

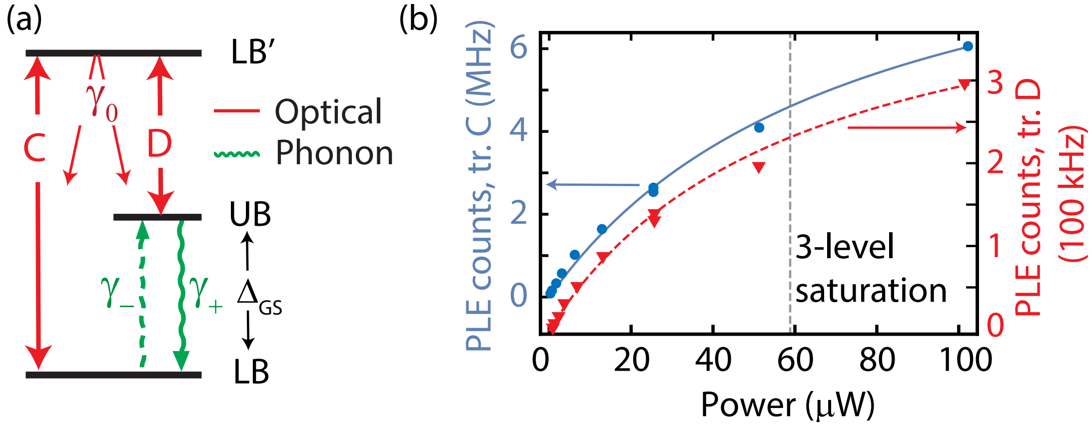

Figure B.3: Three-level saturation in PLE measurements. (a) Relaxation rates in the three-level system formed by the LB and the UB of the SiV ground state and the first excited state (LB′). γ_0 is the total decay rate from the excited state; $\gamma_+(\gamma_-)$ is the upward (downward) phonon relaxation rate. (b) Saturation measurement of the PLE intensity. Blue data is displaced vertically for clarity. Vertical dashed line represents the laser power at 3-level saturation. Power is measured before entering the DR.

decay rate of the excited state (γ_0) and the phonon relaxation rates ($\gamma_\uparrow$ and $\gamma_\downarrow$). By solving master equations for the corresponding 3-level system, we find that at temperatures $T < 1\,\mathrm{K}$, for which the thermal population of phonon modes at the frequency Δ_{GS} is $n(T, \Delta_{\mathrm{GS}}) \to 0$, the saturation intensity is $\propto \gamma_\downarrow/\gamma_0$. The downward phonon relaxation rate is $\gamma_\downarrow \propto (n(T, \Delta_{\mathrm{GS}}) + 1)$[44] and does not depend on T in this regime. Thus, saturation intensity is also constant for $T < 1\,\mathrm{K}$.

In Figure B.3(b), we measure PLE counts for transitions C and D at different laser powers at the fixed $T = 0.75\,\mathrm{K}$. For both transitions, saturation corresponds to a laser power of $\sim 60\,\mu\mathrm{W}$. Since at $T = 0.75\,\mathrm{K}$, $n < 0.1$, saturation intensity does not change at lower T and can only increase at higher temperatures due to faster phonon relaxation.

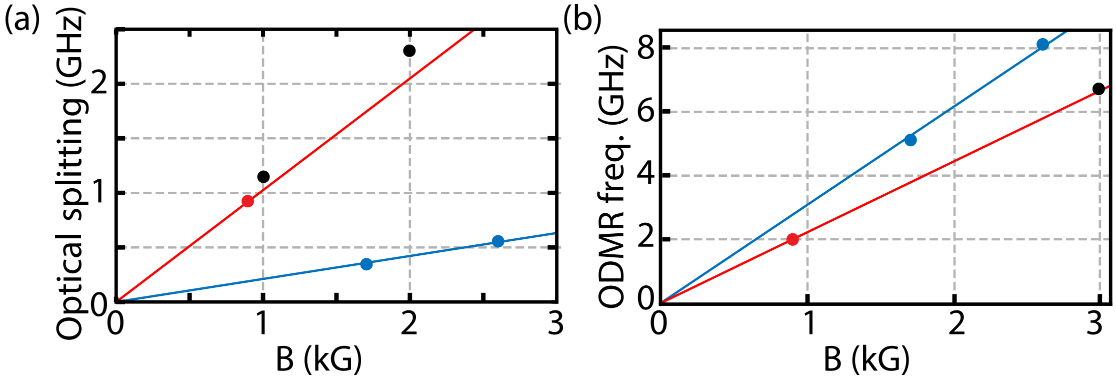

Figure B.4: (a) Splitting of spin-selective transitions in a magnetic field and (b) ODMR frequency. Red data: Orthogonal field for SiV with $\Delta_{\mathrm{GS}} = 75\,\mathrm{GHz}$ in Sample-12; Blue: the same SiV in an aligned field. Black: SiV with $\Delta_{\mathrm{GS}} = 85\,\mathrm{GHz}$ in Sample-13 in an orthogonal field. Solid lines are linear fits.

In Figure 2.1(d), we use a laser power of 0.5 W and thus work deep below 3-level saturation for the whole temperature range. In this case, the ratio of PLE counts is proportional to the ratio of the thermal populations of the LB and the UB of the SiV ground state as stated in Chapter 2.

B.3 Magnetic field alignment for single-shot spin readout

The cyclicity of the spin-conserving transitions depends on the angle between the SiV symmetry axis and applied magnetic field $\vec{B}$[38]. In this section, we describe our procedure to align the magnetic field to the SiV symmetry axis with 0.1 precision. The SiV symmetry axis can be pointed along four possible $\langle 111 \rangle$ orientations in the diamond

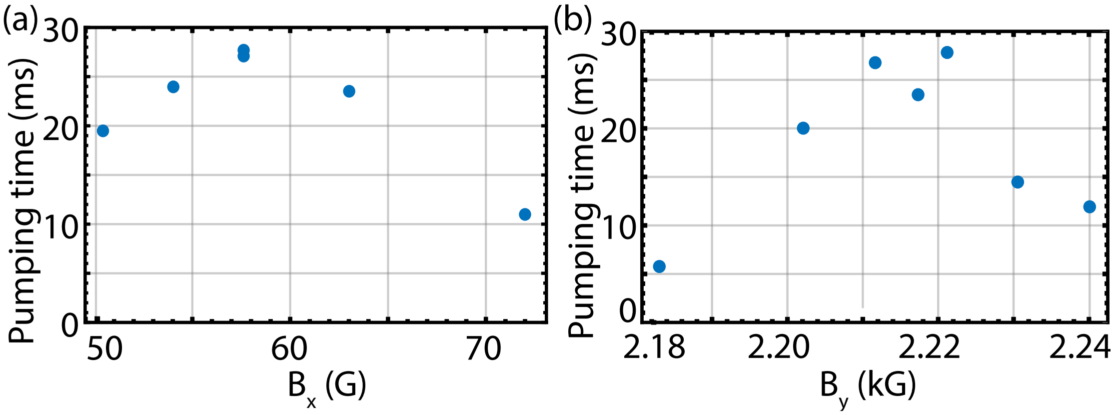

Figure B.5: Magnetic field alignment (a) Optical pumping times at different B_x at $\{B_y = 2.2\,\mathrm{kG},\ B_z = 1.5\,\mathrm{kG}\}$. (b) Optical pumping times at different B_y at $\{B_x = 63\,\mathrm{G},\ B_z = 1.5\,\mathrm{kG}\}$

lattice. Based on the Hamiltonian in Ref.[37], the Zeeman splittings of the ground states and excited states depend on both the orientation of the magnetic field and the amount of strain in the crystal. For strained emitters with $50\,\mathrm{GHz} < \Delta_{\mathrm{GS}} < 100\,\mathrm{GHz}$, off-axis magnetic fields lead to a larger Zeeman splitting in the ground states compared with the excited states. Magnetic fields along the symmetry axis however, result in a comparable Zeeman splitting in ground and excited states. As shown in Figure B.4(a), this leads to a larger frequency splitting between spin-conserving transitions for misaligned fields. We use this approach to determine the orientation group of an SiV center.

For a given SiV, we apply a magnetic field along all 4 possible SiV orientations $\langle 111 \rangle$. Based on the discussion above, the smallest optical splitting corresponds to the magnetic field pointed along the SiV axis. Experimentally, this procedure gives a pointing error of few degrees.

Finally, we fine tune the orientation of the magnetic field by probing SiV spin dynamics. Figure B.5 shows measured optical spin pumping times at different field orientations. These measurements indicate that the spin dynamics are very sensitive to the magnetic field orientation and a precision of ~ 0.1 is required to scatter photons for 30 ms without a spin flip.

B.4 Scattering rates and collection efficiency

For measurements in Figure 2.3(e) in the Main Text, power of the readout laser is set at a 3-level saturation [Section B.2]. This maximizes the number of scattered photons and minimizes off-resonant excitation of the other spin-conserving transition. In this case, the lifetime of the metastable UB $\tau = \gamma_{\downarrow}^{-1}$ limits the photon absorption rate to $R \sim 1/\tau$. For an unstrained emitter ($\Delta_{\mathrm{GS}} \approx 45\,\mathrm{GHz}$), $\tau \sim 200\,\mathrm{ns}$ at 100 mK citejahnke2015electron. Since the phonon emission probability is proportional to $(\Delta_{\mathrm{GS}})^3$, the absorption rate for a strained SiV is $R \sim \frac{1}{200\,\mathrm{ns}} \cdot \left(\frac{\Delta_{\mathrm{GS}}[\mathrm{GHz}]}{45\,\mathrm{GHz}}\right)^3$. During a 20 ms readout window, the SiV in Fig. 3(e) should absorb $\sim 2 \times 10^5$ photons. In the same readout window we detect ~ 10 photons. Thus, the overall system efficiency is $\sim 2 \times 10^{-4}$. This assumes a $\sim 10\%$ quantum efficiency for the SiV[40] optical transition and a $\sim 30\%$ fraction of the PSB (Debye-Waller Factor) in the total emission spectrum.

We can also estimate the collection efficiency in a different way. At 3-level saturation, the steady-state PLE count rate is also limited by $1/\tau \approx 5 \times 10^6$ Hz. In our experiment, the typical steady-state PLE count rate are 1 kHz. This gives $\sim 2 \times 10^{-4}$ for the overall system efficiency which agrees with the previous estimate.

B.5 Optical spin initialization and readout

To initialize the SiV qubit, in state $|{\uparrow}\rangle$ for example, we drive the spin-resolved transition $|{\downarrow}\rangle \rightarrow |{\downarrow}'\rangle$. Optical pumping [Fig. 2.2(a)] eventually brings the qubit into state $|{\uparrow}\rangle$. For higher initialization fidelity, the initialization laser pulse was several times longer than the characteristic time t_p for optical pumping [Fig. 2.2(d)].

We optically readout the qubit states by driving the corresponding spin-conserving transition. For better readout signal-to-noise, we keep the duration of the readout pulse to less than the optical pumping time t_p. Intensities of both initialization and readout pulses were at 3-level saturation [Sec. B.2].

B.6 Spin lifetime measurement

We measure a lower bound for the spin lifetime (T_1) of the SiV spin qubit in a magnetic field of 1.1 kHz aligned along the SiV symmetry axis within a few degrees. Pulse sequence for the T_1 measurement is illustrated in figure B.6. First, a 3 ms long laser pulse at frequency $f_{\downarrow\downarrow'}$ initializes the qubit in state $|{\uparrow}\rangle$. Next, a readout laser at fre-

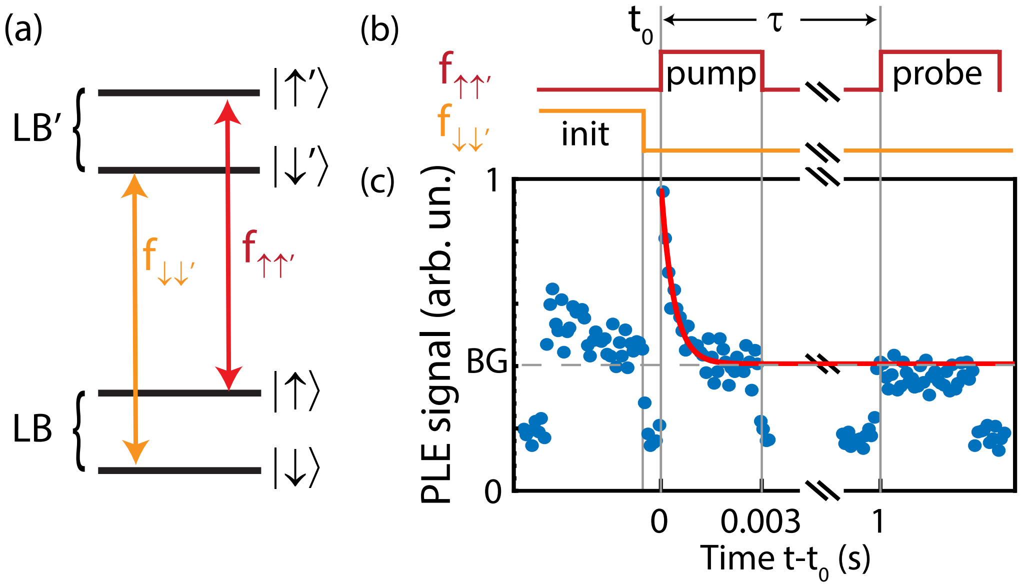

Figure B.6: SiV spin T_1 measurement. (a) Simplified SiV elecronic level structure. $f_{\downarrow\downarrow'}$ and $f_{\uparrow\uparrow'}$ are frequencies of spin-conserving transitions. (b) Pulse sequence for spin T_1 measurement (see text) (c) Time-resolved PLE signal for a sequence in (b). BG denotes a level of background fluorescence.

quency $f_{\uparrow\uparrow'}$ probes the population in state $|\uparrow\rangle$ at time t_0 and pumps the qubit into state $|\downarrow\rangle$. After a delay τ, we probe the population in state $|\uparrow\rangle$ again. The remaining spin polarization depends on the T_1 time. The corresponding pulse sequence is shown in figure B.6(b).

We measure the absence of any fluorescence signal above the background level (BG) after a delay of $\tau = 1\,\mathrm{s}$ [Fig. B.6(c)]. This indicates an almost perfect spin polarization after 1 s and means that the SiV spin T_1 is much greater than 1 s.

B.7 Microwave driving

We use the SiV states $\left|\uparrow\right\rangle$ and $\left|\downarrow\right\rangle$ as a spin qubit. In a small aligned magnetic field B ($\mu_\mathrm{B} B \ll h\lambda_\mathrm{SO}$), these states are of the form[37]

$$\begin{aligned}
\left|\uparrow\right\rangle &= \left|\uparrow\right\rangle_\mathrm{spin} \otimes \left(\left|e_-\right\rangle + \frac{1-\sqrt{1+\xi^2}}{\xi}\left|e_+\right\rangle\right)\\
\left|\downarrow\right\rangle &= \left|\downarrow\right\rangle_\mathrm{spin} \otimes \left(\left|e_+\right\rangle + \frac{1-\sqrt{1+\xi^2}}{\xi}\left|e_-\right\rangle\right)\\
\xi &= \frac{\alpha}{\lambda_\mathrm{SO}},
\end{aligned}$$

where α is an off-diagonal (E_g) strain[103], $\lambda_\mathrm{SO} \approx 46\,\mathrm{GHz}$ is the spin-orbit coupling in the ground manifold of the SiV $\left(\Delta_\mathrm{GS} = \sqrt{\alpha^2 + \lambda_\mathrm{SO}^2}\right)$; $\left|\uparrow\right\rangle_\mathrm{spin}, \left|\downarrow\right\rangle_\mathrm{spin}$ are spin states; and $\left|e_+\right\rangle, \left|e_-\right\rangle$ are orthogonal electronic orbital states.

To coherently manipulate the SiV spin qubit, we drive the transition $\left|\uparrow\right\rangle \to \left|\downarrow\right\rangle$ with resonant MW pulses. The Rabi frequency is $\Omega_\mathrm{MW} \sim \sqrt{P_\mathrm{MW}} \cdot \frac{1-\sqrt{1+\xi^2}}{\xi}$, where P_MW is the MW power. We verify a square-root dependence of Ω_MW on the MW power [Fig. B.7.

In the low strain regime ($\alpha \ll \lambda_\mathrm{SO}$), the qubit magnetic dipole transition $\left|\downarrow\right\rangle \to \left|\uparrow\right\rangle$ is only weakly allowed. This makes a coherent control of the spin with the MW driving difficult due to heating of the sample via ohmic losses in the gold stripline.

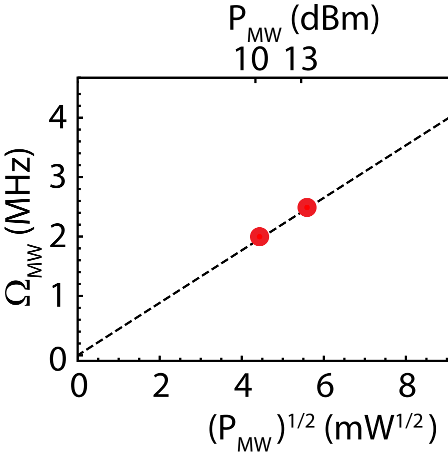

Figure B.7: Frequency of MW Rabi oscillations (Ω_{MW}) at different MW powers (P_{MW}) delivered to the dilution fridge. The power at the sample is reduced by an estimated $\sim 5\,\mathrm{dB}$ due to losses in the coaxial lines. The dashed line is a linear fit. Data are taken at $f_{\downarrow\uparrow} = 6.6\,\mathrm{GHz}$

In this work, we use SiV centers with $\Delta_{\mathrm{GS}} \approx 80\,\mathrm{GHz}$. This corresponds to a moderate crystal strain of $\alpha \approx 1.5\lambda_{\mathrm{SO}}$ allowing the qubit transition and reducing the necessary amount of MW power. This facilitates maintaining a steady-state sample temperature of $\sim 100\,\mathrm{mK}$.

B.8 T_2^* limiting processes and pulse errors

The measurements in figure 2.3 demonstrate that T_2^* scales approximately inversely with the static magnetic field in the isotopically purified sample (Sample-12). In this section, we discuss a microscopic mechanism that can lead to the observed $(T_2^*)^{-1} \propto g\mu_B B$ dependence. As discussed in Sec. B.7 and Ref.[37], the wavefunction of the spin qubit consists of both an electronic orbital and a spin degree of freedom that each contribute to the electronic Landé g-factor.

The electronic orbitals $|e_-\rangle$ and $|e_+\rangle$ can be mixed via strain and large electric fields. The mixing mechanism via strain is described in Sec. B.7. While electric fields cannot mix the two orbitals $|e_-\rangle$ and $|e_+\rangle$ that have the same parity to first order, second-order processes (mediated by the excited states of the opposite parity) can result in a mixing between the two orbitals. The presence of such electric or strain field fluctuations can therefore lead to fluctuation of the orbital wavefunctions and a corresponding change in the g-factor of the qubit states. This can cause spin dephasing at a rate proportional to an applied magnetic field B.

The resulting T_2^* also limits the single qubit gate fidelities. We operate with MW Rabi frequencies Ω_{MW} in the range from 1 to 10 MHz. In this case, MW π-times of $\sim 100\,\mathrm{ns}$ are comparable with T_2^* resulting in imperfect MW π-pulses with errors at the percent level. For CP sequences involving 32 rephasing π-pulses [Fig. 2.4(b)], this results in a reduction of the state fidelity to $\sim 70\%$. In our experiments, stronger MW driving (corresponding to larger Ω_{MW}) causes heating of the sample due to Ohmic losses in a gold coplanar waveguide which destroys spin coherence [Fig. 2.4(d)]. By using low-loss superconducting coplanar waveguide[101] for MW delivering, larger Ω_{MW} can be achieved without additional heat load.

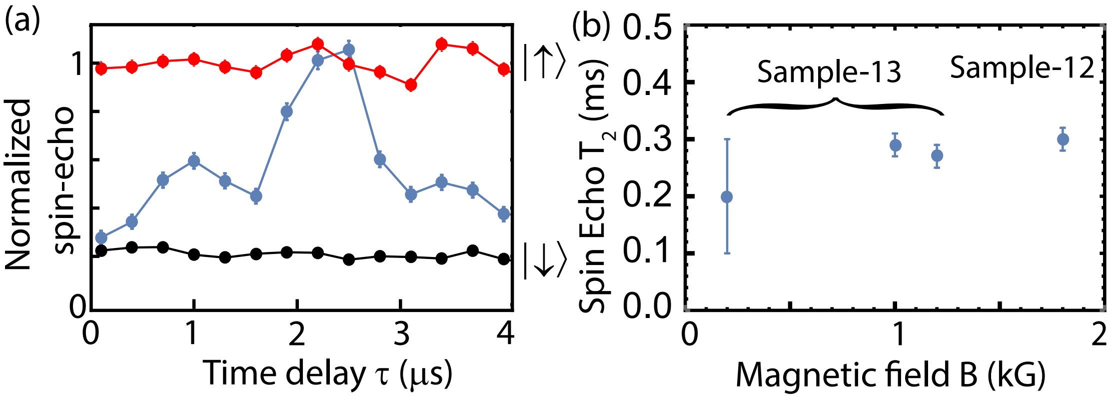

Figure B.8: Spin echo at different magnetic fields. (a) Spin-echo curves for $\tau < 4\,\mathrm{s}$. Blue data: Spin echo at $B = 0.2\,\mathrm{kG}$; Black data: Spin echo at $B = 3\,\mathrm{kG}$; Red data: Spin echo at $B = 3\,\mathrm{kG}$, the second $\pi/2$ pulse is replaced by $3\pi/2$. (b) Spin-echo (T_2) times at different magnetic fields.

B.9 Coupling to nuclear spins

The effect of a ^{13}C nuclear spin on a spin-echo signal depends on the ratio of the external magnetic field and the magnetic field produced by an SiV at the nuclear site (Knight shift)[95]. In a large external magnetic field of 3 kG, this Knight shift is negligible and we do not observe any effect of nuclear spins in the spin-echo measurements [black data in Fig. B.8(a)]. We repeated this measurement with a spin-echo sequence modified such that the second $\pi/2$ pulse was replaced by a $3\pi/2$ pulse (red data). This allows us to normalize the readout signal. The mean value of the spin-echo (modified spin-echo) signal at $\tau \ll T_2$ corresponds to finding the SiV spin in state $|\downarrow\rangle$ ($|\uparrow\rangle$).

In contrast, repeating these measurements in a low magnetic field of 0.2 kG yields high-visibility oscillations of the SiV spin coherence [blue data in Fig. B.8(a)] suggesting a coherent coupling to several ^{13}C nuclear spins in Sample-13.

Coherent coupling to nuclear spins does not affect the T_2 time as measured by the spin-echo envelope [Fig. B.8(b)]. We observe the same T_2 times for Sample-13 in magnetic fields from 0.2 to 1 kG and for Sample-12 in a 2 kG magnetic field. This suggests that coupling to nuclear spins is not the main factor which limits the SiV spin T_2 time.

B.10 Spin coherence analysis

For each curve in figure 2.4(b), the measured background was subtracted from the signal and the result was normalized such that the steady state value is equal to 1/2, corresponding to an equal mixture between the qubit levels; no additional rescaling was implemented.

The observed scaling of the coherence time T_2 with number N of rephasing pulses [Fig. 2.4(c)] is close to linear: $T_2 \propto N^{\beta}$, where $\beta = 1.02 \pm 0.05$. This scaling contradicts dephasing due to a pure Lorentzian noise power spectrum which gives $T_2 \sim N^{2/3}$[99,100].

Different noise bath models can produce similar T_2 scaling but lead to different shapes of the CP curves. Fig. B.9 shows the CP8 curve [from Fig. 2.4(b)] fit using different stretched exponentials $\exp\left[-\left({}^{T}/{}_{T_0}\right)^{n}\right]$. To fit the data shown in figure 2.4(b),

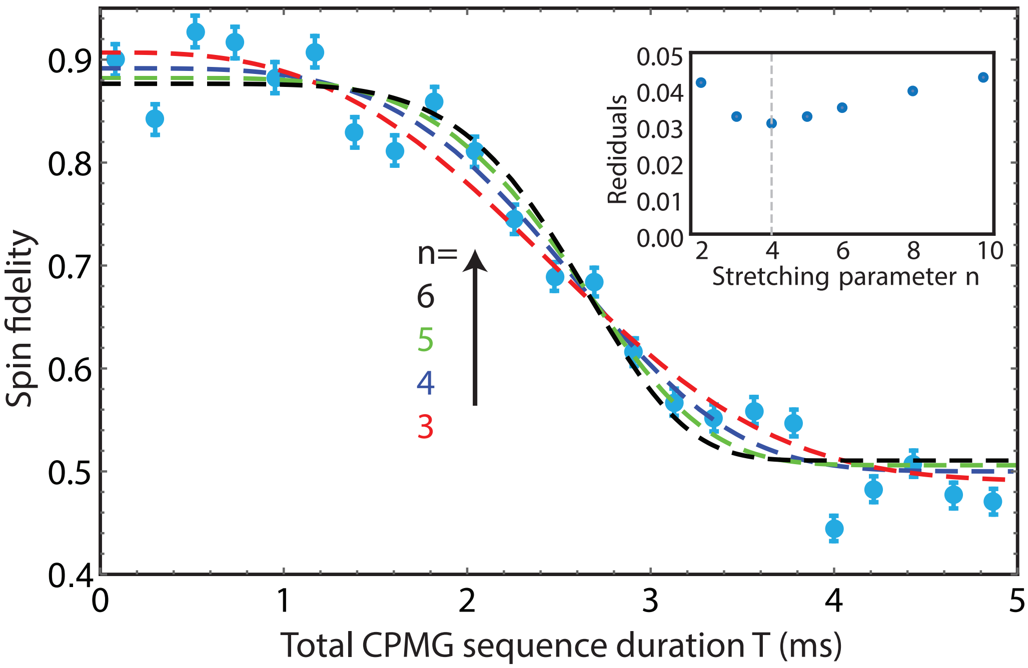

Figure B.9: Experimental CP curve with $N = 8$ (blue points) fitted by stretched exponentials with $n = 3, 4, 5, 6$. Inset: fit residuals for stretched exponentials with $n = 2, 3, 4, 5, 6, 8, 10$.

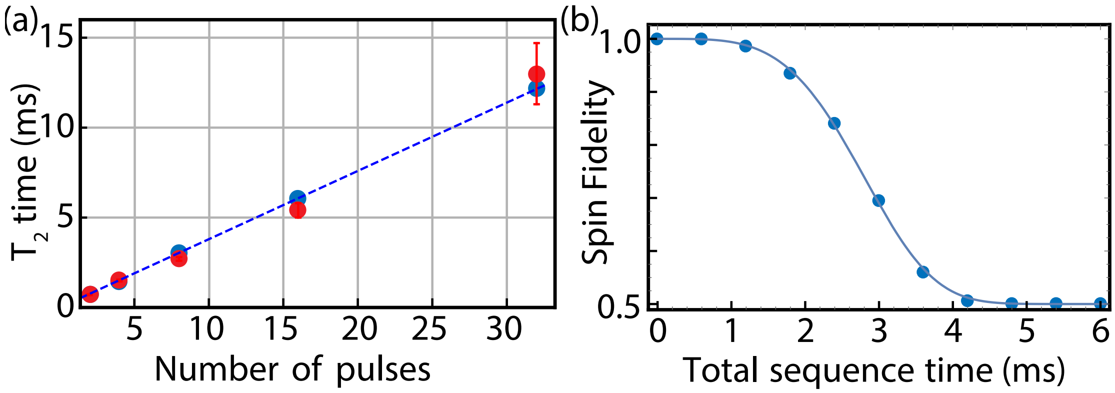

Figure B.10: Double-Gaussian noise power spectrum. (a) Calculated T_2 times for CP sequences (blue points) and measured T_2 times (red points). Dashed line is a linear fit. (b) Calculated CP8 curve (dots) fitted by a strecthed exponential with $n = 4$ (solid line).

we use a stretched exponential with $n = 4$ since is gives the smallest fit residuals [Fig. B.9(inset)]. Using the present data it is not possible to distinguish between different noise models as we can't directly deconvolve the noise power spectrum[100,184].

In figure 2.3(f), we show the dependance of the T_2^* time on the magnetic field amplitude which indicates additional noise in the system (see sec. B.8). In contrast, we do not observe any dependence of the T_2 time on magnetic field [Fig. B.8(b)]. This suggests a bimodal noise power spectrum: a slow-frequency component limits the T_2^* time while a high-frequency component determines the T_2 time. For example, a double-Gaussian noise power spectrum:

$$S(\omega) = A \times \exp\left[-\left({}^{\omega}/_{\omega_0}\right)^2\right] + B \times \exp\left[-\left({}^{\omega}/_{\omega_1}\right)^2\right], \tag{B.1}$$

where $A \approx 1\,\mathrm{MHz}$, $\omega_0 \approx 1.8\,\mathrm{kHz}$, $B \approx 1\,\mathrm{GHz}$, and $\omega_1 \approx 50\,\mathrm{Hz}$, provides a good agreement with the observed T_2 scaling [Fig. B.10(a)] and the correct order-of-magnitude for $T_2^* \approx 10\,\mathrm{s}$. In this case, the calculated CP8 curve is close to a stretched exponential with $n = 4$ [Fig. B.10(b)]. The same result can be obtained using a double-Lorentzian noise power spectrum with hard frequency cutoffs[185].

C

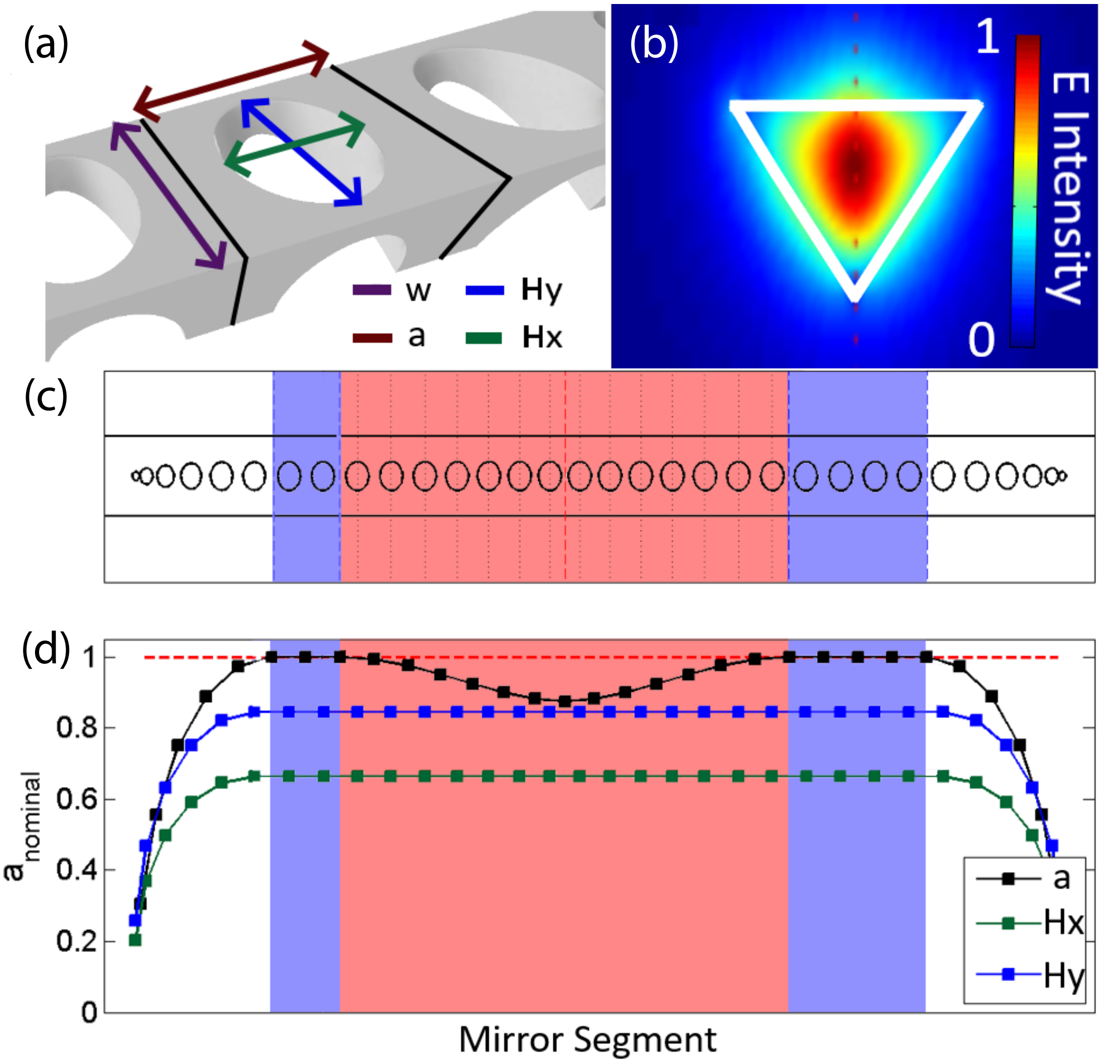

Figure C.1: (a) Unit cell of a photonic crystal cavity (bounded by black lines). H_x and H_y define the size and aspect ratio of the hole, a determines the lattice constant, and w sets the waveguide width. (b) Electric field intensity profile of the TE mode inside the cavity, indicating strong confinement of the optical mode inside the waveguide. (c) Schematic of photonic crystal design. Blue shaded region is the bandgap generating structure, red shaded region represents the cavity structure. (d) Plot of a, H_x, and H_y for the cavity shown in (c), showing cubic taper which defines the cavity region. All sizes are shown in fractions of a_{nominal}, the unperturbed lattice constant.

Supplementary information for chapters 3 and 4

C.1 Nanophotonic cavity design

We simulate and optimize our nanophotonic structures to maximize atom-photon interactions while maintaining high waveguide coupling, which ensures good collection efficiency for the devices. In particular, this requires optimizing the device quality-factor to mode volume ratio, the relative rates of scattering into waveguide modes, and the size and shape of the optical mode. Each of these quantities are considered in a three-step simulation process (FDTD, Lumerical). We first perform a coarse parameter sweep over all possible unit cells which define the photonic crystal gemometry and identify families of bandgap-generating structures. These structures are the starting point for a gradient ascent optimization procedure, which results in generating high quality-factor, low mode volume resonators. Finally, the generated designs are modified to ensure efficient resonator-waveguide coupling.

Optimization begins by exploring the full parameter space of TE-like bandgap generating structures within our waveguide geometry. For hole-based cavities [Fig. C.1(a)], this sweep covers a 5-dimensional parameter space: The lattice constant of the unit cell (a), the hole size and aspect ratio (H_x and H_y), the device etch angle (θ) and the waveguide width (w). Due to the size of this parameter space, we start by performing a low-resolution sweep over all parameters, with each potential design simulated by a single unit cell with the following boundary conditions: 4 perfectly matched layer (PML) boundary conditions in the transverse directions and 2 Bloch boundary conditions in the waveguide directions. The band structure of candidate geometries are determined by sweeping the effective k-vector of the Bloch boundary condition and identifying allowed modes. Using this technique, families of similar structures with large bandgaps near the SiV transition frequency are chosen for further simulation. Each candidate photonic crystal is also inspected for the position of its optical mode maximum, ensuring that it has first-order modes concentrated in the center of the diamond, where SiVs will be incorporated [Fig. C.1(b)].

The second step is to simulate the full photonic crystal cavity design, focused in the regions of parameter space identified in step one. This is done by selecting a fixed θ, as well as a total number of unit cells that define the structure, then modifying the bandgap of the photonic crystal with a defect region to form a cavity mode. We define this defect using a cubic tapering of one (or several) possible parameters:

$$A(x) = 1 - d_{\max}|2x^3 - 3x^2 + 1| \tag{C.1}$$

where A is the relative scale of the target parameter(s) at a distance x from the cavity center, and d_{max} is the defect depth parameter. Photonic Crystal cavities with multi-parameter defects are difficult to reliably fabricate, therefore, devices used in this work have cavity defect geometries defined only by variations in the lattice constant. The cavity generated by this defect is scored by simulating the optical spectrum and mode profile and computing the scoring function F:

$$F = \min(Q, Q_{\text{cutoff}})/(Q_{\text{cutoff}} \times V_{\text{mode}}) \tag{C.2}$$

Where Q is the cavity quality-factor, $Q_{\text{cutoff}} = 5 \times 10^5$ is an estimated maximum realizable Q based on fabrication constraints, and V_{mode} is the cavity mode volume. Based on this criteria, we employ a gradient ascent process over all cavity design parameters (except θ and the total number of unit cells) until F is maximized, or a maximum number of iterations has occurred. Due to the complexity and size of the parameter space, a single iteration of this gradient ascent is unlikely to find the optimal structure. Instead, several candidates from each family of designs found in step one are explored, with the best moving on to the final step of the simulation process. These surviving candidates are again checked to ensure confinement of the optical mode in the center of the cavity structure and to ensure that the structures fall within the tolerances of the fabrication process.

The final step in the simulation process is to modify the optimized designs to maximize resonator-waveguide coupling. This is done by removing unit cells from the input port of the device, which decreases the overall quality-factor of the devices in exchange for better waveguide damping of the optical field. Devices are once again simulated and analyzed for the fraction of light leaving the resonator through the waveguide compared to the fraction scattering into free-space. The number of unit cells on the input port is then optimized for this ratio, with simulations indicating that more than 95% of light is collected into the waveguide. In practice, fabrication defects increase the free-space scattering rate, placing resonators close to the critically-coupled regime. Finally, the waveguide coupling fraction is increased by appending a quadratic taper to both ends of the devices such that the optical mode is transferred adiabatically from the photonic crystal region into the diamond waveguide. This process produces the final cavity structure used for fabrication [Fig. C.1(c)].

C.2 Strain-induced frequency fluctuations

In this Appendix we calculate changes the SiV spin-qubit frequency and optical transition frequency arising from strain fluctuations. We start with the Hamiltonian for SiV in an external magnetic field B_z aligned along trhe SiV symmetry axis[37,121]:

$$H = \underbrace{-\lambda \begin{pmatrix} 0 & 0 & i & 0 \\ 0 & 0 & 0 & -i \\ -i & 0 & 0 & 0 \\ 0 & i & 0 & 0 \end{pmatrix}}_{\text{spin-orbit}} + \underbrace{\begin{pmatrix} \alpha-\beta & 0 & \gamma & 0 \\ 0 & \alpha-\beta & 0 & \gamma \\ \gamma & 0 & \beta & 0 \\ 0 & \gamma & 0 & \beta \end{pmatrix}}_{\text{strain}} + \underbrace{q\gamma_L B_z \begin{pmatrix} 0 & 0 & i & 0 \\ 0 & 0 & 0 & i \\ -i & 0 & 0 & 0 \\ 0 & -i & 0 & 0 \end{pmatrix}}_{\text{orbital Zeeman}} + \underbrace{\frac{\gamma_S B_z}{2} \begin{pmatrix} 1 & 0 & 0 & 0 \\ 0 & -1 & 0 & 0 \\ 0 & 0 & 1 & 0 \\ 0 & 0 & 0 & -1 \end{pmatrix}}_{\text{spin Zeeman}}, \quad (C.3)$$

where λ is a spin-orbit coupling constant, $\gamma_L = \mu_B$ and $\gamma_S = 2\mu_B$ are Landé g-factors of the orbital and spin degrees of freedom (μ_B the Bohr magneton), $q = 0.1$ is a Ham reduction factor of the orbital momentum[37,186], and α, β, γ are local strain parameters which can be different for the ground and excited sates [Sec. 3.4]. As measuring the exact strain parameters is challenging [Sec. 3.4] we assume only one non-zero component in this tensor (ϵ_{zx}) in order to simplify our calculations. In this case, strain parameters are:

$$\beta = f_{\mathrm{g(e)}}\epsilon_{zx}, \tag{C.4}$$

$$\alpha = \gamma = 0, \tag{C.5}$$

where $f_{\mathrm{g(e)}} = 1.7 \times 10^6\,(3.4 \times 10^6)$ GHz/strain[121] for the ground (excited) state and the GS splitting is:

$$\Delta_{GS} = 2\sqrt{\lambda_g^2 + \beta^2}, \tag{C.6}$$

where $\lambda_g \approx 25$ GHz is the SO-constant for the ground state. Next, we solve this Hamiltonian and investigate how the qubit frequency changes as a function of relative strain fluctuations (ξ):

$$\Delta f_{\mathrm{MW}} = \frac{2\left(f_{\mathrm{g}}\epsilon_{zx}\right)^2 \lambda_g B_z q \gamma_L}{\left(\left(f_{\mathrm{g}}\epsilon_{zx}\right)^2 + \lambda_g^2\right)^{3/2}}\xi. \tag{C.7}$$

The corresponding change in the optical frequency is:

$$\Delta f_{\mathrm{optical}} = \left(\frac{\left(f_{\mathrm{g}}\epsilon_{zx}\right)^2}{\sqrt{\left(f_{\mathrm{g}}\epsilon_{zx}\right)^2 + \lambda_g^2}} - \frac{\left(f_{\mathrm{e}}\epsilon_{zx}\right)^2}{\sqrt{\left(f_{\mathrm{e}}\epsilon_{zx}\right)^2 + \lambda_e^2}}\right)\xi, \tag{C.8}$$

where $\lambda_e \approx 125$ GHz is the SO-constant for the excited state.

For SiV 2 [Sec. 3.4] we measured $\Delta_{GS} = 140$ GHz and find $\epsilon_{zx} = 3.8 \times 10^{-5}$. With $\xi = 1\%$ strain fluctuations (corresponding to $\sim 10^{-7}$ strain), frequencies change by $\Delta f_{\mathrm{MW}} \approx 4$ MHz and $\Delta f_{\mathrm{optical}} \approx -300$ MHz. This quantitatively agrees with the data

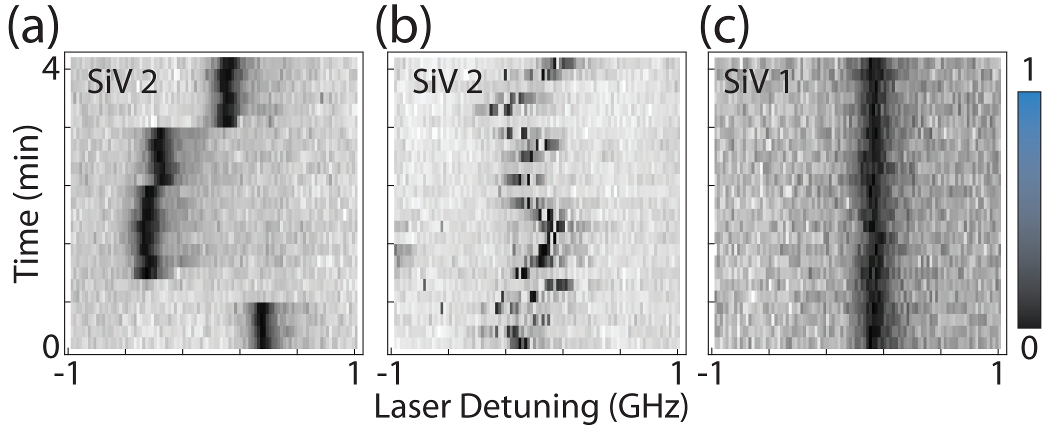

Figure C.2: (a) Spectral diffusion of SiV 2. We observe slow spectral wandering as well as spectral jumps. (b) Applying a short green repumping pulse before every measurement significanly speeds up the timescale for spectral diffusion. (c) Spectral diffusion of SiV 1 in nanostructures. Line is stable to below $100\,\mathrm{MHz}$ over many minutes. Scale bar indicates normalized SiV reflection signal.

presented in [Fig. 3.4(f)].

C.3 Mitigating spectral diffusion

In order to couple SiV centers to a quantum network, electronic transitions must be stabilized with respect to a probe laser. We note that such spectral diffusion is a universal challenge for solid-state quantum systems[86,187,188]. In the case of the SiV center, spectral diffusion can be seen explicitly in figure C.2(a), where the optical transition frequency can either drift slowly (central region), or undergo large spectral jumps. As this diffusion can be larger than the SiV linewidth, any given instance of an experiment could have the probe laser completely detuned from the atomic transition, resulting in a failed experiment.

There are several possible solutions to mitigate this spectral diffusion. First, exploiting a high-cooperativity interface, one can Purcell-broaden the optical linewidth [sec. 3.5] to exceed the spectral diffusion[40]. Second, a high collection efficiency can be used to read out the optical position faster than the spectral diffusion. The frequency can then be probabilistically stabilized by applying a short laser pulse at 520 nm which dramatically speeds up the timescale of spectral diffusion,[41,163] [Fig. C.2(b)]. Alternatively this signal could be used to actively stabilize the line using strain-tuning[148,189]. From the observations in figure 3.4(f), this technique should mitigate spectral diffusion of both the optical and spin transitions. Strain tuning also offers the capability to control the DC strain value, which has important effects on qubit properties as discussed previously, and enables tuning multiple SiV centers to a common network operation frequency. As such, this tunability will likely be an important part of future quantum networking technologies based on SiV centers.

The severity of spectral diffusion is different for different emitters however, and this control is not always necessary, especially for proof-of-principle experiments with a small number of emitters. For SiV 1, the main SiV used in the following sections, and the SiV used in chapter 4, we find almost no spectral diffusion, with optical transitions stable over many minutes [Fig. C.2(c)]. This is an ideal configuration, as experiments can be performed without any need to verify the optical line position.

C.4 Model for SiV decoherence

The scaling of $T_2(N) \propto N^{2/3}$ is identical to that found for nitrogen-vacancy centers, where it is assumed that T_2 is limited by a fluctuating electron spin bath[97,140]. Motivated by DEER measurements with SiV 2, we follow the analysis of ref.[140] to estimate the noise bath observed by SiV 1.

The measured coherence decay is modeled by:

$$\langle S_z \rangle = \mathrm{Exp}\left(- \int \mathrm{d}\omega \, S(\omega) \mathcal{F}_N(t, \omega) \right), \tag{C.9}$$

where $S(\omega)$ is the noise power-spectrum of the bath, and $\mathcal{F}_N(t,\omega) = 2\sin(\omega t/2)(1 - \sec(\omega t/2N))^2/\omega^2$ is filter function for a dynamical-decoupling sequence with an even number of pulses[140]. We fit sucessive T_2 echo curves to the functional form $A + Be^{-(t/T_2)^\beta}$, with A, B being free parameters associated with photon count rates, and $\beta = 3$ providing the best fit to the data. This value of β implies a decoherence bath with a Lorentzian noise power-spectrum, $S(\omega, b, \tau) = b^2\tau/\pi \times 1/(1 + \omega^2\tau^2)$, where b is a parameter corresponding to the strength of the noise bath, and τ is a parameter corresponding to the correlation time of the noise[97,140].

Empirically, no one set of noise parameters faithfully reproduces the data for all measured echo sequences. Adding a second source of dephasing $\tilde{S} = S(\omega, b_1, \tau_1) + S(\omega, b_2, \tau_2)$, gives reasonable agreement with the data using parameters b_1 =5 kHz,

τ_1 =1 s, b_2 =180 kHz, τ_2 =1 ms [Fig. 3.7(d)]. The two drastically different set of noise parameters for each of the sources can help illuminate the source of noise in our devices.

As explained in the previous section, one likely candidate for this decoherence is a bath of free electrons arising from improper surface termination or local damage caused during nanofabrication, which are known to have correlation times in the ∼s range. The SiV studied in this analysis is approximately equidistant from three surfaces: the two nearest holes which define the nanophotonic cavity, and the top surface of the nanobeam [sec: 3.2], all of which are approximately 50 nm away. We estimate a density of $\sigma_{\mathrm{surf}} = 0.067$ spins/nm^2 using:

$$b_1 = \gamma_{\mathrm{SiV}} \langle B_{\mathrm{surf}} \rangle = \frac{\mathrm{g}^2 \mu_B^2 \mu_0}{\hbar} \frac{1}{4\pi \Sigma d_i^2} \sqrt{\frac{\pi}{4\sigma_{\mathrm{surf}}}} \tag{C.10}$$

where b_1 is the measured strength of the noise bath, g is the electron gyromagnetic ratio, and d_i are the distances to the nearest surfaces. This observation is consistent with surface spin densities measured using NVs[140].

The longer correlation time for the second noise term suggests a different bath, possibly arising from free electron spins inside the bulk diamond. Vacancy clusters, which can persist under annealing even at 1200 C, are known to posses $g = 2$ electron spins, and are one possible candidate for this noise bath[190]. Integrating over d in eq. C.10, we estimate the density of spins required to achieve the measured b_2. We estimate

$\rho_{\text{bulk}} \sim 0.53$ spins per nm^3, which corresponds to a doping of 3ppm. Interestingly, this is nearly identical to the local concentration of silicon incorporated during implantation (most of which is not successfully converted into negatively charged SiV), and could imply implantation-related damage as a possible source of these impurities.

Another possible explanation for this slower bath could be coupling to nuclear spins in the environment. The diamond used in this experiment has a natural abundance of ^{13}C, a spin-1/2 isotope, in concentrations of approximately 1.1%. Replacing $\mu_B \rightarrow \mu_N$ in the term for $\langle B \rangle$ gives an estimated nuclear spin density of $\rho_{\text{bulk,N}} = 0.6\%$, only a factor of two different than the expected nuclear spin density.

C.5 Concurrence and Fidelity calculations

C.5.1 Spin-photon concurrence and fidelity calculations

From correlations in the Z- and X-bases, we estimate a lower bound for the entanglement in our system. Following reference[191], we note that the density matrix of our system conditioned on the detection of one photon can be described as:

$$\rho_{ZZ} = 1/2 \begin{pmatrix} p_{e\uparrow} & 0 & 0 & 0 \\ 0 & p_{e\downarrow} & c_{e\downarrow,l\uparrow} & 0 \\ 0 & c^{\dagger}_{e\downarrow,l\uparrow} & p_{l\uparrow} & 0 \\ 0 & 0 & 0 & p_{l\downarrow} \end{pmatrix} \tag{C.11}$$

where p_{ij} are the probabilities of measuring a photon in state i, and the spin in state j. $c_{e\downarrow,l\uparrow}$ represents entanglement between $p_{e\uparrow}$ and $p_{l\downarrow}$. We set all other coherence terms to zero, as they represent negligibly small errors in our system (for example, $c_{e\uparrow,e\downarrow} > 0$ would imply that the SiV was not initialized properly at the start of the measurement). We quantify the degree of entanglement in the system by its concurrence $\mathcal{C}$, which is 0 for seperable states, and 1 for a maximally entangled state[192]:

$$\mathcal{C} = \mathrm{Max}(0, \lambda_0^{1/2} - \sum_{i=1}^{N} \lambda_i^{1/2}), \tag{C.12}$$

where λ_i are the eigenvalues of the matrix $\rho_{ZZ} \cdot \left(\sigma_y \cdot \rho_{ZZ} \cdot \sigma_y^{\dagger}\right)$, and σ_y is the standard Pauli matrix acting on each qubit basis separately ($\sigma_y = \sigma_{y,\mathrm{ph}} \otimes \sigma_{y,\mathrm{el}}$). While this can be solved exactly, the resulting equation is complicated. Taking only the first-order terms, this can be simplified to put a lower bound on the concurrence:

$$\mathcal{C} \geq 2(|c_{e\downarrow,l\uparrow}| - \sqrt{p_{e\uparrow} p_{l\downarrow}}) \tag{C.13}$$

We measure p direcly in the Z basis, and estimate $|c_{e\downarrow,l\uparrow}|$ by performing measurements in the X basis. A $\pi/2$-rotation on both the photon and spin qubits rotates:

$$|e\rangle \rightarrow 1/\sqrt{2}(|e\rangle + |l\rangle), \quad |l\rangle \rightarrow 1/\sqrt{2}(|e\rangle - |l\rangle)$$
$$|\downarrow\rangle \rightarrow 1/\sqrt{2}(|\downarrow\rangle + |\uparrow\rangle), \quad |\uparrow\rangle \rightarrow 1/\sqrt{2}(|\downarrow\rangle - |\uparrow\rangle)$$

Afer this transformation, the signal contrast directly measures $c_{e\downarrow,l\uparrow}$:

$$2c_{e\downarrow,l\uparrow} = p_{-,\leftarrow} + p_{+,\rightarrow} - p_{-\rightarrow} - p_{+\leftarrow} \tag{C.14}$$
$$\Rightarrow \mathcal{C} \geq 0.42(6) \tag{C.15}$$

Similarly, the fidelity of the entangled state (post-selected on the detection of a photon) can be computed by the overlap with the target Bell state[155]:

$$F = \langle\Psi^+|\rho_{ZZ}|\Psi^+\rangle = (p_{e\uparrow} + p_{l\downarrow} + 2c_{e\downarrow,l\uparrow})/2 \geq 0.70(3) \tag{C.16}$$

C.5.2 Correcting for readout infidelity

Errors arising from single-shot readout incorrectly assign the spin state, results in lower-contrast histograms for spin-photon correlations. We follow the analysis done in ref.[155], and correct for readout errors using a transfer matrix formalism. The measured spin-photon correlations p_{ij} are related to the 'true' populations P_{ij} via:

$$\begin{pmatrix} p_{e\downarrow} \\ p_{e\uparrow} \\ p_{l\downarrow} \\ p_{l\uparrow} \end{pmatrix} = \begin{pmatrix} F_{\downarrow} & 1-F_{\uparrow} & 0 & 0 \\ 1-F_{\downarrow} & F_{\uparrow} & 0 & 0 \\ 0 & 0 & F_{\downarrow} & 1-F_{\uparrow} \\ 0 & 0 & 1-F_{\downarrow} & F_{\uparrow} \end{pmatrix} \begin{pmatrix} P_{e\downarrow} \\ P_{e\uparrow} \\ P_{l\downarrow} \\ P_{l\uparrow} \end{pmatrix} \tag{C.17}$$

with $F_{\downarrow}, \quad F_{\uparrow}$ defined above. After this correction, an identical analysis is performed to calculate the error-corrected histograms [Fig. 3.8(b,c,d) dark-shading]. We find an error-corrected concurrence $\mathcal{C} \geq 0.79(7)$ and fidelity $F \geq 0.89(3)$.

C.5.3 Electron-nuclear concurrence and fidelity calculations

For spin-spin Bell states, in contrast to the spin-photon analysis, we can no longer set any of the off-diagonal terms of the density matrix [eq. C.11] to zero due to the limited ($\sim 90\%$) nuclear initialization fidelity. We note that neglecting these off-diagonal terms can only decrease the estimated entanglement in the system, thus the concurrence can still be written as:

$$\mathcal{C} \geq 2(|c_{\downarrow\uparrow}| - \sqrt{p_{\uparrow\uparrow}p_{\downarrow\downarrow}}) \tag{C.18}$$

where the first subscript is the electron spin state, and the second is the nuclear state. We estimate $c_{\downarrow\uparrow}$ again by using the measured populations in an orthogonal basis. In this case, off-diagonal terms add a correction:

$$2c_{\downarrow\uparrow} + 2c_{\uparrow\downarrow} = p_{\leftarrow\leftarrow} + p_{\rightarrow\rightarrow} - p_{\leftarrow\rightarrow} - p_{\rightarrow\leftarrow} \tag{C.19}$$

In order for the density matrix to be properly normalized, $c_{\uparrow\downarrow} \leq \sqrt{p_{\uparrow\uparrow}p_{\downarrow\downarrow}}$, giving us the final concurrence:

$$\mathcal{C} \geq p_{\leftarrow\leftarrow} + p_{\rightarrow\rightarrow} - p_{\leftarrow\rightarrow} - p_{\rightarrow\leftarrow} - 4\sqrt{p_{\uparrow\uparrow}p_{\downarrow\downarrow}} \tag{C.20}$$

Additionally, both electron readout error as well as ^{13}C mapping infidelity can misreport the true spin state. As such, the new transfer matrix to correct for this error is:

$$\begin{pmatrix} F_{\downarrow,e}F_{\downarrow,N} & F_{\downarrow,e}(1-F_{\uparrow,N}) & (1-F_{\uparrow,e})F_{\downarrow,N} & (1-F_{\uparrow,e})(1-F_{\uparrow,N}) \\ F_{\downarrow,e}(1-F_{\downarrow,N}) & F_{\downarrow,e}F_{\uparrow,N} & (1-F_{\uparrow,e})(1-F_{\downarrow,N}) & (1-F_{\uparrow,e})F_{\uparrow,N} \\ (1-F_{\downarrow,e})F_{\downarrow,N} & (1-F_{\downarrow,e})(1-F_{\uparrow,N}) & F_{\uparrow,e}F_{\downarrow,N} & F_{\uparrow,e}(1-F_{\uparrow,N}) \\ (1-F_{\downarrow,e})(1-F_{\downarrow,N}) & (1-F_{\downarrow,e})F_{\uparrow,N} & F_{\uparrow,e}(1-F_{\downarrow,N}) & F_{\uparrow,e}F_{\uparrow,N} \end{pmatrix} \tag{C.21}$$

Where $F_{\downarrow,e} \approx F_{\uparrow,e} = 0.85$ and $F_{\downarrow,N} \approx F_{\uparrow,N} = 0.72$. Following this analysis, we report an error-corrected concurrence of $\mathcal{C} \geq 0.22(9)$.

C.5.4 Electron-nuclear CNOT gate

We further characterize the CNOT gate itself as a universal quantum gate. Due to the relatively poor readout fidelity (see above), we do not do this by performing quantum state tomography. Instead, we estimate entries in the CNOT matrix using measurements in only the Z-basis. As a control measurement, we first initialize the two qubits in all possible configurations and read out, averaged over many trials. Next, we initialize the qubits, perform a CNOT gate, and read out, again averaged over many trials, normalized by the control data. Any reduction in contrast after normalization is attributed to the opposite spin state, establishing a system of equations for determining the CNOT matrix. We solve this system of equations, marginalizing over free parameters to determine a MLE estimate for the CNOT transfer matrix, as seen in chapter 4.

C.6 Nuclear initialization and readout

Initialization (and readout) of the ^{13}C spin can be done by mapping population between the SiV spin and the ^{13}C. Following reference[146], we note that Z and X gates are possible with dynamical-decoupling based nuclear gates, thus a natural choice for initialization are gates comprised of both $\mathcal{R}^{\pi/2}_{\pm x,\mathrm{SiV-C}}$ and $\mathcal{R}^{\pi/2}_{z,\mathrm{SiV-C}}$, as shown in figure C.3(a) and in reference[146]. We note here that it should be possible to combine the

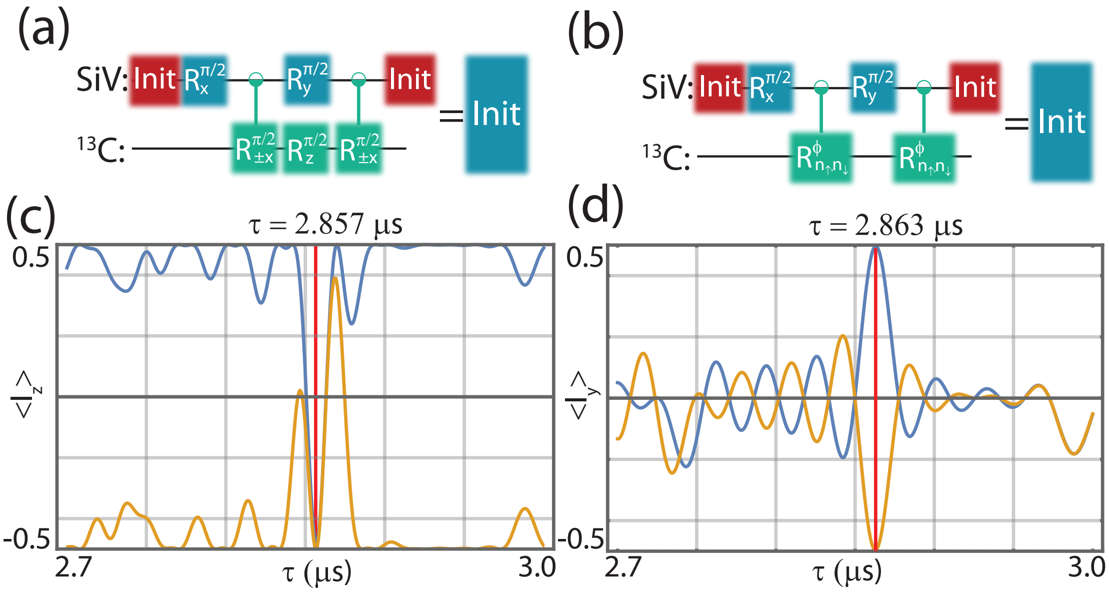

Figure C.3: (a) Original initialization sequence from[146], note $\mathcal{R}_{z,\mathrm{C}}^{\pi/2}$ rotation. (b) Simplified initialization sequence used in this work. (c) Simulated performance of the initialization gate from (b) using 8 $\pi-$pulses per each nuclear gate, the initial state is $|\uparrow\uparrow\rangle$ (blue) and $|\uparrow\downarrow\rangle$ (orange). The resonances are narrow compared to (d) due to applying effectively twice more $\pi-$pulses (d) Simulated performance of $\mathcal{R}_{\pm x,\mathrm{SiV-C}}^{\pi/2}$ gate for 8 $\pi-$pulses for SiV-^{13}C register initialized in $|\uparrow\uparrow\rangle$ (blue) and $|\downarrow\uparrow\rangle$ (orange) effects of $\mathcal{R}_x$ and $\mathcal{R}_z$ rotations in a single gate, which has the potential of shortening and simplifying the total initialzation gate. One proposed sequence uses the following entangling gate:

$$\mathcal{R}^{\phi}_{\vec{n_\uparrow},\vec{n_\downarrow}} = \begin{pmatrix} (1+i)/2 & i/\sqrt{2} & 0 & 0 \\ i/\sqrt{2} & (1-i)/\sqrt{2} & 0 & 0 \\ 0 & 0 & (1+i)/2 & -i/\sqrt{2} \\ 0 & 0 & -i/\sqrt{2} & (1-i)/2 \end{pmatrix}$$

$$= \begin{pmatrix} R^{\pi/2}_{\Theta=\pi/4} R^{\pi/2}_z & 0 \\ 0 & R^{-\pi/2}_{\Theta=\pi/4} R^{\pi/2}_z \end{pmatrix} \quad \text{(C.22)}$$

which corresponds to a rotation on the angle $\phi = 2\pi/3$ around the axes $n_{\uparrow,\downarrow} = \{\pm\sqrt{2}, 0, 1\}/\sqrt{3}$. The matrix of entire initialization gate [Fig. C.3(b)] built from this gate would then be:

$$\text{Init} = \begin{pmatrix} 0 & 0 & -(1+i)/2 & -1/\sqrt{2} \\ i/\sqrt{2} & -(1+i)/2 & 0 & 0 \\ 0 & 0 & -(1-i)/2 & -i/\sqrt{2} \\ 1/\sqrt{2} & (1-i)/2 & 0 & 0 \end{pmatrix} \quad \text{(C.23)}$$

which results in an initialized ^{13}C spin.

To demonstrate this, we numerically simulate a MW pulse sequence using the exact coupling parameters of our ^{13}C[Ch. 4] and 8 $\pi-$pulses for each $\mathcal{R}^{\phi}_{\vec{n_\uparrow},\vec{n_\downarrow}}$ gate. Figure C.3(c) shows that regardless of the initial state, the ^{13}C always ends up in state $|{\downarrow}\rangle$ (given that the SiV was initialized in $|{\uparrow}\rangle$). As expected, the timing of this gate ($\tau_{\text{init}} = 2.857\,\text{s}$) is noticeably different from the timing of the $\mathcal{R}^{\pi/2}_{\pm x,\text{SiV}-\text{C}}$ gate ($\tau_{\pi/2} = 2.851\,\text{s}$), which occurs at spin-echo resonances [Fig. C.3(d)].

The rotation matrix for this sequence at $\tau = \tau_{\text{init}}$ (with the SiV initialized in $|{\uparrow}\rangle$) is:

$$\mathcal{R}^{\phi}_{n_\uparrow} = \begin{pmatrix} 0.55 + 0.51i & 0 + 0.65i \\ 0.65i & 0.55 - 0.52i \end{pmatrix} \tag{C.24}$$

corresponding to a rotation angle $\phi = 0.63\pi$ around the axis $n_\uparrow = \{0.78, 0, 0.62\}$, very close to the theoretical result.

Since the experimental fidelities for both initialization gates [Fig. C.3 (a,b)] are similar, we use sequence (b) to make the gate shorter and avoid unnecessary pulse-errors.

References

[1] N. Bohr. On the constitution of atoms and molecules. *Philos. Mag.*, 26(1), 1913.

[2] N.W. Ashcroft and N.D. Mermin. *Solid State Physics.* Saunders College, Philadelphia, 1976.

[3] Shenna M. LaPointe and Donald F. Weaver. A review of density functional theory quantum mechanics as applied to pharmaceutically relevant systems. *Current Computer-Aided Drug Design*, 3(4):290–296, 2007.

[4] K. Kim, M. Chang, S. Korenblit, R. Islam, E. E. Edwards, J. K. Freericks, G. Lin, L Duan, and C. Monroe. Quantum simulation of frustrated ising spins with trapped ions. *Nature*, 465:590–593, 2010.

[5] K. A. Landsman, Y. Wu, P. H. Leung, D. Zhu, N. M. Linke, K. R. Brown, L. Duan, and C. Monroe. Two-qubit entangling gates within arbitrarily long chains of trapped ions. *Phys. Rev. A*, 100:022332, Aug 2019.

[6] Ivaylo S. Madjarov, Jacob P. Covey, Adam L. Shaw, Joonhee Choi, Anant Kale, Alexandre Cooper, Hannes Pichler, Vladimir Schkolnik, Jason R. Williams, and Manuel Endres. High-fidelity control, detection, and entanglement of alkaline-earth rydberg atoms. *arXiv preprint arXiv:2001.04455*, 2017.

[7] Christian Gross and Immanuel Bloch. Quantum simulations with ultracold atoms in optical lattices. *Science*, 357(6355):995–1001, 2017.

[8] Vincent Lienhard, Sylvain de Léséleuc, Daniel Barredo, Thierry Lahaye, Antoine Browaeys, Michael Schuler, Louis-Paul Henry, and Andreas M. Läuchli. Observing the space- and time-dependent growth of correlations in dynamically tuned synthetic ising models with antiferromagnetic interactions. *Phys. Rev. X*, 8:021070, Jun 2018.

[9] Matthew Rispoli, Alexander Lukin, Robert Schittko, Sooshin Kim, M. Eric Tai, Julian Léonard, and Markus Greiner. Quantum critical behaviour at the many-body localization transition. *Nature*, 573(7774):385–389, 2019.

[10] Hannes Bernien, Sylvain Schwartz, Alexander Keesling, Harry Levine, Ahmed Omran, Hannes Pichler, Soonwon Choi, Alexander S. Zibrov, Manuel Endres, Markus Greiner, Vladan Vuletic, and Mikhail D. Lukin. Probing many-body dynamics on a 51-atom quantum simulator. *Nature*, 551(7682):579–584, 2017.

[11] M. H. Devoret and R. J. Schoelkopf. Superconducting circuits for quantum information: An outlook. *Science*, 339(6124):1169–1174, 2013.

[12] Frank Arute, Kunal Arya, others, and John M. Martinis. Quantum supremacy using a programmable superconducting processor. *Nature*, 574:505–510, 2019.

[13] C. Monroe, R. Raussendorf, A. Ruthven, K. R. Brown, P. Maunz, L.-M. Duan, and J. Kim. Large-scale modular quantum-computer architecture with atomic memory and photonic interconnects. *Phys. Rev. A*, 89:022317, Feb 2014.

[14] H Jeff Kimble. The quantum internet. *Nature*, 453(7198):1023–1030, 2008.

[15] Stephanie Wehner, David Elkouss, and Ronald Hanson. Quantum internet: A vision for the road ahead. *Science*, 362(6412), 2018.

[16] Charles H. Bennett and Gilles Brassard. Quantum cryptography: Public key distribution and coin tossing. *Theoretical Computer Science*, 560:7 – 11, 2014.

[17] Daniel Gottesman, Thomas Jennewein, and Sarah Croke. Longer-baseline telescopes using quantum repeaters. *Phys. Rev. Lett.*, 109:070503, Aug 2012.

[18] P. Kómár, E. M. Kessler, M. Bishof, L. Jiang, A. S. Sørensen, J. Ye, and M. D. Lukin. A quantum network of clocks. *Nature Physics*, 10:582 EP –, 06 2014.

[19] A. Broadbent, J. Fitzsimons, and E. Kashefi. Universal blind quantum computation. In *2009 50th Annual IEEE Symposium on Foundations of Computer Science*, pages 517–526, Oct 2009.

[20] Andreas Reiserer, Norbert Kalb, Gerhard Rempe, and Stephan Ritter. A quantum gate between a flying optical photon and a single trapped atom. *Nature*, 508(7495):237–240, 2014.

[21] C. Crocker, M. Lichtman, K. Sosnova, A. Carter, S. Scarano, and C. Monroe. High purity single photons entangled with an atomic qubit. *Opt. Express*, 27(20):28143–28149, Sep 2019.

[22] Stephan Welte, Bastian Hacker, Severin Daiss, Stephan Ritter, and Gerhard Rempe. Cavity carving of atomic bell states. *Phys. Rev. Lett.*, 118:210503, May 2017.

[23] Peter Lodahl, Sahand Mahmoodian, and Søren Stobbe. Interfacing single photons and single quantum dots with photonic nanostructures. *Rev. Mod. Phys.*, 87(2):347, 2015.

[24] Shuo Sun, Hyochul Kim, Glenn S Solomon, and Edo Waks. A quantum phase switch between a single solid-state spin and a photon. *Nat. Nanotechnol.*, 2016.

[25] L. Huthmacher, R. Stockill, E. Clarke, M. Hugues, C. Le Gall, and M. Atatüre. Coherence of a dynamically decoupled quantum-dot hole spin. *Phys. Rev. B*, 97:241413(R), Jun 2018.

[26] C. E. Bradley, J. Randall, M. H. Abobeih, R. C. Berrevoets, M. J. Degen, M. A. Bakker, M. Markham, D. J. Twitchen, and T. H. Taminiau. A 10-qubit solid-state spin register with quantum memory up to one minute. *arXiv preprint arXiv:1905.02094*, 2019.

[27] Peter C. Humphreys, Norbert Kalb, Jaco P. J. Morits, Raymond N. Schouten, Raymond F. L. Vermeulen, Daniel J. Twitchen, Matthew Markham, and Ronald Hanson. Deterministic delivery of remote entanglement on a quantum network. *Nature*, 558(7709):268–273, 2018.

[28] Chunlang Wang, Christian Kurtsiefer, Harald Weinfurter, and Bernd Burchard. Single photon emission from SiV centres in diamond produced by ion implantation. *Journal of Physics B: Atomic, Molecular and Optical Physics*, 39(1):37–41, dec 2005.

[29] Takayuki Iwasaki, Fumitaka Ishibashi, Yoshiyuki Miyamoto, Yuki Doi, Satoshi Kobayashi, Takehide Miyazaki, Kosuke Tahara, Kay D. Jahnke, Lachlan J. Rogers, Boris Naydenov, Fedor Jelezko, Satoshi Yamasaki, Shinji Nagamachi,

Toshiro Inubushi, Norikazu Mizuochi, and Mutsuko Hatano. Germanium-vacancy single color centers in diamond. *Sci. Rep.*, 5:12882, 08 2015.

[30] Takayuki Iwasaki, Yoshiyuki Miyamoto, Takashi Taniguchi, Petr Siyushev, Mathias H. Metsch, Fedor Jelezko, and Mutsuko Hatano. Tin-vacancy quantum emitters in diamond. *Phys. Rev. Lett.*, 119:253601, Dec 2017.

[31] Matthew E Trusheim, Noel H Wan, Kevin C Chen, Christopher J Ciccarino, Johannes Flick, Ravishankar Sundararaman, Girish Malladi, Eric Bersin, Michael Walsh, Benjamin Lienhard, et al. Lead-related quantum emitters in diamond. *Physical Review B*, 99(7):075430, 2019.

[32] G. V. Astakhov, D. Simin, V. Dyakonov, B. V. Yavkin, S. B. Orlinskii, I. I. Proskuryakov, A. N. Anisimov, V. A. Soltamov, and P. G. Baranov. Spin centres in sic for quantum technologies. *Applied Magnetic Resonance*, 47(7):793–812, 2016.

[33] A. M. Dibos, M. Raha, C. M. Phenicie, and J. D. Thompson. Atomic source of single photons in the telecom band. *Phys. Rev. Lett.*, 120:243601, Jun 2018.

[34] A. Dietrich, M. W. Doherty, I. Aharonovich, and A. Kubanek. Solid-state single photon source with fourier transform limited lines at room temperature. *Phys. Rev. B*, 101:081401, Feb 2020.

[35] E. Neu, D. Steinmetz, J. Riedrich-Möller, S. Gsell, M. Fischer, M. Schreck, and C. Becher. Single photon emission from silicon-vacancy colour centres in chemical vapour deposition nano-diamonds on iridium. *New J. Phys.*, 13(2):025012, 2011.

[36] J. P. Goss, P. R. Briddon, and M. J. Shaw. Density functional simulations of silicon-containing point defects in diamond. *Phys. Rev. B*, 76:075204, Aug 2007.

[37] C. Hepp, T. Müller, V. Waselowski, J. N. Becker, B. Pingault, H. Sternschulte, D. Steinmüller-Nethl, A. Gali, J. R. Maze, M. Atatüre, and C. Becher. Electronic structure of the silicon vacancy color center in diamond. *Phys. Rev. Lett.*, 112(3):036405, January 2014.

[38] L. J. Rogers, K. D. Jahnke, T. Teraji, L. Marseglia, C. Müller, B. Naydenov, H. Schauffert, C. Kranz, J. Isoya, L. P. McGuinness, and F. Jelezko. Multiple

intrinsically identical single-photon emitters in the solid state. *Nat. Commun.*, 5:4739, August 2014.

[39] Ruffin E Evans, Alp Sipahigil, Denis D Sukachev, Alexander S Zibrov, and Mikhail D Lukin. Narrow-linewidth homogeneous optical emitters in diamond nanostructures via silicon ion implantation. *Phys. Rev. Appl.*, 5(4):044010, 2016.

[40] Alp Sipahigil, RE Evans, DD Sukachev, MJ Burek, J Borregaard, MK Bhaskar, CT Nguyen, JL Pacheco, HA Atikian, C Meuwly, et al. An integrated diamond nanophotonics platform for quantum-optical networks. *Science*, 354(6314):847–850, 2016.

[41] R. E. Evans, M. K. Bhaskar, D. D. Sukachev, C. T. Nguyen, A. Sipahigil, M. J. Burek, B. Machielse, G. H. Zhang, A. S. Zibrov, E. Bielejec, H. Park, M. Lončar, and M. D. Lukin. Photon-mediated interactions between quantum emitters in a diamond nanocavity. *Science*, 362(6415):662–665, 2018.

[42] Lachlan J Rogers, Kay D Jahnke, Mathias H Metsch, Alp Sipahigil, Jan M Binder, Tokuyuki Teraji, Hitoshi Sumiya, Junichi Isoya, Mikhail D Lukin, Philip Hemmer, et al. All-optical initialization, readout, and coherent preparation of single silicon-vacancy spins in diamond. *Phys. Rev. Lett.*, 113(26):263602, 2014.

[43] Benjamin Pingault, Jonas N Becker, Carsten HH Schulte, Carsten Arend, Christian Hepp, Tillmann Godde, Alexander I Tartakovskii, Matthew Markham, Christoph Becher, and Mete Atatüre. All-optical formation of coherent dark states of silicon-vacancy spins in diamond. *Phys. Rev. Lett.*, 113(26):263601, 2014.

[44] Kay D Jahnke, Alp Sipahigil, Jan M Binder, Marcus W Doherty, Mathias Metsch, Lachlan J Rogers, Neil B Manson, Mikhail D Lukin, and Fedor Jelezko. Electron–phonon processes of the silicon-vacancy centre in diamond. *New J. Phys*, 17(4):043011, 2015.

[45] Jonas Nils Becker, Johannes Görlitz, Carsten Arend, Matthew Markham, and Christoph Becher. Ultrafast all-optical coherent control of single silicon vacancy colour centres in diamond. *Nat. Commun.*, 7:13512, 2016.

[46] Benjamin Pingault, David-Dominik Jarausch, Christian Hepp, Lina Klintberg, Jonas N Becker, Matthew Markham, Christoph Becher, and Mete Atatüre. Coherent control of the silicon-vacancy spin in diamond. *Nat. Commun.*, 8, 2017.

[47] Luis Dias Carlos and Fernando Palacio, editors. *Thermometry at the Nanoscale.* RSC Nanoscience and Nanotechnology. The Royal Society of Chemistry, 2016.

[48] Fabian Menges, Philipp Mensch, Heinz Schmid, Heike Riel, Andreas Stemmer, and Bernd Gotsmann. Temperature mapping of operating nanoscale devices by scanning probe thermometry. *Nat. Commun.*, 7:10874 EP –, 03 2016.

[49] Zhiping Cai, Alain Chardon, Huiying Xu, Patrice Féron, and Guy Michel Stéphan. Laser characteristics at 1535 nm and thermal effects of an er:yb phosphate glass microchip pumped by ti:sapphire laser. *Opt. Commun.*, 203(3):301–313, 2002.

[50] D. Patrick O'Neal, Leon R. Hirsch, Naomi J. Halas, J. Donald Payne, and Jennifer L. West. Photo-thermal tumor ablation in mice using near infrared-absorbing nanoparticles. *Cancer Lett.*, 209(2):171–176, 6 2004.

[51] Glen W. Walker, Vikram C. Sundar, Christina M. Rudzinski, Aetna W. Wun, Moungi G. Bawendi, and Daniel G. Nocera. Quantum-dot optical temperature probes. *Appl. Phys. Lett.*, 83(17):3555–3557, 2017/07/24 2003.

[52] Helin Liu, Yanyan Fan, Jianhai Wang, Zhongsen Song, Hao Shi, Rongcheng Han, Yinlin Sha, and Yuqiang Jiang. Intracellular temperature sensing: An ultra-bright luminescent nanothermometer with non-sensitivity to ph and ionic strength. *Sci. Rep.*, 5:14879, 10 2015.

[53] I. Sildos, A. Loot, V. Kiisk, L. Puust, V. Hizhnyakov, A. Yelisseyev, A. Osvet, and I. Vlasov. Spectroscopic study of ne8 defect in synthetic diamond for optical thermometry. *Diamond Relat. Mater.*, 76:27–30, 6 2017.

[54] Fiorenzo Vetrone, Rafik Naccache, Alicia Zamarrón, Angeles Juarranz de la Fuente, Francisco Sanz-Rodríguez, Laura Martinez Maestro, Emma Martín Rodriguez, Daniel Jaque, José García Solé, and John A. Capobianco. Temperature sensing using fluorescent nanothermometers. *ACS Nano*, 4(6):3254–3258, 06 2010.

[55] Sergii Kalytchuk, Kateřina Poláková, Yu Wang, Jens P. Froning, Klara Cepe, Andrey L. Rogach, and Radek Zbořil. Carbon dot nanothermometry: Intracellular photoluminescence lifetime thermal sensing. *ACS Nano*, 11(2):1432–1442, 02 2017.

[56] Satoshi Arai, Sung-Chan Lee, Duanting Zhai, Madoka Suzuki, and Young Tae Chang. A molecular fluorescent probe for targeted visualization of temperature at the endoplasmic reticulum. *Sci. Rep.*, 4:6701, 10 2014.

[57] Jon S. Donner, Sebastian A. Thompson, Mark P. Kreuzer, Guillaume Baffou, and Romain Quidant. Mapping intracellular temperature using green fluorescent protein. *Nano Letters*, 12(4):2107–2111, 04 2012.

[58] Taras Plakhotnik, Marcus W. Doherty, Jared H. Cole, Robert Chapman, and Neil B. Manson. All-optical thermometry and thermal properties of the optically detected spin resonances of the nv–center in nanodiamond. *Nano Lett.*, 14(9):4989–4996, 09 2014.

[59] V. M. Acosta, E. Bauch, M. P. Ledbetter, A. Waxman, L. S. Bouchard, and D. Budker. Temperature dependence of the nitrogen-vacancy magnetic resonance in diamond. *Phys. Rev. Lett.*, 104(7):070801–, 02 2010.

[60] G. Kucsko, P. C. Maurer, N. Y. Yao, M. Kubo, H. J. Noh, P. K. Lo, H. Park, and M. D. Lukin. Nanometre-scale thermometry in a living cell. *Nature*, 500(7460):54–58, 08 2013.

[61] J. M. Taylor, P. Cappellaro, L. Childress, L. Jiang, D. Budker, P. R. Hemmer, A. Yacoby, R. Walsworth, and M. D. Lukin. High-sensitivity diamond magnetometer with nanoscale resolution. *Nat. Phys.*, 4(10):810–816, 10 2008.

[62] Gopalakrishnan Balasubramanian, I. Y. Chan, Roman Kolesov, Mohannad Al-Hmoud, Julia Tisler, Chang Shin, Changdong Kim, Aleksander Wojcik, Philip R. Hemmer, Anke Krueger, Tobias Hanke, Alfred Leitenstorfer, Rudolf Bratschitsch, Fedor Jelezko, and Jorg Wrachtrup. Nanoscale imaging magnetometry with diamond spins under ambient conditions. *Nature*, 455(7213):648–651, 10 2008.

[63] F. Dolde, H. Fedder, M. W. Doherty, T. Nobauer, F. Rempp, G. Balasubramanian, T. Wolf, F. Reinhard, L. C. L. Hollenberg, F. Jelezko, and J. Wrachtrup. Electric-field sensing using single diamond spins. *Nat. Phys.*, 7(6):459–463, 06 2011.

[64] M. W. Doherty, F. Dolde, H. Fedder, F. Jelezko, J. Wrachtrup, N. B. Manson, and L. C. L. Hollenberg. Theory of the ground-state spin of the nv${}^{\ensuremath{-}}$ center in diamond. *Phys. Rev. B*, 85(20):205203–, 05 2012.

[65] J. P. Goss, P. R. Briddon, M. J. Rayson, S. J. Sque, and R. Jones. Vacancy-impurity complexes and limitations for implantation doping of diamond. *Phys. Rev. B*, 72(3):035214–, 07 2005.

[66] Tom Feng and Bradley D. Schwartz. Characteristics and origin of the 1.681 ev luminescence center in chemical-vapor-deposited diamond films. *J. Appl. Phys.*, 73(3):1415–1425, 2017/07/03 1993.

[67] Elke Neu, Christian Hepp, Michael Hauschild, Stefan Gsell, Martin Fischer, Hadwig Sternschulte, Doris Steinmüller-Nethl, Matthias Schreck, and Christoph Becher. Low-temperature investigations of single silicon vacancy colour centres in diamond. *New J. Phys*, 15(4):043005, 2013.

[68] Stefano Lagomarsino, Federico Gorelli, Mario Santoro, Nicole Fabbri, Ahmed Hajeb, Silvio Sciortino, Lara Palla, Caroline Czelusniak, Mirko Massi, Francesco Taccetti, Lorenzo Giuntini, Nicla Gelli, Dmitry Yu Fedyanin, Francesco Saverio Cataliotti, Costanza Toninelli, and Mario Agio. Robust luminescence of the silicon-vacancy center in diamond at high temperatures. *AIP Advances*, 5(12):127117, 2017/10/04 2015.

[69] Daniel Foreman-Mackey, David W. Hogg, Dustin Lang, and Jonathan Goodman. emcee: The mcmc hammer. *Publ. Astron. Soc. Pac*, 125(925):306, 2013.

[70] J. Goodman and J. Weare. Ensemble samplers with affine invariance. *Comm. App. Math. Comp. Sci.*, 5(1):65–85, 2010.

[71] V. M. Acosta, E. Bauch, M. P. Ledbetter, C. Santori, K. M. C. Fu, P. E. Barclay, R. G. Beausoleil, H. Linget, J. F. Roch, F. Treussart, S. Chemerisov,

W. Gawlik, and D. Budker. Diamonds with a high density of nitrogen-vacancy centers for magnetometry applications. *Phys. Rev. B*, 80(11):115202–, 09 2009.

[72] U. F. S. D'Haenens-Johansson, A. M. Edmonds, B. L. Green, M. E. Newton, G. Davies, P. M. Martineau, R. U. A. Khan, and D. J. Twitchen. Optical properties of the neutral silicon split-vacancy center in diamond. *Phys. Rev. B*, 84(24):245208–, 12 2011.

[73] Leonid Khriachtchev, Lauri Heikkilä, and Tom Kuusela. Red photoluminescence of gold island films. *Appl. Phys. Lett.*, 78(14):1994–1996, 2017/06/26 2001.

[74] António Tadeu and Nuno Simões. Three-dimensional fundamental solutions for transient heat transfer by conduction in an unbounded medium, half-space, slab and layered media. *Eng. Anal. Bound. Elem.*, 30(5):338–349, 2006.

[75] Yanan Yue and Xinwei Wang. Nanoscale thermal probing. *Nano Rev.*, 3(1):11586, 01 2012.

[76] Maya Shamir, Yinon Bar-On, Rob Phillips, and Ron Milo. Snapshot: Timescales in cell biology. *Cell*, 164(6):1302–1302.e1, 2017/11/02 2016.

[77] Andrew M. Smith, Michael C. Mancini, and Shuming Nie. Bioimaging: Second window for in vivo imaging. *Nat. Nano.*, 4(11):710–711, 11 2009.

[78] M. Kern, J. Jeske, D. W. M. Lau, A. D. Greentree, F. Jelezko, and J. Twamley. Optical cryocooling of diamond. *Phys. Rev. B*, 95(23):235306–, 06 2017.

[79] H.-J. Briegel, W. Dür, J. I. Cirac, and P. Zoller. Quantum repeaters: The role of imperfect local operations in quantum communication. *Phys. Rev. Lett.*, 81:5932–5935, Dec 1998.

[80] L. Childress, J. M. Taylor, A. S. Sørensen, and M. D. Lukin. Fault-tolerant quantum communication based on solid-state photon emitters. *Phys. Rev. Lett.*, 96:070504, Feb 2006.

[81] Stephan Ritter, Christian Nölleke, Carolin Hahn, Andreas Reiserer, Andreas Neuzner, Manuel Uphoff, Martin Mücke, Eden Figueroa, Joerg Bochmann, and Gerhard Rempe. An elementary quantum network of single atoms in optical cavities. *Nature*, 484(7393):195–200, 2012.

[82] D Hucul, IV Inlek, G Vittorini, C Crocker, S Debnath, SM Clark, and Cl Monroe. Modular entanglement of atomic qubits using photons and phonons. *Nat. Phys.*, 11(1):37–42, 2015.

[83] WB Gao, A Imamoglu, H Bernien, and R Hanson. Coherent manipulation, measurement and entanglement of individual solid-state spins using optical fields. *Nat. Photon.*, 9(6):363–373, 2015.

[84] David Press, Kristiaan De Greve, Peter L. McMahon, Thaddeus D. Ladd, Benedikt Friess, Christian Schneider, Martin Kamp, Sven Höfling, Alfred Forchel, and Yoshihisa Yamamoto. Ultrafast optical spin echo in a single quantum dot. *Nature Photonics*, 4(6):367–370, 2010.

[85] G. Balasubramanian, P. Neumann, D. Twitchen, M. Markham, R. Kolesov, N. Mizuochi, J. Isoya, J. Achard, J. Beck, J. Tissler, V. Jacques, P. R. Hemmer, F. Jelezko, and J. Wrachtrup. Ultralong spin coherence time in isotopically engineered diamond. *Nature Materials*, 8(5):383–387, 2009.

[86] A. Faraon, C. Santori, Z. Huang, Victor M. Acosta, and Raymond G. Beausoleil. Coupling of nitrogen-vacancy centers to photonic crystal cavities in monocrystalline diamond. *Phys. Rev. Lett.*, 109:033604, Jul 2012.

[87] Bas Hensen, H Bernien, AE Dréau, A Reiserer, N Kalb, MS Blok, J Ruitenberg, RFL Vermeulen, RN Schouten, C Abellán, et al. Loophole-free bell inequality violation using electron spins separated by 1.3 kilometres. *Nature*, 526(7575):682–686, 2015.

[88] Aymeric Delteil, Zhe Sun, Wei-bo Gao, Emre Togan, Stefan Faelt, and Ataç Imamoğlu. Generation of heralded entanglement between distant hole spins. *Nat. Phys.*, 12:218–223, 2015.

[89] A. Sipahigil, K. D. Jahnke, L. J. Rogers, T. Teraji, J. Isoya, A. S. Zibrov, F. Jelezko, and M. D. Lukin. Indistinguishable photons from separated silicon-vacancy centers in diamond. *Phys. Rev. Lett.*, 113:113602, Sep 2014.

[90] A. M. Edmonds, M. E. Newton, P. M. Martineau, D. J. Twitchen, and S. D. Williams. Electron paramagnetic resonance studies of silicon-related defects in diamond. *Phys. Rev. B*, 77:245205, Jun 2008.

[91] B. L. Green, S. Mottishaw, B. G. Breeze, A. M. Edmonds, U. F. S. D'Haenens-Johansson, M. W. Doherty, S. D. Williams, D. J. Twitchen, and M. E. Newton. Neutral silicon-vacancy center in diamond: Spin polarization and lifetimes. *Phys. Rev. Lett.*, 119:096402, Aug 2017.

[92] Brendon C. Rose, Ding Huang, Zi-Huai Zhang, Paul Stevenson, Alexei M. Tyryshkin, Sorawis Sangtawesin, Srikanth Srinivasan, Lorne Loudin, Matthew L. Markham, Andrew M. Edmonds, Daniel J. Twitchen, Stephen A. Lyon, and Nathalie P. de Leon. Observation of an environmentally insensitive solid-state spin defect in diamond. *Science*, 361(6397):60–63, 2018.

[93] Lucio Robledo, Lilian Childress, Hannes Bernien, Bas Hensen, Paul F. A. Alkemade, and Ronald Hanson. High-fidelity projective read-out of a solid-state spin quantum register. *Nature*, 477(7366):574–578, 2011.

[94] Aymeric Delteil, Wei-bo Gao, Parisa Fallahi, Javier Miguel-Sanchez, and Atac Imamoğlu. Observation of quantum jumps of a single quantum dot spin using submicrosecond single-shot optical readout. *Phys. Rev. Lett.*, 112:116802, Mar 2014.

[95] L. Childress, M. V. Gurudev Dutt, J. M. Taylor, A. S. Zibrov, F. Jelezko, J. Wrachtrup, P. R. Hemmer, and M. D. Lukin. Coherent dynamics of coupled electron and nuclear spin qubits in diamond. *Science*, 314(5797):281–285, 2006.

[96] C. A. Ryan, J. S. Hodges, and D. G. Cory. Robust decoupling techniques to extend quantum coherence in diamond. *Phys. Rev. Lett.*, 105:200402, Nov 2010.

[97] G. de Lange, Z. H. Wang, D. Ristè, V. V. Dobrovitski, and R. Hanson. Universal dynamical decoupling of a single solid-state spin from a spin bath. *Science*, 330(6000):60–63, 2010.

[98] S. Meiboom and D. Gill. Modified spin-echo method for measuring nuclear relaxation times. *Review of Scientific Instruments*, 29(8):688–691, 1958.

[99] N. Bar-Gill, L. M. Pham, A. Jarmola, D. Budker, and R. L. Walsworth. Solid-state electronic spin coherence time approaching one second. *Nature Communications*, 4(1):1743, 2013.

[100] J. Medford, Ł. Cywiński, C. Barthel, C. M. Marcus, M. P. Hanson, and A. C. Gossard. Scaling of dynamical decoupling for spin qubits. *Phys. Rev. Lett.*, 108:086802, Feb 2012.

[101] A. J. Sigillito, H. Malissa, A. M. Tyryshkin, H. Riemann, N. V. Abrosimov, P. Becker, H.-J. Pohl, M. L. W. Thewalt, K. M. Itoh, J. J. L. Morton, A. A. Houck, D. I. Schuster, and S. A. Lyon. Fast, low-power manipulation of spin ensembles in superconducting microresonators. *Applied Physics Letters*, 104(22):222407, 2014.

[102] Peter Christian Maurer, Georg Kucsko, Christian Latta, Liang Jiang, Norman Ying Yao, Steven D Bennett, Fernando Pastawski, David Hunger, Nicholas Chisholm, Matthew Markham, et al. Room-temperature quantum bit memory exceeding one second. *Science*, 336(6086):1283–1286, 2012.

[103] Young-Ik Sohn, Srujan Meesala, Benjamin Pingault, Haig A Atikian, Jeffrey Holzgrafe, Mustafa Gundogan, Camille Stavrakas, Megan J Stanley, Alp Sipahigil, Joonhee Choi, et al. Engineering a diamond spin-qubit with a nano-electro-mechanical system. *arXiv preprint arXiv:1706.03881*, 2017.

[104] Michael J. Burek, Justin D. Cohen, Seán M. Meenehan, Nayera El-Sawah, Cleaven Chia, Thibaud Ruelle, Srujan Meesala, Jake Rochman, Haig A. Atikian, Matthew Markham, Daniel J. Twitchen, Mikhail D. Lukin, Oskar Painter, and Marko Lončar. Diamond optomechanical crystals. *Optica*, 3(12):1404–1411, Dec 2016.

[105] J Majer, JM Chow, JM Gambetta, Jens Koch, BR Johnson, JA Schreier, L Frunzio, DI Schuster, AA Houck, Andreas Wallraff, et al. Coupling superconducting qubits via a cavity bus. *Nature*, 449(7161):443–447, 2007.

[106] S. D. Bennett, N. Y. Yao, J. Otterbach, P. Zoller, P. Rabl, and M. D. Lukin. Phonon-induced spin-spin interactions in diamond nanostructures: application to spin squeezing. *Phys. Rev. Lett.*, 110(15):156402, 2013.

[107] K. Stannigel, P. Rabl, A. S. Sørensen, M. D. Lukin, and P. Zoller. Optomechanical transducers for quantum-information processing. *Phys. Rev. A*, 84:042341, Oct 2011.

[108] Martin V. Gustafsson, Thomas Aref, Anton Frisk Kockum, Maria K. Ekström, Göran Johansson, and Per Delsing. Propagating phonons coupled to an artificial atom. *Science*, 346(6206):207–211, 2014.

[109] L. Childress, J. M. Taylor, A. S. Sørensen, and M. D. Lukin. Fault-tolerant quantum repeaters with minimal physical resources and implementations based on single-photon emitters. *Phys. Rev. A*, 72:052330, Nov 2005.

[110] A. Stute, B. Casabone, B. Brandstätter, K. Friebe, T. E. Northup, and R. Blatt. Quantum-state transfer from an ion to a photon. *Nature Photonics*, 7:219 EP –, 02 2013.

[111] Andreas Reiserer and Gerhard Rempe. Cavity-based quantum networks with single atoms and optical photons. *Rev. Mod. Phys.*, 87:1379–1418, Dec 2015.

[112] Norbert Kalb, Andreas Reiserer, Stephan Ritter, and Gerhard Rempe. Heralded storage of a photonic quantum bit in a single atom. *Phys. Rev. Lett.*, 114:220501, Jun 2015.

[113] Stephan Welte, Bastian Hacker, Severin Daiss, Stephan Ritter, and Gerhard Rempe. Photon-mediated quantum gate between two neutral atoms in an optical cavity. *Phys. Rev. X*, 8(1):011018, 2018.

[114] Hyochul Kim, Deepak Sridharan, Thomas C Shen, Glenn S Solomon, and Edo Waks. Strong coupling between two quantum dots and a photonic crystal cavity using magnetic field tuning. *Opt. Express*, 19(3):2589–2598, 2011.

[115] A. Javadi, I. Sollner, M. Arcari, S. Lindskov Hansen, L. Midolo, S. Mahmoodian, G. Kirsanske, T. Pregnolato, E. H. Lee, J. D. Song, S. Stobbe, and P. Lodahl. Single-photon non-linear optics with a quantum dot in a waveguide. *Nat. Commun.*, 6:8655, Oct 2015.

[116] Sean Molesky, Zin Lin, Alexander Y. Piggott, Weiliang Jin, Jelena Vuckovic, and Alejandro W. Rodriguez. Inverse design in nanophotonics. *Nature Photonics*, 12(11):659–670, 2018.

[117] M. H. Abobeih, J. Cramer, M. A. Bakker, N. Kalb, M. Markham, D. J. Twitchen, and T. H. Taminiau. One-second coherence for a single electron spin

coupled to a multi-qubit nuclear-spin environment. *Nature Communications*, 9(1):2552, 2018.

[118] G. Waldherr, Y. Wang, S. Zaiser, M. Jamali, T. Schulte-Herbrüggen, H. Abe, T. Ohshima, J. Isoya, J. F. Du, P. Neumann, and J. Wrachtrup. Quantum error correction in a solid-state hybrid spin register. *Nature*, 506:204 EP –, Feb 2014.

[119] W. Pfaff, B. J. Hensen, H. Bernien, S. B. van Dam, M. S. Blok, T. H. Taminiau, M. J. Tiggelman, R. N. Schouten, M. Markham, D. J. Twitchen, and R. Hanson. Unconditional quantum teleportation between distant solid-state quantum bits. *Science*, 345(6196):532–535, 2014.

[120] Jonas N. Becker, Benjamin Pingault, David Groß, Mustafa Gündoğan, Nadezhda Kukharchyk, Matthew Markham, Andrew Edmonds, Mete Atatüre, Pavel Bushev, and Christoph Becher. All-optical control of the silicon-vacancy spin in diamond at millikelvin temperatures. *Phys. Rev. Lett.*, 120:053603, Jan 2018.

[121] Srujan Meesala, Young-Ik Sohn, Benjamin Pingault, Linbo Shao, Haig A. Atikian, Jeffrey Holzgrafe, Mustafa Gündoğan, Camille Stavrakas, Alp Sipahigil, Cleaven Chia, Ruffin Evans, Michael J. Burek, Mian Zhang, Lue Wu, Jose L. Pacheco, John Abraham, Edward Bielejec, Mikhail D. Lukin, Mete Atatüre, and Marko Lončar. Strain engineering of the silicon-vacancy center in diamond. *Phys. Rev. B*, 97:205444, May 2018.

[122] Mathias H Metsch, Katharina Senkalla, Benedikt Tratzmiller, Jochen Scheuer, Michael Kern, Jocelyn Achard, Alexandre Tallaire, Martin B Plenio, Petr Siyushev, and Fedor Jelezko. Initialization and readout of nuclear spins via negatively charged silicon-vacancy center in diamond. *arXiv preprint arXiv:1902.02965*, 2019.

[123] Tina Müller, Christian Hepp, Benjamin Pingault, Elke Neu, Stefan Gsell, Matthias Schreck, Hadwig Sternschulte, Doris Steinmüller-Nethl, Christoph Becher, and Mete Atatüre. Optical signatures of silicon-vacancy spins in diamond. *Nat. Comm.*, 5:3328, 2014.

[124] Ernst G. Bauer, Brian W. Dodson, Daniel J. Ehrlich, Leonard C. Feldman, C. Peter Flynn, Michael W. Geis, James P. Harbison, Richard J. Matyi, Paul S.

Peercy, Pierre M. Petroff, and et al. Fundamental issues in heteroepitaxy—a department of energy, council on materials science panel report. *Journal of Materials Research*, 5(4):852–894, 1990.

[125] Michael J Burek, Nathalie P de Leon, Brendan J Shields, Birgit JM Hausmann, Yiwen Chu, Qimin Quan, Alexander S Zibrov, Hongkun Park, Mikhail D Lukin, and Marko Lončar. Free-standing mechanical and photonic nanostructures in single-crystal diamond. *Nano Lett.*, 12(12):6084–6089, 2012.

[126] Behzad Khanaliloo, Matthew Mitchell, Aaron C. Hryciw, and Paul E. Barclay. High-q/v monolithic diamond microdisks fabricated with quasi-isotropic etching. *Nano Letters*, 15(8):5131–5136, Aug 2015.

[127] Sara Mouradian, Noel H. Wan, Tim Schröder, and Dirk Englund. Rectangular photonic crystal nanobeam cavities in bulk diamond. *Applied Physics Letters*, 111(2):021103, 2017.

[128] Haig A. Atikian, Pawel Latawiec, Michael J. Burek, Young-Ik Sohn, Srujan Meesala, Normand Gravel, Ammar B. Kouki, and Marko Lončar. Freestanding nanostructures via reactive ion beam angled etching. *APL Photonics*, 2(5):051301, 2017.

[129] Michael J Burek, Charles Meuwly, Ruffin E Evans, Mihir K Bhaskar, Alp Sipahigil, Srujan Meesala, Bartholomeus Machielse, Denis D Sukachev, Christian T Nguyen, Jose L Pacheco, et al. Fiber-coupled diamond quantum nanophotonic interface. *Phys. Rev. Appl.*, 8(2):024026, 2017.

[130] Michael J Burek, Yiwen Chu, Madelaine SZ Liddy, Parth Patel, Jake Rochman, Srujan Meesala, Wooyoung Hong, Qimin Quan, Mikhail D Lukin, and Marko Lončar. High quality-factor optical nanocavities in bulk single-crystal diamond. *Nat. Commun.*, 5:5718, 2014.

[131] C. D. Clark, H. Kanda, I. Kiflawi, and G. Sittas. Silicon defects in diamond. *Phys. Rev. B*, 51:16681–16688, Jun 1995.

[132] Constantin Dory, Dries Vercruysse, Ki Youl Yang, Neil V. Sapra, Alison E. Rugar, Shuo Sun, Daniil M. Lukin, Alexander Y. Piggott, Jingyuan L. Zhang, Ma-

rina Radulaski, Konstantinos G. Lagoudakis, Logan Su, and Jelena Vuckovic. Optimized diamond quantum photonics. *arXiv preprint arXiv:1812.02287*, 2019.

[133] David M. Toyli, Christoph D. Weis, Gregory D. Fuchs, Thomas Schenkel, and David D. Awschalom. Chip-scale nanofabrication of single spins and spin arrays in diamond. *Nano Letters*, 10(8):3168–3172, Aug 2010.

[134] T. Staudacher, F. Ziem, L. Häussler, R. Stöhr, S. Steinert, F. Reinhard, J. Scharpf, A. Denisenko, and J. Wrachtrup. Enhancing the spin properties of shallow implanted nitrogen vacancy centers in diamond by epitaxial overgrowth. *Applied Physics Letters*, 101(21):212401, 2012.

[135] M. W. Doherty, N. B. Manson, P. Delaney, and L. C. L. Hollenberg. The negatively charged nitrogen-vacancy centre in diamond: the electronic solution. *New J. Phys.*, 13(2):025019, 2011.

[136] J. M. Moison, F. Houzay, F. Barthe, L. Leprince, E. André, and O. Vatel. Self-organized growth of regular nanometer-scale inas dots on gaas. *Applied Physics Letters*, 64(2):196–198, 1994.

[137] Daniel Riedel, Immo Söllner, Brendan J. Shields, Sebastian Starosielec, Patrick Appel, Elke Neu, Patrick Maletinsky, and Richard J. Warburton. Deterministic enhancement of coherent photon generation from a nitrogen-vacancy center in ultrapure diamond. *Phys. Rev. X*, 7:031040, Sep 2017.

[138] T. Gullion, D.B. Baker, and M.S. Conradi. New, compensated carr-purcell sequences. *Journal of Magnetic Resonance (1969)*, 89(3):479–484, 1990.

[139] A. D. Milov, A. B. Ponomarev, and Yu D. Tsvetkov. Electron-electron double resonance in electron spin echo: Model biradical systems and the sensitized photolysis of decalin. *Chemical Physics Letters*, 110(1):67–72, 1984.

[140] B. A. Myers, A. Das, M. C. Dartiailh, K. Ohno, D. D. Awschalom, and A. C. Bleszynski Jayich. Probing surface noise with depth-calibrated spins in diamond. *Phys. Rev. Lett.*, 113:027602, Jul 2014.

[141] R. Kalish and S. Prawer. Graphitization of diamond by ion impact: Fundamentals and applications. *Nuclear Instruments and Methods in Physics Research*

Section B: Beam Interactions with Materials and Atoms, 106(1):492 – 499, 1995. Ion Beam Modification of Materials.

[142] L-M Duan and H J Kimble. Scalable photonic quantum computation through cavity-assisted interactions. *Phys. Rev. Lett.*, 92(12):127902, 2004.

[143] TG Tiecke, Jeffrey Douglas Thompson, Nathalie Pulmones de Leon, LR Liu, V Vuletić, and Mikhail D Lukin. Nanophotonic quantum phase switch with a single atom. *Nature*, 508(7495):241–244, 2014.

[144] J. Casanova, Z.-Y. Wang, J. F. Haase, and M. B. Plenio. Robust dynamical decoupling sequences for individual-nuclear-spin addressing. *Phys. Rev. A*, 92:042304, Oct 2015.

[145] Ilai Schwartz, Jochen Scheuer, Benedikt Tratzmiller, Samuel Müller, Qiong Chen, Ish Dhand, Zhen-Yu Wang, Christoph Müller, Boris Naydenov, Fedor Jelezko, and Martin B. Plenio. Robust optical polarization of nuclear spin baths using hamiltonian engineering of nitrogen-vacancy center quantum dynamics. *Science Advances*, 4(8), 2018.

[146] T. H. Taminiau, J. Cramer, T. van der Sar, V. V. Dobrovitski, and R. Hanson. Universal control and error correction in multi-qubit spin registers in diamond. *Nature Nanotechnology*, 9:171 EP –, 02 2014.

[147] Xing Rong, Jianpei Geng, Fazhan Shi, Ying Liu, Kebiao Xu, Wenchao Ma, Fei Kong, Zhen Jiang, Yang Wu, and Jiangfeng Du. Experimental fault-tolerant universal quantum gates with solid-state spins under ambient conditions. *Nature Communications*, 6:8748 EP –, Nov 2015. Article.

[148] Bartholomeus Machielse, Stefan Bogdanovic, Srujan Meesala, Scarlett Gauthier, Michael J Burek, Graham Joe, Michelle Chalupnik, Young-Ik Sohn, Jeffrey Holzgrafe, Ruffin E Evans, et al. Electromechanical control of quantum emitters in nanophotonic devices. *arXiv preprint arXiv:1901.09103*, 2019.

[149] A. Stute, B. Casabone, P. Schindler, T. Monz, P. O. Schmidt, B. Brandstätter, T. E. Northup, and R. Blatt. Tunable ion-photon entanglement in an optical cavity. *Nature*, 485:482 EP –, May 2012.

[150] Maximilian Ruf, Mark IJspeert, Suzanne van Dam, Nick de Jong, Hans van den Berg, Guus Evers, and Ronald Hanson. Optically coherent nitrogen-vacancy centers in m-thin etched diamond membranes. *arXiv preprint arXiv:1904.00883*, 2019.

[151] G. de Lange, Z. H. Wang, D. Ristè, V. V. Dobrovitski, and R. Hanson. Universal dynamical decoupling of a single solid-state spin from a spin bath. *Science*, 330(6000):60–63, 2010.

[152] MV Gurudev Dutt, L Childress, L Jiang, E Togan, J Maze, F Jelezko, AS Zibrov, PR Hemmer, and MD Lukin. Quantum register based on individual electronic and nuclear spin qubits in diamond. *Science*, 316(5829):1312–1316, 2007.

[153] Shimon Kolkowitz, Quirin P. Unterreithmeier, Steven D. Bennett, and Mikhail D. Lukin. Sensing distant nuclear spins with a single electron spin. *Phys. Rev. Lett.*, 109:137601, Sep 2012.

[154] L. G. Rowan, E. L. Hahn, and W. B. Mims. Electron-spin-echo envelope modulation. *Phys. Rev.*, 137:A61–A71, Jan 1965.

[155] H. Bernien, B. Hensen, W. Pfaff, G. Koolstra, M. S. Blok, L. Robledo, T. H. Taminiau, M. Markham, D. J. Twitchen, L. Childress, and R. Hanson. Heralded entanglement between solid-state qubits separated by three metres. *Nature*, 497(7447):86–90, May 2013.

[156] Aymeric Delteil, Zhe Sun, Stefan Fält, and Atac Imamoglu. Realization of a cascaded quantum system: Heralded absorption of a single photon qubit by a single-electron charged quantum dot. *Phys. Rev. Lett.*, 118:177401, Apr 2017.

[157] Mihir K. Bhaskar, Ralf Riedinger, Bartholomeus Machielse, David S. Levonian, Christian T. Nguyen, Erik N. Knall, Hongkun Park, Dirk Englund, Marko Lončar, Denis D. Sukachev, and Mikhail D. Lukin. Experimental demonstration of memory-enhanced quantum communication. *arXiv preprint arXiv:1909.01323*, 2019.

[158] B. Machielse, S. Bogdanovic, S. Meesala, S. Gauthier, M. J. Burek, G. Joe, M. Chalupnik, Y. I. Sohn, J. Holzgrafe, R. E. Evans, C. Chia, H. Atikian, M. K. Bhaskar, D. D. Sukachev, L. Shao, S. Maity, M. D. Lukin, and M. Lončar.

Quantum interference of electromechanically stabilized emitters in nanophotonic devices. *Phys. Rev. X*, 9:031022, Aug 2019.

[159] Petr Siyushev, Mathias H. Metsch, Aroosa Ijaz, Jan M. Binder, Mihir K. Bhaskar, Denis D. Sukachev, Alp Sipahigil, Ruffin E. Evans, Christian T. Nguyen, Mikhail D. Lukin, Philip R. Hemmer, Yuri N. Palyanov, Igor N. Kupriyanov, Yuri M. Borzdov, Lachlan J. Rogers, and Fedor Jelezko. Optical and microwave control of germanium-vacancy center spins in diamond. *Phys. Rev. B*, 96:081201(R), Aug 2017.

[160] Matthew E Trusheim, Benjamin Pingault, Noel H Wan, Lorenzo De Santis, Kevin C Chen, Michael Walsh, Joshua J Rose, Jonas N Becker, Eric Bersin, Girish Malladi, et al. Transform-limited photons from a tin-vacancy spin in diamond. *arXiv preprint arXiv:1811.07777*, 2018.

[161] Donovan Buterakos, Edwin Barnes, and Sophia E Economou. Deterministic generation of all-photonic quantum repeaters from solid-state emitters. *Physical Review X*, 7(4):041023, 2017.

[162] Alexander Zaitsev. *Optical Properties of Diamond.* Springer, 01 2001.

[163] M. K. Bhaskar, D. D. Sukachev, A. Sipahigil, R. E. Evans, M. J. Burek, C. T. Nguyen, L. J. Rogers, P. Siyushev, M. H. Metsch, H. Park, F. Jelezko, M. Lončar, and M. D. Lukin. Quantum nonlinear optics with a germanium-vacancy color center in a nanoscale diamond waveguide. *Phys. Rev. Lett.*, 118:223603, May 2017.

[164] Masfer Alkahtani, Ivan Cojocaru, Xiaohan Liu, Tobias Herzig, Jan Meijer, Johannes Küpper, Tobias Lühmann, Alexey V. Akimov, and Philip R. Hemmer. Tin-vacancy in diamonds for luminescent thermometry. *Applied Physics Letters*, 112(24):241902, 2018.

[165] Sean Blakley, Xiaohan Liu, Ilya Fedotov, Ivan Cojocaru, Christapher Vincent, Masfer Alkahtani, Joe Becker, Michael Kieschnick, Tobias Lühman, Jan Meijer, Philip Hemmer, Alexey Akimov, Marlan Scully, and Aleksei Zheltikov. Fiber-optic quantum thermometry with germanium-vacancy centers in diamond. *ACS Photonics*, 6(7):1690–1693, Jul 2019.

[166] D. A. Broadway, B. C. Johnson, M. S. J. Barson, S. E. Lillie, N. Dontschuk, D. J. McCloskey, A. Tsai, T. Teraji, D. A. Simpson, A. Stacey, J. C. McCallum, J. E. Bradby, M. W. Doherty, L. C. L. Hollenberg, and J.-P. Tetienne. Microscopic imaging of the stress tensor in diamond using in situ quantum sensors. *Nano Letters*, 19(7):4543–4550, Jul 2019.

[167] M.-A. Lemonde, S. Meesala, A. Sipahigil, M. J. A. Schuetz, M. D. Lukin, M. Loncar, and P. Rabl. Phonon networks with silicon-vacancy centers in diamond waveguides. *Phys. Rev. Lett.*, 120:213603, May 2018.

[168] Smarak Maity, Linbo Shao, Stefan Bogdanovic, Srujan Meesala, Young-Ik Sohn, Neil Sinclair, Benjamin Pingault, Michelle Chalupnik, Cleaven Chia, Lu Zheng, Keji Lai, and Marko Loncar. Coherent acoustic control of a single silicon vacancy spin in diamond. *Nature Communications*, 11(1):193, 2020.

[169] Hoi-Kwong Lo, Marcos Curty, and Bing Qi. Measurement-device-independent quantum key distribution. *Phys. Rev. Lett.*, 108:130503, Mar 2012.

[170] Christiana Panayi, Mohsen Razavi, Xiongfeng Ma, and Norbert Lütkenhaus. Memory-assisted measurement-device-independent quantum key distribution. *New Journal of Physics*, 16(4):043005, apr 2014.

[171] W. K. Wootters and W. H. Zurek. A single quantum cannot be cloned. *Nature*, 299(5886):802–803, 1982.

[172] D. Dieks. Communication by epr devices. *Physics Letters A*, 92(6):271 – 272, 1982.

[173] Stefano Pirandola, Riccardo Laurenza, Carlo Ottaviani, and Leonardo Banchi. Fundamental limits of repeaterless quantum communications. *Nature Communications*, 8(1):15043, 2017.

[174] M. Minder, M. Pittaluga, G. L. Roberts, M. Lucamarini, J. F. Dynes, Z. L. Yuan, and A. J. Shields. Experimental quantum key distribution beyond the repeaterless secret key capacity. *Nature Photonics*, 13(5):334–338, 2019.

[175] Hans J. Briegel and Robert Raussendorf. Persistent entanglement in arrays of interacting particles. *Phys. Rev. Lett.*, 86:910–913, Jan 2001.

[176] J. Borregaard, H. Pichler, T. Sch'oder, M. D. Lukin, P. Lodahl, and A. S. Sørensen. One-way quantum repeater based on near-deterministic photon-emitter interfaces. *arXiv preprint arXiv:1907.05101*, 2019.

[177] Robert Raussendorf and Hans J. Briegel. A one-way quantum computer. *Phys. Rev. Lett.*, 86:5188–5191, May 2001.

[178] E. T. Khabiboulline, J. Borregaard, K. De Greve, and M. D. Lukin. Optical interferometry with quantum networks. *Phys. Rev. Lett.*, 123:070504, Aug 2019.

[179] Anna Tchebotareva, Sophie L. N. Hermans, Peter C. Humphreys, Dirk Voigt, Peter J. Harmsma, Lun K. Cheng, Ad L. Verlaan, Niels Dijkhuizen, Wim de Jong, Anaïs Dréau, and Ronald Hanson. Entanglement between a diamond spin qubit and a photonic time-bin qubit at telecom wavelength. *Phys. Rev. Lett.*, 123:063601, Aug 2019.

[180] Smarak Maity, Linbo Shao, Young-Ik Sohn, Srujan Meesala, Bartholomeus Machielse, Edward Bielejec, Matthew Markham, and Marko Lončar. Spectral alignment of single-photon emitters in diamond using strain gradient. *Phys. Rev. Applied*, 10:024050, Aug 2018.

[181] Igor Aharonovich, Jonathan C. Lee, Andrew P. Magyar, Bob B. Buckley, Christopher G. Yale, David D. Awschalom, and Evelyn L. Hu. Homoepitaxial growth of single crystal diamond membranes for quantum information processing. *Adv. Mat.*, 24(10):OP54–OP59, 2012.

[182] V. A. Davydov, A. V. Rakhmanina, S. G. Lyapin, I. D. Ilichev, K. N. Boldyrev, A. A. Shiryaev, and V. N. Agafonov. Production of nano- and microdiamonds with si-v and n-v luminescent centers at high pressures in systems based on mixtures of hydrocarbon and fluorocarbon compounds. *JETP Lett.*, 99(10):585–589, 2014.

[183] Ruffin E. Evans. Siv tempfit [python code], https://github.com/ruffinevans/sivtempfit, 2016.

[184] N. Bar-Gill, L. M. Pham, C. Belthangady, D. Le Sage, P. Cappellaro, J. R. Maze, M. D. Lukin, A. Yacoby, and R. Walsworth. Suppression of spin-bath

dynamics for improved coherence of multi-spin-qubit systems. *Nature Communications*, 3(1):858, 2012.

[185] Michael J. Biercuk and Hendrik Bluhm. Phenomenological study of decoherence in solid-state spin qubits due to nuclear spin diffusion. *Phys. Rev. B*, 83:235316, Jun 2011.

[186] C. P. Slichter. *Principles of Magnetic Resonance*. Number 1 in Solid State Sciences. Springer-Verlag Berlin Heidelberg, 1990.

[187] Andreas V. Kuhlmann, Jonathan H. Prechtel, Julien Houel, Arne Ludwig, Dirk Reuter, Andreas D. Wieck, and Richard J. Warburton. Transform-limited single photons from a single quantum dot. *Nature Communications*, 6:8204 EP –, Sep 2015. Article.

[188] C. Neill, A. Megrant, R. Barends, Yu Chen, B. Chiaro, J. Kelly, J. Y. Mutus, P. J. J. O'Malley, D. Sank, J. Wenner, T. C. White, Yi Yin, A. N. Cleland, and John M. Martinis. Fluctuations from edge defects in superconducting resonators. *Applied Physics Letters*, 103(7):072601, 2013.

[189] Young-Ik Sohn, Srujan Meesala, Benjamin Pingault, Haig A. Atikian, Jeffrey Holzgrafe, Mustafa Gündogan, Camille Stavrakas, Megan J. Stanley, Alp Sipahigil, Joonhee Choi, Mian Zhang, Jose L. Pacheco, John Abraham, Edward Bielejec, Mikhail D. Lukin, Mete Atatüre, and Marko Loncar. Controlling the coherence of a diamond spin qubit through its strain environment. *Nature Communications*, 9(1):2012, 2018.

[190] T Yamamoto, T Umeda, K Watanabe, S Onoda, M. L. Markham, D. J. Twitchen, B Naydenov, L. P. McGuinness, T Teraji, S Koizumi, F. Dolde, H. Fedder, J. Honert, J. Wrachtrup, T. Ohshima, F. Jelezko, and J. Isoya. Extending spin coherence times of diamond qubits by high-temperature annealing. *Phys. Rev. B*, 88(7):075206, 2013.

[191] C. W. Chou, H. de Riedmatten, D. Felinto, S. V. Polyakov, S. J. van Enk, and H. J. Kimble. Measurement-induced entanglement for excitation stored in remote atomic ensembles. *Nature*, 438(7069):828–832, 2005.

[192] William K. Wootters. Entanglement of formation of an arbitrary state of two qubits. *Phys. Rev. Lett.*, 80:2245–2248, Mar 1998.